**Purdue University**
**Purdue e-Pubs**

Open Access Dissertations

Theses and Dissertations

Spring 2015

# An experimental study on the effects of blade row interactions on aerodynamic loss mechanisms in a multistage compressor

Natalie Rochelle Smith
*Purdue University*

Follow this and additional works at: https://docs.lib.purdue.edu/open_access_dissertations

Part of the Aerospace Engineering Commons, and the Mechanical Engineering Commons

## Recommended Citation

Smith, Natalie Rochelle, "An experimental study on the effects of blade row interactions on aerodynamic loss mechanisms in a multistage compressor" (2015). *Open Access Dissertations*. 558.
https://docs.lib.purdue.edu/open_access_dissertations/558

This document has been made available through Purdue e-Pubs, a service of the Purdue University Libraries. Please contact epubs@purdue.edu for additional information.

**PURDUE UNIVERSITY**
**GRADUATE SCHOOL**
**Thesis/Dissertation Acceptance**

This is to certify that the thesis/dissertation prepared

By Natalie Rochelle Smith

Entitled
An Experimental Study on the Effects of Blade Row Interactions on Aerodynamic Loss Mechanisms in a Multistage Compressor

For the degree of Doctor of Philosophy

Is approved by the final examining committee:

Nicole L. Key
Chair

Jun Chen

Alina Alexeenko

John Sullivan

To the best of my knowledge and as understood by the student in the Thesis/Dissertation Agreement, Publication Delay, and Certification Disclaimer (Graduate School Form 32), this thesis/dissertation adheres to the provisions of Purdue University's "Policy of Integrity in Research" and the use of copyright material.

Approved by Major Professor(s): Nicole L. Key

Approved by: Tom Shih 4/28/2015
Head of the Departmental Graduate Program Date

# AN EXPERIMENTAL STUDY ON THE EFFECTS OF BLADE ROW INTERACTIONS ON AERODYNAMIC LOSS MECHANISMS IN A MULTISTAGE COMPRESSOR

A Dissertation
Submitted to the Faculty
of
Purdue University
by
Natalie Rochelle Smith

In Partial Fulfillment of the
Requirements for the Degree
of
Doctor of Philosophy

May 2015
Purdue University
West Lafayette, Indiana

# ACKNOWLEDGEMENTS

Many people supported this body of work over the past few years, and for that I am endlessly grateful. First, I would like to thank my advisor Nicole Key; she pushed, guided, and encouraged when I needed it and I have grown as a researcher because of her. The technical guidance of John Fabian has been invaluable throughout my project. I appreciate the time and feedback from my committee, Professors John Sullivan, Alina, Alexeenko, and Jun Chen. Various funding sources have supported aspects this research including Rolls-Royce, NASA, and Zonta International. Furthermore, I am thankful for the technical guidance provided by Drs. Roy Fulyater, Aaron King, and Mark Celestina. There are many members of the Zucrow staff who facilitate our work at the lab daily, in particular, the technical advice of Rob McGuire. I am tremendously grateful to all my labmates for their friendship and assistance during my time in the Compressor Lab. Throughout troubleshooting issues and countless discussions of data, Dr. John Brossman and Reid Berdanier have helped me become a better researcher and engineer. My support network of friends, both near and far, have been unwavering in their ability to put a smile on my face. And finally, I would like to acknowledge my family; my parents and brother have inspired and encouraged me every step of the way with their examples of both dedication and love.

# TABLE OF CONTENTS

Page

LIST OF TABLES ........ vii

LIST OF FIGURES ........ viii

NOMENCLATURE ........ xv

ABSTRACT ........ xvii

CHAPTER 1. INTRODUCTION ........ 1

- 1.1 Aerodynamics Forcing Functions ........ 2
    - 1.1.1 Potential Fields ........ 2
    - 1.1.2 Wakes ........ 3
    - 1.1.3 Additional Aerodynamic Forcing ........ 6
- 1.2 Blade Row Interactions ........ 6
    - 1.2.1 Rotor-Rotor Interactions ........ 7
    - 1.2.2 Stator-Stator Interactions and Vane Clocking ........ 8
        - 1.2.2.1 Turbine Performance ........ 9
        - 1.2.2.2 Compressor Performance ........ 10
        - 1.2.2.3 Flow Physics ........ 12
- 1.3 Boundary Layer Development ........ 14
    - 1.3.1 Multimodal Transition ........ 15
    - 1.3.2 Boundary Layers in Turbomachinery ........ 18
- 1.4 Flow Separation ........ 19
- 1.5 Research Objectives ........ 24

CHAPTER 2. EXPERIMENTAL METHODS ........ 27

- 2.1 Research Facility Overview ........ 27
- 2.2 Purdue 3-stage Axial Research Compressor ........ 28

Page
2.3 Clocking Configurations and Loading Conditions of Interest .............................. 29
2.4 Steady Measurement Methodology ...................................................................... 33
2.5 High Frequency Response Measurement Methodology ....................................... 35
  2.5.1 Time-Resolved Measurements of Stator Inlet Flow ................................... 36
  2.5.2 Surface Mounted Anemometry .................................................................... 36
    2.5.2.1 Methodology Background .................................................................. 36
    2.5.2.2 Sensor Array Design and Implementation .......................................... 38
    2.5.2.3 Quasi-Wall Shear Stress Analysis ...................................................... 40
2.6 Stator 2 Insert for Special Instrumentation .......................................................... 41
2.7 Flow Visualization ................................................................................................ 42
CHAPTER 3. ASPECTS OF COMPRESSOR CORRECTED CONDITIONS AND PERFORMANCE REPEATABILITY ................................................................ 48
3.1 Humidity Accounting ............................................................................................. 49
  3.1.1 Corrected Rotational Speed .......................................................................... 49
  3.1.2 Corrected Mass Flow Rate ........................................................................... 51
  3.1.3 Effects of Humidity on Corrected Conditions .............................................. 53
3.2 Correcting Performance for Density and Work .................................................... 58
  3.2.1 Density Ratio and Work Coefficient Correction Procedure ......................... 60
  3.2.2 Effects of Correcting for Density and Work Coefficient ............................ 63
3.3 Reynolds Number Considerations ........................................................................ 64
3.4 Effects of Inlet Temperature ................................................................................. 68
CHAPTER 4. FLOW VISUALIZATION ..................................................................... 75
4.1 Overview of Flow Visualization ............................................................................ 75
  4.1.1 Effects of Loading Condition ....................................................................... 77
  4.1.2 Comparison with CFD .................................................................................. 83
4.2 Rotor Tip Clearance Effects on Stator Loss Distribution ..................................... 84
4.3 Endwall Flows ........................................................................................................ 90
  4.3.1 Rotor Endwalls .............................................................................................. 90
  4.3.2 Stator Endwalls ............................................................................................. 96

Page

- 4.4 Influence of Instrumentation and Hardware Features ........ 98
- 4.5 Separation Line Variability ........ 100

CHAPTER 5. STEADY VANE CLOCKING RESULTS ........ 105

- 5.1 Flowfield Upstream of Stator 2 ........ 106
  - 5.1.1 Downstream of Stator 1 ........ 106
  - 5.1.2 Downstream of Rotor 2 ........ 107
- 5.2 Vane Clocking Results Downstream of Stator 2 ........ 113
  - 5.2.1 Stator 2 Wake Profiles ........ 115
  - 5.2.2 Stator 2 Exit Total Pressure Radial Profiles ........ 118
  - 5.2.3 Stator 2 Loss ........ 120
  - 5.2.4 Flow Visualization of Stator 2 Corner Separations ........ 124
  - 5.2.5 Overall Vane Clocking Trends ........ 127

CHAPTER 6. ROTOR TIP LEAKAGE FLOW EFFECTS ON VANE CLOCKING 132

- 6.1 Influence of the Tip Leakage Flow ........ 133
- 6.2 Change in Rotor 2 Leakage Flow with Clocking Configuration ........ 141

CHAPTER 7. BLADE ROW INTERACTION EFFECTS ON STATOR SURFACE FLOWS ........ 151

- 7.1 Stator 2 Surface Pressures ........ 151
  - 7.1.1 One-Dimensional Pressure Distributions ........ 152
  - 7.1.2 Surface Pressure Unsteadiness ........ 155
  - 7.1.3 Frequency Domain Analysis ........ 161
- 7.2 Stator 2 Wall Shear Stress ........ 164
  - 7.2.1 Rotor-Rotor Interaction Effects ........ 164
  - 7.2.2 Mean Rotor 2 Blade Pass ........ 165

CHAPTER 8. SUMMARY AND CONCLUSIONS ........ 171

REFERENCES ........ 177

Page

APPENDICES

Appendix A. Flow Visualization of Vanes with Downstream Instrumentation .... 186

Appendix B. Gallery of Fluid Motion .................................................................... 188

Appendix C. Stator 2 Insert Design with Leading Edge and Knife Seal Pressures 189

VITA ......................................................................................................................... 194

PUBLICATIONS ....................................................................................................... 195

# LIST OF TABLES

Table Page

Table 2.1 Summary of stator flow parameters at peak efficiency loading condition ....... 29
Table 2.2 Rake element distributions and area weightings............................................... 35
Table 4.1 Summary of flow visualization cases presented ............................................... 77
Table 4.2 Summary of percent difference in loss coefficient from nominal loading ....... 82
Table 5.1 Summary of Stator 2 loss coefficient changes in terms of percent difference 122

Appendix Table

Table C.1 Costs and lead times of different vendors and manufacturing methods ........ 190

# LIST OF FIGURES

Figure Page

Figure 1.1 Aerodynamic forcing functions ........ 2

Figure 1.2 The effect of a velocity deficit in one reference frame on the downstream row in another reference frame ........ 4

Figure 1.3 Interactions between rows with different rotor blade counts cause a constructive and destructive beating pattern ........ 8

Figure 1.4 Example of vane clocking where clocking offset (CL) is defined as the difference between the upstream and downstream vane positions ........ 9

Figure 1.5 Space-time (st) diagram of multimodal boundary layer transition ........ 17

Figure 1.6 Schematics of flow separation features; (a) corner separation forming at the intersection of the stator suction surface (SS) and the hub endwall, (b) separation critical points including a saddle point and two node types ........ 22

Figure 2.1 The Purdue three-stage axial research compressor facility ........ 28

Figure 2.2 The measurement stations and blade counts in the research compressor ........ 29

Figure 2.3 100% corrected speedline with loading conditions for vane clocking studies and other work ........ 32

Figure 2.4 Part-speed operating points: Nominal Loading and High Loading ........ 32

Figure 2.5 Hot-film sensor array, (a) drawing (b) photo ........ 40

Figure 2.6 Schematic of flow visualization setup ........ 44

Figure 2.7 Lighting comparison with (a) visible, (b) mixed, and (c) UV ........ 47

Figure 3.1 Summary of steady performance data collection ........ 49

Figure 3.2 Effect of humidity on (a) calculated mechanical speed and (b) actual mass flow rate as lines of constant percent difference ........ 57

Figure Page

Figure 3.3 Approximate effects of major research areas on compressor performance compared to humidity effects (Graf et al., 1998; Bons, 2010; Wellborn and Okiishi, 1999; Hynes and Greitzer, 1987) .................................................. 58

Figure 3.4 TPR discrepancy between a hot day and a cold day and 3% and 4% rotor tip clearance ....................................................................................... 59

Figure 3.5 Effects ambient pressure, temperature and relative humidity changes from reference conditions on the enthalpy, density and ratio of specific heats of air in terms of percent difference. ...................................................................... 60

Figure 3.6 Percent difference change in TPR with density and work coefficient correction on a hot and cold day ..................................................................... 64

Figure 3.7 Reynolds Number Index on a hot and cold day ............................................ 67

Figure 3.8 Machine and blade Reynolds number fluctuations with ambient conditions (a) temperature (b) relative humidity (c) pressure ............................................ 68

Figure 3.9 TPR variations with ambient temperature for three nominal tip clearances (a) 1.5%TC (b) 3%TC and (c) 4%TC .............................................................. 71

Figure 3.10 Total pressure wakes at midspan for 3%TC at near stall loading, hot and cold days ........................................................................................... 72

Figure 3.11 Total pressure wakes at 80%span for 3%TC at near stall loading, hot and cold days ........................................................................................ 72

Figure 3.12 Radial total pressure profiles from traversed data downstream of each row for a cold and hot day for the 3% TC ................................................................ 72

Figure 3.13 TPR trends with measured Rotor 1 tip clearance at a near stall operating condition ....................................................................................... 73

Figure 3.14 Radial profiles for three nominal tip clearances on a hot and cold day at nominal loading ........................................................................... 73

Figure 3.15 Radial profiles for three nominal tip clearances on a hot and cold day at near stall loading.......................................................................................... 74

Figure Page

Figure 4.1 Basic surface flow topology for Stator 1 at the high loading condition (a) image, (b) corner separations, and (c) drawn flow topology with saddle points (S) and nodes (N) labelled ........ 77

Figure 4.2 Surface flow visualization of corner separations for Stator 1 (left), Stator 2 (middle), and Stator 3 (right) at three loading conditions: nominal loading (a-c), peak efficiency (d-f), high loading (g-i), and near stall (j-l)........ 81

Figure 4.3 Stator 1 at near stall conditions viewed from the leading edge looking downstream........ 82

Figure 4.4 Comparison of surface streaklines on Stator 3 suction surface between (a) experiment and (b) CFD (Monk 2014) at the peak efficiency loading condition ........ 84

Figure 4.5 Flow visualization of vane corner separations at nominal loading for three different rotor tip clearances, 1.5% (a-c), 3% (d-f), and 4%TC (g-i) ........ 88

Figure 4.6 Flow visualization of vane corner separations at the high loading condition for three different rotor tip clearances, 1.5% (a-c), 3% (d-f), and 4% TC (g-i) with surface flow features highlighted: the extent of radial flow (RF) streamlines and movement of some spiral nodes (SN)........ 89

Figure 4.7 Flow visualization of casing endwall over Rotor 2 at HL........ 91

Figure 4.8 Flow visualization of casing endwall over each rotor at NL and HL for the baseline rotor tip clearance (1.5%TC) ........ 94

Figure 4.9 Flow visualization of casing endwall over each rotor at NL and HL for 3.0%TC........ 95

Figure 4.10 Flow visualization of casing endwall over each rotor at NL and HL for 4.0%TC........ 95

Figure 4.11 Secondary flows on stator passage endwalls highlighting (a) overturning, (b) entrainment in to corner separation (c) large tip corner separation ........ 97

Figure 4.12 Flow visualization of other features: (a) rake ports, (b) leakage paths, (c) vanes with tip gap for instrumentation ........ 100

Figure Page

Figure 4.13 Process to identify separation line using: (a) original image, (b) RGB color separation, (c) binary image, and (d) recirculation region boundary .......... 102

Figure 4.14 Comparison of RGB color breakdown for the blue paint........................... 102

Figure 4.15 Separation lines of 29 Stator 1 vanes at the high loading condition with (a) outliers highlighted and (b) vanes of interest highlighted ........................... 104

Figure 4.16 Separation line variability around the compressor where (a) 0-90°, (b) 90-180°, (c) 180-270°, (d) 270-360° clockwise from the top splitline ............. 104

Figure 5.1 Summary of steady performance data collection .......................................... 106

Figure 5.2 Stator 1 wakes at L8 for six clocking traverses at 12%, 50%, and 88% span 110

Figure 5.3 Stator 1 exit total pressure contours at the nine loading conditions .............. 110

Figure 5.4 Rotor 2 exit total pressure contours at nine loading conditions .................... 111

Figure 5.5 Rotor 2 exit total pressure for CL1 at 20%span for all nine loading conditions ................................................................................................................ 112

Figure 5.6 Rotor 2 exit total pressure for CL1 and CL4 at 20%span for L5 and L8 ...... 112

Figure 5.7 Total pressure contours at Stator 2 exit for all six CL at L5 ......................... 115

Figure 5.8 Tip, midspan, and hub wake profiles at (a) L1 and (b) L7 ........................... 117

Figure 5.9 Total pressure downstream of Stator 2 at 12%span for loadings: (a) L5 (b) L7 (c) L8 ........................................................................................................ 118

Figure 5.10 Radial profiles at Stator 2 exit for all six clocking configurations at all nine loading conditions ........................................................................................ 120

Figure 5.11 Changes in Stator 2 loss with vane clocking at all nine loading conditions 123

Figure 5.12 1D Stator 2 loss for all nine loading conditions ......................................... 124

Figure 5.13 Vane clocking effects on Stator 2 boundary layer separation for the maximum and minimum loss clocking configurations at (a-b) L7 high loading and (c-d) L9 near stall conditions shown with radial total pressure profiles downstream S2 .............................................................................. 127

Figure 5.14 Difference in overall Stator 2 loss between clocking configurations along 100%Nc ......................................................................................................... 130

Figure 5.15 Inlet total temperature for each clocking configuration of present study.... 130

Figure Page

Figure 5.16 Average inlet total temperature for various vane clocking studies in the Purdue three-stage compressor as a function of mass flow rate .................. 131
Figure 6.1 Pressure coefficient RMS contours (left) and Fourier transform of RMS at 80%span (right) for 40% (top) and 90%vp (bottom) at the high loading condition .......................................................................................... 138
Figure 6.2 Average rotor exit flow field, in terms of coefficient of pressure RMS, at each circumferential location across the vane passage (clockwise) at high loading ................................................................................................................. 139
Figure 6.3 Contours of coefficient of pressure RMS (bottom) at high loading for the average passage (left), 40%vp (middle), and 90%vp (right) ....................... 139
Figure 6.4 Schematic of interaction between Stator 1 wake and Rotor 2 tip leakage vortex (a) R2 passing the middle of the S1 passage (b) R2 passing through the S1 wake ..................................................................................................... 140
Figure 6.5 Flow visualization on the casing endwall over Rotor 2 ................................ 140
Figure 6.6 Contours of coefficient of pressure RMS at L1 for CL2 and CL5 ............... 147
Figure 6.7 Contours of coefficient of pressure RMS at L3 for CL3 and CL6 ............... 147
Figure 6.8 Contours of pressure coefficient RMS at L6 for CL2, CL3.5, CL5 and CL6.5 ................................................................................................................. 148
Figure 6.9 Contours of pressure coefficient RMS at L7 for CL2, CL3.5, CL5 and CL6.5 ................................................................................................................. 148
Figure 6.10 Contours of pressure coefficient RMS at L8 for CL2, CL3.5, CL5 and CL6.5 ................................................................................................................. 148
Figure 6.11 Contours of coefficient of pressure RMS at L8 for 12 clocking configurations highlighting the Stator 1 wake location ...................................................... 149
Figure 6.12 Radial total pressure profiles at Rotor 2 exit for six clocking configurations at L1 ........................................................................................................ 149
Figure 6.13 Radial total pressure profiles at Rotor 2 exit for six clocking configurations at L3 ........................................................................................................ 149

Figure Page

Figure 6.14 Radial total pressure profiles at Rotor 2 exit for six clocking configurations at L6 ........ 150
Figure 6.15 Radial total pressure profiles at Rotor 2 exit for six clocking configurations at L7 ........ 150
Figure 6.16 Radial total pressure profiles at Rotor 2 exit for six clocking configurations at L8 ........ 150
Figure 7.1 Stator 2 static pressure distribution at (a) 50%span and (b) 80%span for the peak efficiency and high loading conditions ........ 153
Figure 7.2 Stator 2 static pressure distribution at 80%span with bars showing scale of (a) RMS and (b) vane clocking effects scaled ........ 154
Figure 7.3 Change in Stator 2 static pressure differential between vane clocking configurations for (a) 50%span and (b) 80%span at six loading conditions 155
Figure 7.4 Suction surface pressure coefficient with Rotor 2 blade passing at high loading (L7) for (a) 50%span and (b) 80%span ........ 159
Figure 7.5 Cp and RMS for an average Rotor 2 blade pass on the suction surface at 10% axial chord for the L7 loading condition at (a,b) 50%span and (c,d) 80%span ........ 160
Figure 7.6 Cp and RMS for an average Rotor 2 blade pass on the pressure surface at 10% axial chord for the L1 loading condition at (a,b) 50%span and (c,d) 80%span ........ 160
Figure 7.7 Cp and RMS for an average Rotor 2 blade pass and the Fourier transform of Cp at 10% axial chord for the L7 high loading condition at 80%span for CL2 and CL5 ........ 162
Figure 7.8 Changes in FT magnitude at blade pass frequencies with clocking configuration for L7, at 10%$c_x$ suction side ........ 163
Figure 7.9 st-diamagrams of normalized QWSS for six clocking configurations at peak efficiency (L3) ........ 168
Figure 7.10 QWSS response at 8%ss for six clocking configurations at peak efficiency (L3) ........ 169

Figure Page

Figure 7.11 Mean Rotor 2 blade pass of QWSS response at 8%ss for six clocking configurations at peak efficiency (L3)........................................................ 170
Figure 7.12 Mean Rotor 2 blade pass of QWSS response at 8%ss for six clocking configurations at higher loading (L5)......................................................... 170

Appendix Figures

Figure A.1 Stator 1 Vanes with Downstream Instrumentation....................................... 186
Figure A.2 Stator 2 Vanes with Downstream Instrumentation....................................... 187
Figure A.3 Stator 3 Vanes with Downstream Instrumentation....................................... 187
Figure B.1 Gallery of Fluid Motion 2015 Submission................................................... 188
Figure C.1 Kiel-head geometry considerations ............................................................. 191
Figure C.2 Stator 2 insert model with routing holes and connector configuration......... 193

# NOMENCLATURE

| Symbol | Description |
|---|---|
| A | area |
| a | speed of sound |
| bp | blade passage |
| CFD | computational fluid dynamics |
| CL | clocking configuration |
| $C_P$ | coefficient of pressure |
| $c_x$ | axial chord |
| D | diameter |
| E | voltage |
| IGV | inlet guide vane |
| HL | high loading |
| L | loading condition |
| LE | leading edge |
| $\dot{m}$ | mass flow rate |
| N | rotational speed |
| NL | nominal loading |
| P | pressure |
| PS | pressure side |
| QWSS | quasi-wall shear stress |
| R | rotor |
| RF | radial flow |
| RMS | root mean square |
| S | stator |

| Symbol | Description |
|---|---|
| SN | spiral node |
| SS | suction side |
| T | temperature |
| TC | rotor tip clearance |
| TE | trailing edge |
| U | wheel speed |
| v | absolute velocity |
| vp | vane passage |
| w | relative velocity |
| $Y_P$ | total pressure loss |

Greek

| | |
|---|---|
| $\alpha$ | absolute flow angle |
| $\beta$ | relative flow angle |
| $\gamma$ | ratio of specific heats |
| $\Pi$ | non-dimensional Pi parameter |
| $\rho$ | density |
| $\tau_w$ | wall shear stress |

Subscripts

| | |
|---|---|
| 0-9 | axial measurement positions |
| act | actual conditions |
| c | corrected conditions |
| ideal | ideal flow assumption |
| in | inlet conditions |
| mech | mechanical speed |
| o | stagnation conditions |
| real | real flow assumption |
| ref | reference conditions |

# ABSTRACT

Smith, Natalie Rochelle. Ph.D., Purdue University, May 2015. An Experimental Study on the Effects of Blade Row Interactions on Aerodynamic Loss Mechanisms in a Multistage Compressor. Major Professor: Nicole Key.

While the gas turbine engine has existed for nearly 80 years, much of the complex aerodynamics which governs compressor performance is still not well understood. The unsteady flow field consists of periodic blade row interactions from the wakes and potential fields of each blade and vane. Vane clocking is the relative circumferential indexing of adjacent vane rows with the same vane count, and it is one method to change blade row interactions. Though the potential of performance benefits with vane clocking is known, the driving flow physics have yet to be identified.

This research examines the effects of blade row interactions on embedded stator total pressure loss and boundary layer transition in the Purdue 3-stage axial compressor. The inlet guide vane, Stator 1, and Stator 2 all have 44 vanes which enable vane clocking of the embedded stage, while the rotors have different blade counts producing amplitude modulation of the unsteady interactions.

A detailed investigation of corrected conditions is presented to establish repeatable, compressor performance year-round in a facility utilizing ambient inlet conditions. Without proper humidity accounting of compressor corrected conditions and an understanding of the potential for inlet temperature changes to affect clearances due to

thermal growth, measurements of small performance changes in detailed research studies could be indiscernible.

The methodology and implementation of a powder-paint flow visualization technique along with the illuminated flow physics are presented in detail. This method assists in understanding the loss development in the compressor by highlighting stator corner separations and endwall flow patterns. Effects of loading condition, rotor tip clearance height, and stator wake and rotor tip leakage interactions are shown with this technique.

Vane clocking effects on compressor performance were quantified for nine loading conditions and six clocking configurations – the largest vane clocking dataset in the open literature. These data show that vane clocking effects are small at low loading conditions, including peak efficiency operation, but become stronger as loading increases, and then eventually lessen at near stall operation. Additionally, stator wake profiles and flow visualization reveal that total pressure loss changes are due to a corner separation modulation between clocking configurations.

To further address these clocking trends, high-frequency response data were acquired at the Stator 2 inlet and along the Stator 2 surface. The unsteadiness at the Stator 2 inlet was quantified with detailed radial traverses for the different clocking configurations. These data show the effects of interactions between the Stator 1 wake and Rotor 2 tip leakage flow, which result in significantly different inlet flow conditions for Stator 2. The high unsteadiness and blockage region formed by the rotor tip leakage flow changes in size and shape between clocking configurations. Finally, measurements of the Stator 2 surface flows were acquired to investigate the vane clocking effects on unsteady

surface pressures and boundary layer transition. These data reveal that Stator 2 performance is influenced by blade row interactions including rotor-rotor interactions, stator wake-rotor tip leakage flow interactions, and vane clocking.

# CHAPTER 1. INTRODUCTION

Gas turbine engine designs and technologies have advanced to a point where even tiny gains in efficiency are noteworthy and have both environmental and fiscal implications for engine companies. These incremental steps are achieved through thorough evaluation of all engine components. An improvement of one point high pressure compressor (HPC) efficiency can reduce the cruise SFC of a high bypass engine by 0.66 percent (Wisler, 1998).

To achieve these incremental improvements in compressor efficiency, major loss mechanisms (rotor tip leakage, corner separation, seal leakages, etc.) must be better understood so that they may be accurately modeled during the design process. While the advancement of computational abilities allows the compressor designer to evaluate many design concepts without testing, these studies are only useful if there is confidence in the code’s ability to accurately capture the details of the flow physics. Boundary layer transition and corner separations are crucial to correctly predicting the profile loss through a compressor and are affected by both the steady and unsteady effects of the surrounding blade row interactions. Thus, the flow field arising from complex interactions between rotating and stationary blade rows in turbomachinery must be interrogated in experiments, so that codes may be calibrated.

## 1.1 Aerodynamics Forcing Functions

The periodic disturbances created by the relative motion between stationary vane rows and rotating blade rows in axial compressors include potential fields and wakes, as shown in Figure 1.1. Although not discussed in this study, shocks are also an aerodynamic forcing function in some flow regimes. The periodic disturbances created by these interactions can result in blade vibration, increased discrete frequency noise, and change aerodynamic performance. When these disturbances occur at a frequency similar to that of a vibrational mode of a blade, then forced response vibrations can occur and even lead to high cycle fatigue and blade failure. Furthermore, these interactions have profound effects on not only on unsteady performance aspects including, lift and boundary layer development, but also affect the time-averaged performance.

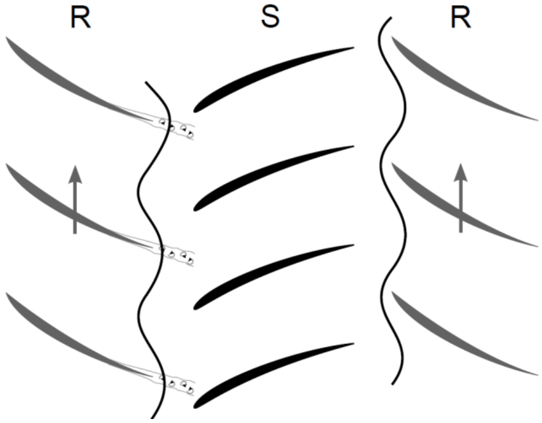

Figure 1.1 Aerodynamic forcing functions

### 1.1.1 Potential Fields

The potential interactions are the inviscid aerodynamic forcing function component and are caused by the pressure field associated with each blade’s thickness and camber. Although, they propagate both upstream and downstream, their strength decays exponentially with distance, typically only affecting the adjacent row (Johnston et al., 1998). Hall (1998) showed that when a rotor blade passes near the downstream stator's leading edge, it performs additional work to attain the higher static pressures near the stator leading edge. In a computational study, Graf et al. (1999) studied the effects of the downstream stator pressure field on the upstream rotor. They found that compared to an isolated rotor at the same overall pressure rise, the backpressure imposed by the downstream stator caused up to 40% variation in time-averaged rotor loss. These variations were most significant at the tip endwall due to the effects on the leakage vortex. While the effects of the potential fields contribute to aerodynamic forcing, often they are less significant than other interactions present in this complex flow field.

### 1.1.2 Wakes

Wakes, the vortical forcing function, originate from the shedding of a blade's viscous boundary layer. The velocity deficit that characterizes the rotor wake fluid in the relative reference frame results in an increased flow angle in the absolute reference frame. Therefore, the downstream stator will experience an increase in incidence when the rotor wake passes, leading to an unsteady lift force on the vane. The same effect occurs when considering the stator wake fluid as seen by the downstream rotor; the velocity deficit in the absolute reference frame becomes an increase in relative flow angle, $\beta$. Velocity triangles depicting these changes are shown in Figure 1.2. Wakes can persist for many stages downstream, interacting with blade rows and other wakes and flow features.

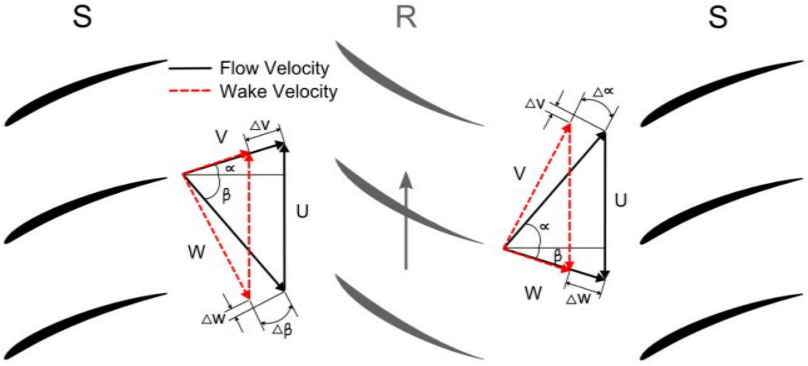

Figure 1.2 The effect of a velocity deficit in one reference frame on the downstream row in another reference frame

Several researchers have studied wakes in turbomachinery to better understand the viscous loss mechanism. Raj and Lakshminarayana (1973) presented cascade data where they examined the wake decay characteristics for the near and far wake. Further details about the near wake region have been reported by Reynolds et al. (1978). Kerrebrock and Mikolajczak (1970) showed that stagnation temperature measured at the exit of the downstream stator can be used to estimate the viscous losses of the rotor due to the energy transport of the rotor wakes through the stator passage. Smith (1966) introduced the concept of wake recovery, and Adamczyk (1996) explained how the rotor wake recovery process is connected to the change in kinetic energy across the stator passage. Others have used numerical simulations to investigate the tradeoff between mixing losses and inviscid wake stretching (Deregel and Tan, 1996; VanZante et al., 2002).

The wake’s role as a forcing function for vibrations on the downstream vane row is often considered using an average, representative wake. Variations in compressor hardware due to machining tolerances or wear, in addition to blade row interactions, introduce differences in wakes, and this is commonly referred to as wake variability. These effects are often not accounted for in CFD nor quantified in experiments.

Wake variability has been assessed both experimentally and numerically by a few authors. Garzon and Darmofal (2003) used a high-fidelity, probabilistic analysis to model the impact of geometric variability on compressor aerodynamic performance. Their results showed that manufacturing variability can affect the mean passage flow enough to reduce efficiency by up to one point. They showed that the variance in leading-edge geometry is a major factor resulting in changes in passage loss. Key et al. (2004) used particle image velocimetry to identify large scale structures shed from a rotor blade which strayed from the average wake convection path and connected this deviation to non-uniform hub leakage flow caused by mass removal on the balancing ring.

The work of Sherman et al. (1996) used a mean wake analysis to show the need to consider individual blade variability, as the mean wake was only representative of about half the rotors in their single-stage compressor. Similarly, Boyd and Fleeter (2003) found that less than 50% of the rotor wakes in their facility fell within the confidence level of the grand mean average wake. Furthermore, this variability resulted in differences in aerodynamics response by as much as 100%. Key et al. (2010) used different averaging techniques to isolate variability effects locked to the rotor revolution versus the stator pitch for all three rotors in a three-stage compressor focusing on the variability associated with blade row interactions. Sanders and Fleeter (2002) evaluated the blade-to-blade variability in a 1.5 stage high-speed compressor and showed that the clocking of the inlet guide vane (IGV) had a profound effect on how the chopped IGV wakes would combine with the rotor wakes and change the forcing on the downstream stator. At off-design conditions, they observed that even small rotor wake variability could result in large differences in unsteady lift on the downstream stator.

### 1.1.3 Additional Aerodynamic Forcing

In addition to the rotor wake, the rotor tip leakage flow is an important unsteady flow feature that provides an aerodynamic excitation to the downstream vane row. The tip leakage vortex has received a lot of attention due to its effect on performance, including loss and stability. In general, authors have observed that for every 1% increase in tip clearance, there is a 1% reduction in efficiency (Wisler, 1985). Furthermore, as tip clearance increases, stall margin is reduced (Wisler, 1985; Day, 1993).

Some authors have also identified interactions between the development of the rotor tip leakage vortex and the incoming stator wakes. The experimental investigation by Mailach et al. (2008) was the first to identify the interaction between the stator wake and the rotor tip leakage vortex. Laser Doppler Anemometry measurements revealed that the stator wake caused time-dependent changes in the position and intensity of the rotor tip leakage vortex. Similarly, Krug et al. (2014) investigated the effects of unsteady wake passing in a cascade where cylindrical bars were used to generate unsteady wakes. They showed that the secondary flows, including tip leakage vortices, were highly dependent upon the upstream wake position.

## 1.2 Blade Row Interactions

The potential fields from adjacent airfoil rows and the wakes shed from upstream airfoil rows generate periodic disturbances that impact aerodynamic performance. The combination of these effects in a multistage environment adds complexity. The following discussion will focus the effects of blade row interactions on performance for rotor-rotor interactions with varying blade counts and stator-stator interactions with equal vane counts between rows.

### 1.2.1 Rotor-Rotor Interactions

When blade counts of adjacent rotor rows differ, rotor-rotor wake interactions result in a beating pattern based on the difference in blade counts of adjacent rotor rows (Cherrett and Bryce, 1992). This is depicted in Figure 1.3 for two rotor rows which differ in blade count by 3. This results in a 3/rev beating because there are three locations circumferentially where the wakes from the upstream row align with those of the downstream row; and there are locations were the rotor wakes are out-of-phase. Experimental results in a multistage research compressor with 70 Rotor 1 blades and 72 Rotor 2 blades showed a two node-per-revolution pattern in axial velocity (Prato et al., 1998). Williams (1998) measured a four-cycle-per-revolution beat frequency at the Stator 9 exit associated with the 66 bladed Rotor 9 flow field interacting with the 62 bladed Rotor 10 flow field. A Fourier transform of the data showed that many more rotors than the immediate upstream and downstream rotors were contributing to the fluctuating velocity field. In fact, at the Rotor 10 inlet plane, periodic contributions from Rotor 6 were present. This phenomenon is not particular to compressors. Beat frequencies associated with the difference in adjacent blade counts were measured in a five-stage low-pressure turbine research facility (Binder et al., 1989 and Arndt, 1993). This beat frequency is also evident in the surface hot-film measurements of the boundary layer data acquired on the third vane row in a high-speed low pressure turbine (Howell et al., 2002). Thus, these interactions of the surrounding rotor blade rows are important to consider when evaluating the time-resolved response of the boundary layer development.

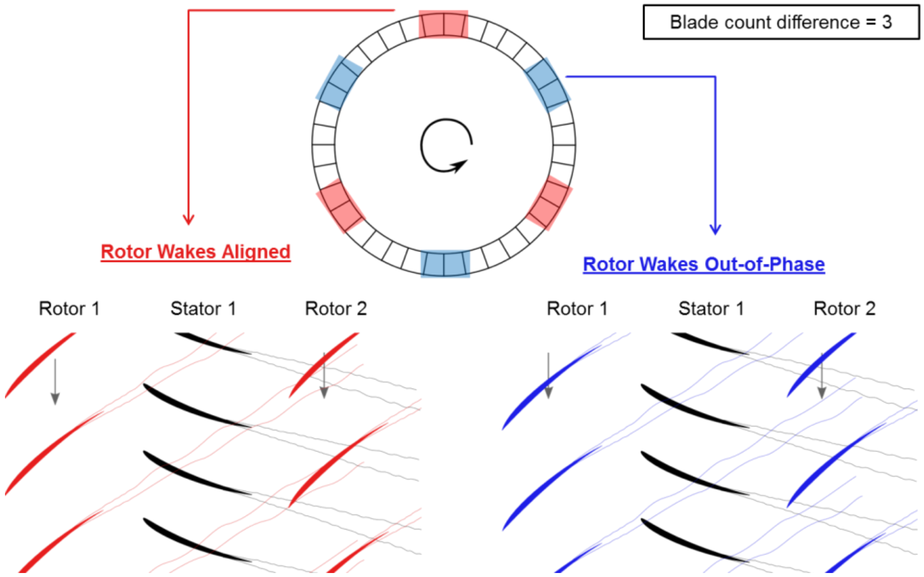

Figure 1.3 Interactions between rows with different rotor blade counts cause a constructive and destructive beating pattern

### 1.2.2 Stator-Stator Interactions and Vane Clocking

Vane clocking, the circumferential indexing of adjacent vane rows with the same vane counts, affects blade row interactions in turbomachines. Researchers have shown that vane clocking has an effect on stage efficiency, forced response, and propagation of tonal noise. Figure 1.4 illustrates how an upstream vane row in a multistage compressor may be indexed to different circumferential positions to change the alignment of its wake with respect to the downstream vane row. The position of the upstream vane row is adjusted to a different circumferential position, as shown by the difference in position of the filled and outlined upstream stators. The clocking configuration or clocking offset (CL) is defined as the difference in the upstream vane position with respect to the downstream vane position. The configuration shown by the solid black vanes has a clocking offset of zero. The configuration shown by the outlined vanes has a clocking offset of 25% vane passage (vp). Often, two specific clocking configurations are of particular interest: 1) the configuration that places the wake from the upstream vane row at the leading edge of the downstream vane, referred to as $CL_{LE}$, and 2) the configuration where the wake from the upstream vane row passes through the middle of the downstream vane row passage, referred to as $CL_{MP}$.

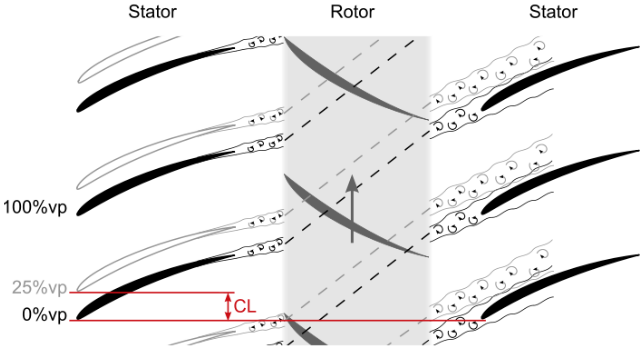

Figure 1.4 Example of vane clocking where clocking offset (CL) is defined as the difference between the upstream and downstream vane positions

#### 1.2.2.1 Turbine Performance

Much of the available clocking literature involves turbine applications, where as much as a 2% stage efficiency benefit has been observed with optimal clocking (Huber et al., 1996; Jouini et al., 2003; Reinmöller et al., 2002). These turbine experiments are supported by computational clocking studies (Dorney and Sharma, 1996 and Reinmöller et al., 2002) which show the potential for changes in stage efficiency from 0.7-2% with vane clocking. Huber et al. (1996) is one of the first such studies to investigate vane clocking effects on the performance of a two-stage turbine showing 0.3 points average efficiency difference between the maximum and minimum efficiency clocking configurations. Closer examination of local spanwise efficiencies reveals that local spanwise efficiency can vary by nearly 1 point, but these variations diminish when averaged over the entire span. Furthermore, it is generally agreed that for turbines, the $CL_{LE}$ clocking configuration is the most efficient case, and the $CL_{MP}$ clocking configuration is the least efficient.

#### 1.2.2.2 Compressor Performance

The first studies (Walker and Oliver, 1972; Schmidt and Okiishi, 1977; Kamiyoshi and Kaji, 2000) of vane clocking in compressors investigated the effect of clocking on tonal noise propagation, where changes on the order of 10-15db were reported. Vane clocking also has a significant effect on the unsteady rotor blade loading (Hsu and Wo, 1998; Mailach and Vogeler, 2004). The relative position of the upstream potential and vortical disturbances with respect to the downstream potential fields can have a strong effect on the embedded rotor unsteady lift. Vane clocking studies on compressor performance are less common because changes are more difficult to observe and measure in low-speed compressors due to lower pressure rise. Other early experiments (Hsu and Wo, 1998; Capece et al., 1989) exploring the effects of blade row interactions in compressors identified the potential for vane clocking to alter stage performance, which is the focus of the present work. Numerical studies, like those of Gundy-Burlet and Dorney (1997), were of the first compressor studies to emerge and had findings similar to the turbine literature of a nearly sinusoidal variation between maximum and minimum clocking locations.

Barankiewicz and Hathaway (1997) measured small changes in overall loss coefficient with clocking in the NASA Four-Stage Axial Compressor Facility, but these differences were considered to be small and within the manufacturing and assembly tolerances of the compressor. This research did observe that the maximum performance clocking position was dependent upon the operating condition, and furthermore, the clocking effects were larger at the higher loading condition. Detailed hot wire measurements acquired downstream of the stator in a 1.5 stage axial compressor by Walker et al. (1997) showed that the $CL_{LE}$ clocking configuration resulted in a 10% lower peak momentum thickness for the downstream stator suction side boundary layer, but the time-mean results showed no conclusive trend in stator loss reduction with vane clocking.

The work of Saren et al. (1997) is one of the few high-speed clocking experiments in the open literature, and the measured change in average stage efficiency was 1%, but local spanwise efficiency changes were as large as 7-8%. The larger local changes occurred in the endwall regions where the incoming IGV wakes were larger. The computational study that accompanied this work showed that the $CL_{LE}$ configuration provided the maximum stage efficiency, in agreement with the turbine literature. The computations also showed vane clocking to be effective at a near stall loading condition.

Key et al. (2010) measured a change in stage efficiency with clocking in the embedded stage of an intermediate-speed three-stage compressor. This vane clocking study included both the design point and a high loading condition. Results at design point showed that the Stator 2 losses were minimized when the wakes from Stator 1 impinged on Stator 2, $CL_{LE}$. Clocking configurations which placed the Stator 1 wake in the mid-passage region of Stator 2 showed the largest Stator 2 loss and was 0.3 efficiency points lower than clocking configuration $CL_{LE}$. This result is similar to the results reported by researchers studying vane clocking effects on turbines. However, at a high loading condition, leading edge impingement of Stator 1 wakes on Stator 2 resulted in the worst efficiency, and the overall change in efficiency between $CL_{LE}$ and $CL_{MP}$ clocking configurations at this high loading condition was one point. This supports previous observations that vane clocking effectiveness, including the impingement condition related to the maximum efficiency configuration and the change in efficiency between maximum and minimum configurations, depends on compressor loading conditions.

Städing et al. (2011) observed opposite trends from previous authors, where they found the $CL_{MP}$ clocking configuration to be the most efficient. They measured a consistent 0.2% change in overall efficiency for a 2.5-stage low-speed compressor over three loading conditions: low loading, design point, and high loading.

Some authors (Saren et al., 1997; Mailach and Vogeler, 2004) have identified changes in the rotor flowfield character due to vane clocking, but none have drawn conclusions connecting rotor performance differences with vane clocking with the efficiency changes. Results from Key (2013) showed that the change in compressor efficiency associated with vane clocking is caused by losses on the downstream vane. Rotor loss, as measured by detailed traverses of stagnation temperature and also absolute flow angle, was unchanged by vane clocking.

#### 1.2.2.3 Flow Physics

While some trends between upstream wake location and resulting efficiency benefit has emerged from experimental and numerical studies alike and several authors have noted the dependence on loading condition, a finite explanation of the defining flow physics behind vane clocking has not been achieved. Through detailed flow field investigations, two general hypotheses have developed from observations of the unsteady aspects of the flow field: unsteady surface pressures (Griffin et al., 1996; Dorney et al., 1998) and boundary layer response (Walker et al., 1998; Key et al., 2008; Konig et al., 2009).

Some authors believe the movement of the upstream vane wake impingement affects the unsteadiness of the surface pressure, which leads to an efficiency change. Dorney and Sharma (1996) found the maximum efficiency configuration, which was two points higher than the minimum, exhibited more pressure unsteadiness along the suction side surface near the leading edge through numerical computations on 1.5 stage axial turbine. In a numerical study of a low-pressure turbine, Arnone et al. (2002) also showed that the maximum efficiency configuration had higher static pressure disturbances. Gundy-Burlet and Dorney (1997) found similar results in a 2-stage axial compressor computational study. Dorney et al. (1998) used a numerical investigation of unsteady pressures on the second stage stator of a 1.5 stage compressor to reveal the combination of steady and unsteady effects on Stator 2. At the higher efficiency clocking configuration, the Stator 2 suction side had higher unsteadiness and contained higher frequency content. They suggested this was caused by the Stator 1 wake vorticity introduced at the leading edge.

The other hypothesis focuses on the changes in boundary layer response to rotor wake chopping. Walker et al. (1997) measured the momentum thickness of the $CL_{MP}$ configuration to be generally 10% higher than the $CL_{LE}$ configuration. The higher momentum thickness should leave the leading edge impingement case more resistant to separation. This is further supported by stator wake unsteadiness findings in which $CL_{LE}$, the maximum efficiency configuration, consistently showed less wake unsteadiness suggesting that the upstream vane wake helps stabilize the unsteady boundary layer transition from the periodic rotor wakes.

Unsteady measurements acquired at Stator 2 exit in the study by Key et al. (2008) led the authors to hypothesize that at design point, the Stator 1 wake dampens the Stator 2 boundary layer response to Rotor 2 wake chopping. At high loading, this same configuration causes boundary layer separation on the suction side of Stator 2. A frequency analysis focusing on the blade pass frequency associated with the upstream blade row was used to identify these trends in the unsteady data and to infer information about the Stator 2 boundary layer response to the rotor wakes. Also, the Stator 1 wake impingement on the leading edge of Stator 2 caused the energy related to the Rotor 2 blade pass frequency to be pushed to higher frequencies similar to the findings of Dorney et al. (1996). The unsteady data acquired by these researchers within the downstream stator wake suggest the leading edge impingement configuration suppresses the vane’s response to the rotor wake passing, allowing it to perform more efficiently. However the evidence of the defining flow physics is missing, and an investigation of the downstream stator’s boundary layer would confirm these hypothesizes.

## 1.3 Boundary Layer Development

The ability to predict boundary layer transition, including the position along the blade at which it occurs and the length of the transition region, is important for correctly predicting the profile loss of a blade. In general, transition from laminar to turbulent flow occurs through the development of turbulent spots, which spread as the flow moves downstream. As presented by Mayle (1991), there are three different modes by which a boundary layer transitions from laminar to turbulent. Natural transition typically occurs when there are low levels of freestream turbulence, and the process begins with a weak instability in the laminar boundary layer eventually leading to a turbulent boundary layer. Bypass transition occurs when there are significant disturbances in the flow field that trigger transition. The term bypass is used because the process seems to ‘bypass’ the initial stages of the natural transition mode. Finally, separated flow transition occurs if the laminar boundary layer separates and reattaches as a turbulent boundary layer. Many aspects of the flow and geometry affect boundary layer development and include Reynolds number, freestream turbulence levels, the blade surface pressure distribution, leading edge shape, and surface roughness (Mayle, 1991).

### 1.3.1 Multimodal Transition

Transition on a turbomachinery airfoil is also influenced by the periodic impingement of wakes shed from the upstream blade row. As discussed earlier, the velocity deficit from the passing wake from an upstream row becomes an increase in incidence to the downstream row, as shown in Figure 1.2. The upstream wake fluid also contains higher turbulence. Both the change in incidence and the change in turbulence intensity affect the boundary layer development of the downstream row with each wake passing. Halstead et al. (1997) showed that for both turbines and compressors, two distinct regions of boundary layer development occur on a turbomachinery airfoil: a region through the wake path and a region between the wakes. These regions are typically discussed using space-time (st)-diagrams, like shown in Figure 1.5. They allow for visualization of these two paths of boundary layer development, where “I” denotes the wake-induced oath and

“II” is the path between the wakes. In this schematic, region A represents laminar flow, B and E are transitional flow, and C and F regions with a turbulent boundary layer. Therefore, both wake-induced transition and the transition method for the undisturbed vane can coincide on the same vane, continuously varying the location of transition onset and the length over which transition occurs. If turbulence levels in the wake are very high, the turbulent spots may merge and form a sort of turbulent strip. Outside of the zone of wake influence, natural transition can occur. Hughes and Walker (2001) discovered evidence of natural transition in the last stator of a 1.5 stage compressor. Evidence for Tollmien-Schlichting waves was discovered using significant data processing efforts to identify these small amplitude instabilities. Thus, turbomachines often feature ‘multimodal’ boundary layer transition (Mayle, 1991).

After the rotor wake passing event, a calmed region noted as region D in Figure 1.5, characterized by high but decreasing shear stress, is observed. The high level of shear stress helps the boundary layer become more resistant to transition. Schubauer and Klebanoff (1956) first noted a calmed region that occurred after a turbulent spot on a flat plate. The region is very stable, not affected by disturbances, and able to resist boundary layer separation in strong adverse pressure gradients. The calmed region is not like a conventional laminar boundary layer. It is quite thin and has a nearly linear velocity profile. After some time, the calmed region further relaxes and takes on a more conventional parabolic laminar velocity profile (Dong and Cumpsty, 1990, Part 1 and 2). There exists some disagreement in the literature regarding the source of the calmed region. Some authors believe the calmed region occurs between the passing of the rotor wake centerline and the trailing boundary of the rotor wake shed from the suction side of the upstream blade row and associate it with the passing of the rotor wake itself rather than a relaxation occurring after the wake (Mailach and Vogeler, 2004). Most recently, Gostelow et al. (2009) provide evidence to reconcile this disagreement regarding the calmed region in turbomachines. They generated wakes with rods rotating past an instrumented flat plate with a long separation bubble in a strong adverse pressure gradient. They showed that as wake spacing decreased, the relaxing benefits of the calmed region were evident in the reduced disturbance levels. These findings suggest that a calmed region exists following the wake-induced paths in turbomachines even when a classic calming region is undetectable due to wake spacing. Thus, the observations made by Mailach and Vogeler (2004) could be effects of a calmed region, despite the region being within the wake-induced boundary.

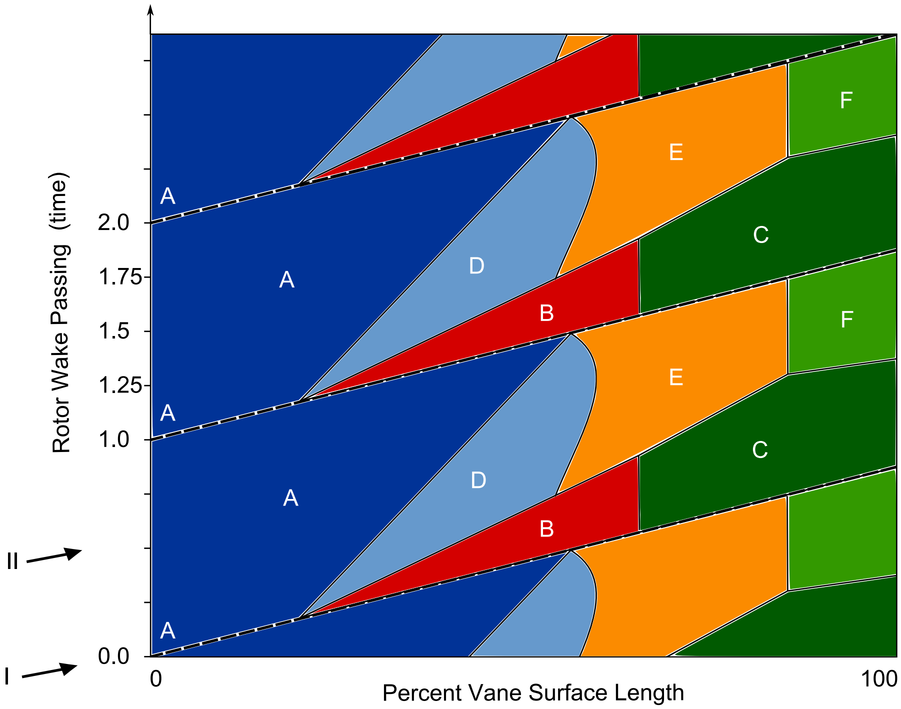

Figure 1.5 Space-time (st) diagram of multimodal boundary layer transition

### 1.3.2 Boundary Layers in Turbomachinery

Several researchers have studied the boundary layers of embedded stages in low pressure turbines, and Hodson and Howell (2005) provide a good review of this work. Fewer studies have focused on boundary layer measurements in compressors, where the adverse pressure gradient has a strong effect on boundary layer transition. Halstead et al. (1997) observed the difference in transition for turbines and compressors, which agrees with work from Gostelow and Walker (1990) in that the presence of an adverse pressure gradient shortens the length of transition and increases the production of separation bubbles. Dong and Cumpsty (1990, Parts 1 and 2) provided one of the first detailed boundary layer studies in an adverse pressure gradient including the effect of upstream wakes. They used moving cylindrical rods to generate wake-like disturbances on the downstream large-scale vanes in a cascade. When the wakes impinged on the vane, turbulent spots appeared near the leading edge and behaved similar to a turbulent spot in a transitional boundary layer on a flat plate (Dong and Cumpsty, 1990, Parts 1 and 2).

Walker et al. (1999) investigated suction side stator boundary layer transition in a single stage compressor consisting of an IGV-rotor-stator. They explored the effect that the time-averaged vane pressure distribution had on transition by changing the incidence on the vanes. They also explored the effect that the freestream turbulence level had on transition by clocking the upstream IGV so that the IGV wake provided additional unsteadiness to the downstream vane. These effects increased with loading and were most important when transition occurred via a separation bubble near the leading edge. When transition occurred via a mid-chord separation bubble, there was little difference between the cases (Walker et al., 1999). Mailach and Vogeler (2004) investigated the boundary layer response on the first stage stator vane in a low-speed research compressor with results showing movement of the transition zone up to 80% of the chord due to wake-induced transition. In both of these studies, the effects of the wakes from the upstream rotor were captured in a rotating rig environment.

Halstead et al. (1997) acquired shear stress data on the first and third rotor of a 4-stage low speed research compressor featuring repeating stages. Thus, he was able to contrast results of boundary layers from the first rotor (without any upstream vane influence) with results from the third rotor which was influenced by several upstream vane rows and wakes. The 4-stage compressor featured repeating stages where the vane counts were identical for every stage, as were the rotor counts. Consequently, the contributions from the different upstream stages were difficult to discern because of the similar blade counts.

## 1.4 Flow Separation

Flow visualization techniques have been used to enhance the understanding of complex fluid flows since the beginning of fluid mechanics. The qualitative observations that inspired theories from early scientists (Richter, 1883) are echoed by modern researchers still evaluating the complex fluid structures that govern modern day technical challenges.

Some of the most complicated flow fields include those found in turbomachinery, where flow structures including wakes, passage vortices, tip leakage vortices, and boundary layer separations interact in the unsteady flow field. These flow structures must be understood and well predicted for future turbomachines to maintain high efficiency, low fuel burn, and low weight – all important design objectives, especially for the gas turbine engine used to power aircraft. The designers’ toolbox consists of a wide array of computational methods, from reduced order models to full 3D unsteady computational fluid dynamics (CFD). Each tool has its place in the design system and relies on different levels of modeling to obtain useful solutions. The steady Reynolds-Averaged Navier-Stokes solvers have been favored for use in the design iteration loop because of their quick convergence. These solvers rely on turbulence models and typically show good agreement to experimental data at design conditions with well-behaved flow fields. However, at off-design conditions, where boundary layer separations are more common, these codes can be less reliable (Cumpsty, 2004; Denton, 2010). If a code does not correctly predict boundary layer separation, then the blockage will be incorrect resulting in differences with stage matching, and these errors are compounded in the multistage environment.

Three-dimensional separations are fundamentally different from their two-dimensional counterparts in a couple ways: (1) their formation can occur at non-zero surface and without reversed flow (Chang, 1970), and (2) many of the separations are independent of Reynolds number (Délery, 2001). A particularly interesting three-dimensional flow separation common to compressors occurs at the junction of the suction surface (SS) of a shrouded vane and the endwall, typically called a corner separation. There are two types of stators used in compressors: shrouded and cantilevered. Cantilevered stators are fixed to the casing endwall and feature a small gap at the hub between the vane and rotating rotor drum, and thus, a corner separation will only occur in the tip region of these vanes. For shrouded stators, the hub of the airfoil is fixed to a platform, or ring, which connects to all vanes. The bottom of a single shrouded stator and its passage are shown in Figure 1.6a, with flow going from left to right. There are two main flow features which drive the formation of this separation. First, the inherent streamwise pressure gradient in compressors causes the boundary layer along the vane suction surface to grow thick and be susceptible to early boundary layer separation. Secondly, the endwall flow in the vane passage experiences a cross flow pressure gradient as a result of the flow moving through a curved passage. This causes the low momentum fluid of the endwall to move across the passage from the pressure surface of one vane toward the suction surface of the adjacent vane (Mertz, 1954; Horlock et al., 1966). The intersection of the secondary flow of the endwall boundary layer and the boundary layer developing on the suction surface of the vane creates a weakened flow region which is prone to three-dimensional separation, illustrated in Figure 1.6a. These separations contribute significantly to the formation of blockage and total pressure loss in axial compressors and thus, reduce efficiency and increase deviations in stage matching at off-design conditions (Cumpsty, 2004). At high loading conditions the endwall boundary layers suffer from increased adverse pressure gradient. Also, the vane boundary layers experience stronger incoming rotor wakes, and this causes the vane’s suction side boundary layer transition to move forward toward the leading edge (Halstead et al., 1997).

Qualitative evaluation of these types of flow separation patterns can provide quick and useful insight when experimental data are not matching computational predictions. For example, Miller et al. (2012) used flow visualization to quantify the extent to which the endwall flows were pulled into the main passage by incorporating bow and lean in an advanced outlet guide vane design.  The design was outside of the typical design space, and thus, common design rules regarding the amount of grid resolution in the radial direction was deemed to be too coarse to capture the strong radial flows present in this design. This study is a good example of how flow visualization was used in conjunction with CFD to better understand the flow physics and also the shortcomings of the best practices for utilization of computational tools in the design loop.

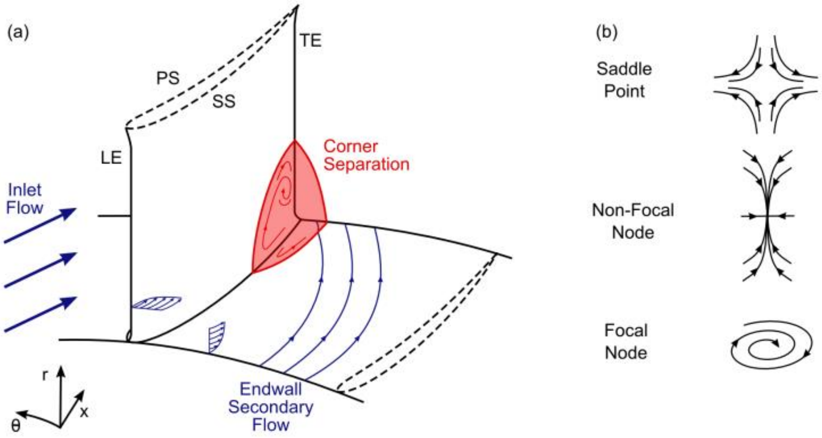

Figure 1.6 Schematics of flow separation features; (a) corner separation forming at the intersection of the stator suction surface (SS) and the hub endwall, (b) separation critical points including a saddle point and two node types

Unlike two-dimensional separations, the flow topology is far more intricate and separation lines are not simply characterized by the shear stress going to zero. Surface streamlines illustrate the flow patterns at a height infinitesimally close to the surface where the flow velocity is zero. In separated flow regions, these patterns consist of lines connecting critical points at which both shear stress vectors ($\tau_x$ and $\tau_y$) are zero. The work of Poincaré (1928) defining singular points in differential equations has been applied to critical points for the Navier-Stokes and continuity equations by several authors (Lighthill, 1963; Tobak and Peake, 1982; Perry and Chong, 1987). All stable and unstable critical points (nodes, focus, saddle points) can be classified based on the determinant and trace of the 2x2 Jacobian matrix which is an approximation of velocity vectors as a function of space coordinates with constant coefficients. Hunt et al. (1978) present an explanation of the relation between critical points and separations. The two critical lines of a saddle point act as separation (the converging branch) and attachment (the diverging branch) lines. Similarly, nodal points with diverging limiting streamlines are points of attachment, while nodal points with converging streamlines are separation points. Figure 1.6b provides examples of the separation versions of these critical points. Furthermore, general rules regarding a flow's "topological class" exist. Most notably of these is the index rule given by Flegg (1974) which provides a relation for number of nodes and saddle points. In a blade passage with no tip gap, the number of nodes and saddle point must be equal, whereas a blade passage with a tip gap will contain two more nodes than saddle points.

While the details of the formation of three dimensional separations are complicated, the experimental techniques to observe these patterns (oil film, paint, tufts) are relatively straightforward. Authors (Dring et al., 1982; Joslyn and Dring, 1985; Dong et al., 1987; Zierke and Straka, 1996; Gbadebo et al., 2005) have used these methods to observe corner separations in a variety of flows for both rotors and stators in compressors and pumps. Authors (Dong et al. 1987; Gbadebo et al. 2005; Gbadebo et al., 2007) have used oil flow visualization in compressor cascades and single stage compressors to compare the development of corner separations on stators with hub clearances and shrouded stators. Generally, much of the available literature does not include experiments in multistage facilities and contains limited discussion and examples of the utility of the technique.

The unsteady flow field present in turbomachinery is characterized by inviscid and viscous blade row interactions. Blade count and alignment between adjacent rotor rows and adjacent stator rows alter aspect of compressor performance. Specifically, vane clocking changes how the wakes from an upstream vane row and interact with the downstream row. The literature lacks conclusive evidence of the flow physics driving the changes in efficiency with vane clocking.

## 1.5 Research Objectives

While the compressor literature agrees that vane clocking results are dependent upon loading conditions, most studies are limited to investigations at a nominal, or design, loading and a single high loading or off-design condition. There also lacks conclusive evidence of the underlying flow mechanism driving the change in efficiency between clocking configurations. Furthermore, as the increase in computational resources allows for multistage calculations to become more common, data acquired in a multistage environment are needed to validate the models and verify that the important flow physics, such as blade row interactions and the unsteady boundary layer development, are captured. Not only are the levels of unsteadiness larger in an embedded compressor stage, but the frequency content of the unsteadiness is markedly different from that of a single stage. Therefore, to address these deficiencies, the objectives of this research were aimed to characterize the steady total pressure loss of an embedded stator with vane clocking and evaluate the effects of blade row interactions on the unsteady Stator 2 inlet flow and surface flows with different clocking configurations.

A detailed investigation of compressor performance repeatability for varying inlet ambient conditions is presented. Relative humidity and inlet temperature are shown to have significant measurable influences on compressor performance and are documented for the first time. Without accounting for these factors, it could be impossible to track small changes in compressor performance due to non-repeatable day-to-day performance.

Powder-paint flow visualization is used to highlight the development of stator corner separations and endwall flows in this compressor over a wide range of loading conditions. This allows for both a qualitative and quantitative discussion of the loss development due to several flow features.

Vane clocking effects on Stator 2 total pressure loss is evaluated in six clocking configurations at nine loading conditions along the 100% speedline. This is the largest vane clocking study in the open literature. Results from peak efficiency to high loading conditions where vane clocking effects become stronger agree with the work of previous authors, but this study shows that as loading is increased closer to near stall, vane clocking effects lessen.

The Stator 2 inlet flow field is characterized with an unsteady total pressure probe. These data reveal strong interactions between the Stator 1 wake and Rotor 2 tip leakage flow, which have significant implications to the blockage and unsteadiness at the Stator 2 inlet flow field. This is the first time these interactions have been tied to vane clocking. Moreover these interactions are shown to affect the downstream stator surface flows with time-resolved measurements of the surface pressures.

The results presented herein not only contribute to a better understanding of vane clocking flow physics, but also illuminate important blade row interactions which must be considered when measuring and modelling these flow fields.

# CHAPTER 2. EXPERIMENTAL METHODS

All research was completed at the Purdue 3-Stage Axial Research Compressor Facility. This chapter covers the details about the research facility and compressor, as well as an overview of the instrumentation and methodology used throughout this research.

## 2.1 Research Facility Overview

The Purdue 3-Stage Axial Compressor Facility is shown in Figure 2.1. This open circuit facility draws air from atmosphere through screens and into a settling chamber that is 8 ft in diameter and 20 ft long. Air enters the 24-in diameter inlet duct through a bellmouth, followed by honeycomb, and is metered with an ASME standard long-form venturi. An area-reducing nosecone accelerates the flow to the constant area annulus at the inlet of the compressor. Approximately 20 chord lengths downstream of the compressor exit, a sliding gate valve is used to back pressure the compressor before the air enters a scroll collector and is exhausted out the side of the facility. The compressor is driven by a 1400 hp AC motor, of which the output shaft is connected to a 5:1 speed increasing gearbox. An encoder on the motor shaft maintains the shaft speed within 0.1% of the desired speed with feedback control.

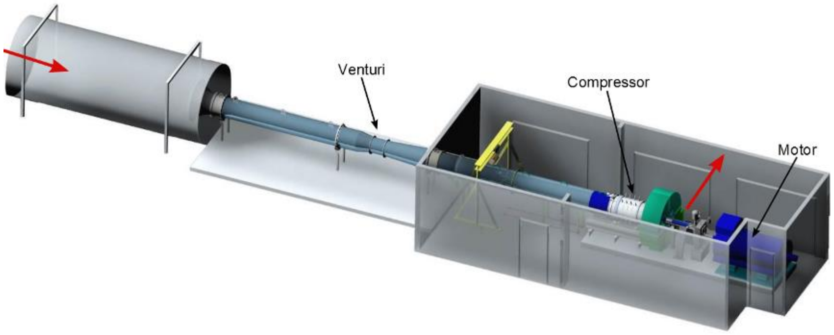

Figure 2.1 The Purdue three-stage axial research compressor facility

## 2.2 Purdue 3-stage Axial Research Compressor

The research compressor is a scaled-up model of the rear stages of a HPC and operates at engine representative Reynolds Numbers and Mach Numbers. The design corrected speed is 5000 rpm. The flow path consists of an inlet guide vane (IGV) followed by three stages, as depicted in Figure 2.2. The IGV and rotor airfoils are double circular arc designs and the stator airfoils are NACA 65-series. The rotor blade counts decrease by three through the machine: 36, 33, and 30, respectively. The IGV, Stator 1, and Stator 2 rows each have 44 vanes, and Stator 3 has 50. All four vane rows are individually indexable, allowing for 20 degrees of circumferential traverse range (2.4 vane passages), for circumferential probe traverses and vane clocking studies. By using precision string potentiometers, the vane positioning system's repeatability is better than 0.1% of the vane passage. The vane clocking portion of this study will focus on the embedded stage, which generates a total pressure ratio of about 1.1 and has an average diffusion factor of approximately 0.47 at the peak efficiency operating condition. Stator 2 turns the flow 30 degrees, has an inlet Reynolds number based on chord of 4.6 x $10^5$, and an inlet Mach number of 0.34 at peak efficiency. These values along with those for the other stator rows are summarized in Table 2.1. Further details on the compressor can be found in Fulayter (2004), Brossman et al. (2011) and Ball (2013).

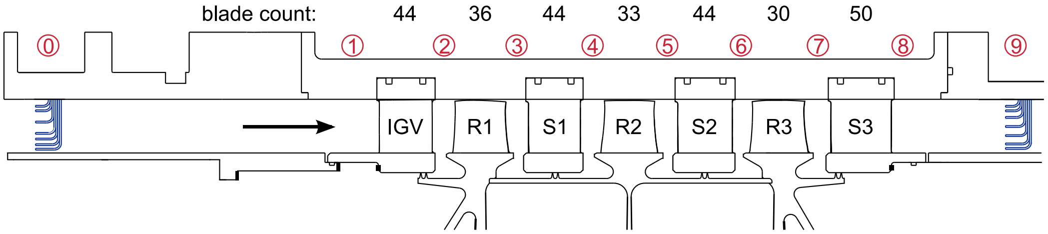

Figure 2.2 The measurement stations and blade counts in the research compressor

Table 2.1 Summary of stator flow parameters at peak efficiency loading condition

| | Inlet Mach Number | Inlet Reynolds Number | Solidity | Diffusion Factor |
|---|---|---|---|---|
| Stator 1 | 0.371 | $4.34 \times 10^5$ | 1.35 | 0.464 |
| Stator 2 | 0.347 | $4.57 \times 10^5$ | 1.42 | 0.459 |
| Stator 3 | 0.323 | $4.76 \times 10^5$ | 1.72 | 0.470 |

### 2.3 Clocking Configurations and Loading Conditions of Interest

The vane clocking configurations are defined by a clocking offset (CL) which is expressed as the difference in circumferential location between the upstream and downstream vane rows in terms of percent vane passage (vp),

$$\text{CL} = \text{Stator 1 \%vp} - \text{Stator 2 \%vp} \,. \tag{2.1}$$

For example in Figure 1.4, the red lines marking CL would be a 25%vp clocking offset, because Stator 1 is at 25%vp and Stator 2 is at 0%vp.

Six clocking configurations will be investigated, with clocking offsets of 0%, 15%, 32%, 49%, 66%, and 83%vp and are referred to as CL1, CL2, CL3, CL4, CL5, and CL6, respectively. For vane traverses, a particular clocking configuration was chosen and that relative offset was maintained throughout the traverse array. In every case, the IGV was moved with Stator 1 and Stator 3 was moved with Stator 2. For example, if data were being acquired in CL3 which has an offset of 32%vp, when the IGV and Stator 1 were at 60%vp, then Stator 2 and Stator 3 were at 28%vp. When vane clocking data were acquired without full vane traverse, Stator 2 and Stator 3 remained at 50%vp, while the IGV and Stator 1 were indexed to the desired clocking offset. The position of 50%vp is the nominal vane position placing the vane splitlines in line with the casing splitline, and thus this is the position used when assembling and disassembling the compressor. This position is important because some instrumentation does not allow for vane traversing due to wire routing. Therefore, those studies achieve clocking positions by only moving the other row to achieve the desired offset.

Clocking effects at peak efficiency and a high loading case have been interrogated in detail previously in this facility, and both conditions are known to have measurable and different influences on Stator 2 loss (Key, 2013). Rather than monotonically increasing as the compressor is back pressured to stall, clocking effects peak at some high loading condition and then decrease as the compressor is loaded to stall. Previous work has shown that the stalling mass flow for different clocking configurations were nearly the same and within the uncertainty of the flow rate measurements (Smith and Key, 2013). These previous studies show vane clocking is a viable method to perturb compressor performance in this facility, but they also highlight the sensitivity to loading condition. Therefore, the need exists to better define the operating range in which clocking is most effective and why certain loading conditions behavior differently than others.

Vane clocking effects on stator loss were investigated at nine loading conditions, as shown in Figure 2.3 and labelled L1-L9. These loading conditions are distributed along the 100% speedline from a low loading case (L1), that was about half way between choke and peak efficiency (L3), to a near stall case (L9) at 4% stall margin. The loading conditions also included a point just below and above the peak efficiency point (L2 and L4, respectively), three high loading cases (L5-L7) where the total pressure of the machine was still increasing, and a high loading case at peak pressure rise (L8). The mass flow rates in Figure 2.3 have been normalized by the corrected mass flow rate at the peak efficiency point.

There are also four other loading conditions labelled in Figure 2.3. These operating points correspond to loadings where data were acquired in this research to also supplement other projects. Two of these points match loading conditions used for the vane clocking study: peak efficiency and near stall. The other two are Nominal Loading, located half way between L1 and L2, and High Loading, near L7. Furthermore, some of the data regarding characterizing rotor wakes was acquired at 74%Nc, at two loading conditions: Nominal Loading and High Loading, shown in Figure 2.4. This speed is a near resonance speed for the Rotor 2 first torsion and was part of an aeromechanics study in which the opportunity to gather additional pertinent data was presented. Data at these points were acquired under particular ambient conditions which allowed for safe mechanical speeds while matching the on-resonance aerodynamics with the proper corrected speed.

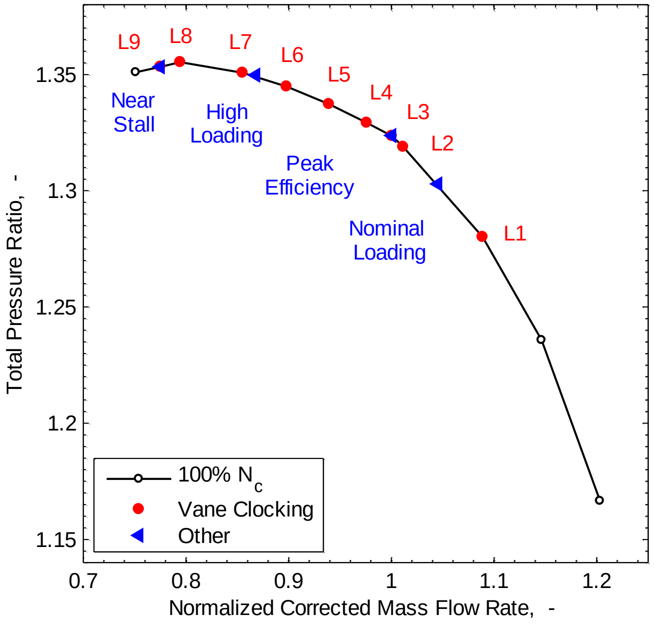

Figure 2.3 100% corrected speedline with loading conditions for vane clocking studies and other work

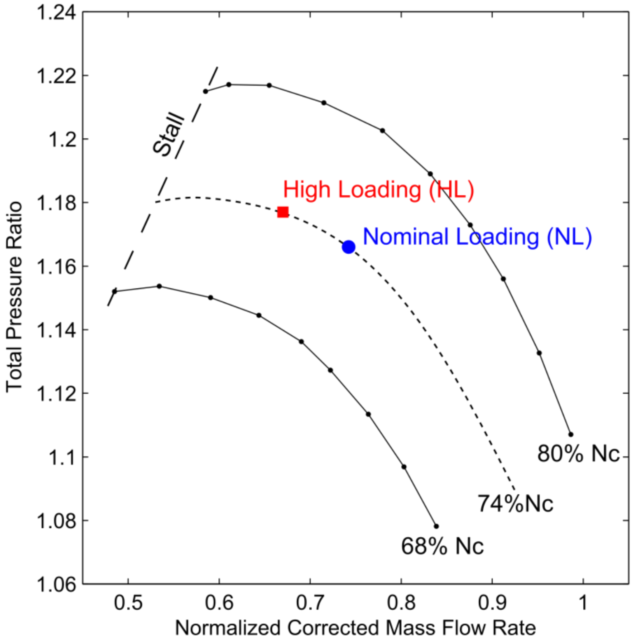

Figure 2.4 Part-speed operating points: Nominal Loading and High Loading

## 2.4 Steady Measurement Methodology

Several steady measurement techniques were used to characterize various aspects of steady compressor performance. These measurements include total pressures from rakes, static pressures at the casing endwall, absolute pressure, several total temperatures, and relative humidity. A couple of steady performance measurements which included specialty instrumentation design (pressures at the Stator 2 leading edge and under the stator hub shroud) will be discussed separately in Section 2.6.2.

Instrumentation ports positioned half way between every blade row allow for the acquisition of interstage data. Seven-element Kiel-head total pressure rakes were used at axial stations 1-8 (Figure 2.2). Static pressure taps in the casing endwall are also located at these positions. Additional total pressure and total temperature rakes are located at the compressor inlet, station 0, and the exhaust at station 9. The radial distributions of the rakes and area-weighting for each position are listed in Table 2.2. Many of the detailed traverses will focus on the embedded stage, and thus, data acquired at stations 4, 5, and 6, which are downstream of Stator 1, Rotor 2, and Stator 2, respectively, will be the focus for much of this study.

To capture small changes in the wakes associated with vane clocking, detailed circumferential traverses of the flow field will be performed with a resolution of 2%vp. Previous studies (Methel et al., 2015) have conducted stator wake variability data in the compressor which assisted in the selection of which circumferential positions to use. Slots in the casing and actuator arm length allow for over two vane passages to be traversed, and for position accounting the traverse range is from -50%vp to 150%vp. To acquire data from only one Stator 1 and Stator 2 vane without splitting the wakes at high loadings, the vane traverses when from 45% to 145%vp. On a given day, once the compressor reaches steady state for a particular loading condition, the throttle position is not changed until all six clocking configurations are measured. Due to the acquisition time required for measuring all six clocking configurations at one loading condition (approximately 10 hours), days of relatively constant ambient pressure are selected to avoid drift in the loading condition. The mechanical speed is adjusted during the run to maintain a corrected speed of 5000 rpm to within 0.1%.

Steady total pressure measurements from each rake port, as well as casing static pressure measurements, are acquired using Scanivalve Digital Sensor Arrays (DSA) which contain 16 temperature-compensated piezoresistive pressure sensors with ±0.05% full scale accuracy. Instrumentation in the second stage, third stage and the exhaust use a DSA 3217 with 5 psi pressure range, while the inlet, IGV, and first stage uses DSA 3016 units within a rack-mounted enclosure featuring smaller pressure ranges of 1 and 2.5 psi. Due to the smaller range, the 1 psi DSA has a full scale accuracy of 0.12%. The pressure transducers are zeroed every 20 minutes to minimize the effects of thermal drift. The ambient reference pressure was measured using a high accuracy barometric transducer with ±0.073% full scale accuracy. The resulting design point uncertainty for Stage 2 total pressure ratio is ±0.00027 and Stator 2 loss is ±0.007.

Temperature data were acquired using an Agilent Technologies 34980A Multifunction Switch/Measurement Unit with 34921A 40-Ch Multiplexer with low thermal offset and built-in reference temperature and a 34921T terminal block. Careful system setup and calibrations in an oil bath allow for uncertainty to less than 0.3°C for all channels (Berdanier, 2015). Relative humidity is measured with a digital hygrometer with an absolute uncertainty of ±2% relative humidity. To reduce sampling uncertainty with the hygrometer, the voltage signal is measured 40 times to ensure a large sample distribution.

Table 2.2 Rake element distributions and area weightings

| Radial Element | Inlet Pressure | | Exit Pressure | | Temperature & Interstage Pressure | |
|---|---|---|---|---|---|---|
| | %span | Area Weight | %span | Area Weight | %span | Area Weight |
| 1 | 12 | 6.5024 | 12 | 6.5024 | 12 | 6.5024 |
| 2 | 20 | 3.7476 | 20 | 4.8001 | 20 | 4.8001 |
| 3 | 30 | 4.24 | 35 | 6.42 | 35 | 6.42 |
| 4 | 40 | 6.51 | 50 | 6.6 | 50 | 7.7175 |
| 5 | 60 | 8.96 | 65 | 6.78 | 70 | 6.81 |
| 6 | 80 | 6.4624 | 80 | 5.3199 | 80 | 4.1724 |
| 7 | 88 | 7.5776 | 88 | 7.5776 | 88 | 7.5776 |

## 2.5 High Frequency Response Measurement Methodology

To capture unsteady effects caused by blade row interactions, including rotor wake passing and interaction with stator boundary layers, measurements which provide time-resolved data are required. For these investigations, two types of thermal anemometry and high frequency response pressure transducers were used and are described in more detail in the following sections.

While signal conditioning and calibration methods vary between the following measurement techniques, all signals were acquired using National Instruments (NI) PXIe-

1073 chassis with either a PXIe-6356 or PXIe-6358 card connected to a NI BNC 2110 connector block. Additionally all data were sampled simultaneously with a one-per-revolution trigger from an optical tachometer on the compressor drive shaft.

### 2.5.1 Time-Resolved Measurements of Stator Inlet Flow

To characterize the Stator 2 inlet flow field a high-frequency response pressure probe was used. Fast-response total pressure data were acquired with a Kulite LQ-062 sensor embedded in a miniature Kiel-head (0.083-in. diameter) probe. To evaluate pitchwise changes, 20 circumferential positions were traversed, with a detailed radial traverse that incorporated a higher resolution in the tip region: increments of 2% span from 78% to 100% span, increments of 4% span from 4% to 20% span and 70% to 78% span, and increments of 5% span from 20% to 70% span. These data were sampled at a rate of 300kHz for 500 rotor revolutions and filtered at 100kHz with Precision Filters Precision 28118 Octal Bridge Conditioner.

### 2.5.2 Surface Mounted Anemometry

To investigate the boundary layer development on each of the stators and investigate the effects of vane clocking on Stator 2 boundary layer response, surface-mounted hot-film anemometry was used. This section will discuss the basic methodology, array design, and data analysis.

#### 2.5.2.1 Methodology Background

Wall shear stress measurements acquired on the suction surface of all three stators will use surface-mounted hot-film anemometry, an established measurement technique to capture unsteady boundary layer development in turbomachinery. The method, originally developed by Bellhouse and Schultz (1966), relates the heat transfer of the sensor with the wall shear stress by:

$$\tau_w = k\left(\frac{E^2 - A^2}{\Delta T}\right)^3, \tag{2.2}$$

where $k$ and $A$ are calibration constants, $E$ is the instantaneous anemometer voltage, and $\Delta T$ is the temperature difference between the heated sensor and the air. For the current application, calibration of each sensor is not possible because the one-time-use array is adhered directly to the vane. Using the relation described by Hodson et al. (1994), the uncalibrated sensors can still provide semi-qualitative information about the instantaneous state of the boundary layer. This method approximates the heat loss from the substrate (the $A^2$ term) to the square of the zero-flow anemometer voltage ($E_o$) and assumes the air temperature will be equal to that of the vane surface. Thus, $\Delta T$ is proportional to ${E_o}^2$. This voltage is acquired both immediately before and immediately after a test. Therefore, wall shear stress can be approximated by the relation:

$$\tau_w \sim \text{QWSS} = \left(\frac{E^2 - E_o^2}{E_o^2}\right)^3 . \tag{2.3}$$

This quantity is typically referred to as quasi-wall shear stress (QWSS) and will be used to evaluate unsteady boundary layer transition in this research. This method also minimizes effects of sensor-to-sensor variation, allowing for better comparison across an array of sensors. Calibration would be not only cumbersome, but it would also be required for both laminar and turbulent flow regimes.

### 2.5.2.2 Sensor Array Design and Implementation

Boundary layer transition on the vane will be affected by many flow features and geometry parameters, including the inlet Reynolds number, turbulence intensity, surface roughness, overall pressure gradient, leading edge shape, and pressure gradient set up by the curvature of the vane. Many of these flow characteristics change with each stage of a compressor, and thus, acquiring wall-shear stress data on all three stators will provide insight to how the boundary layer transition differs from vane to vane through a compressor.

While the boundary layer development of all three stators will be investigated, the hot-film array design is based on Stator 2 properties, due to the emphasis on the vane clocking portion of this work. The Stator 2 surface pressure and isentropic Mach number distributions taken from a CFD solution as well as preliminary wall-shear stress data show the suction surface flow accelerates around the leading edge up to the position of 20% axial chord ($c_{ax}$). At this position, the peak velocity occurs followed by a nearly constant diffusion rate to the trailing edge. No hot-film sensors will be placed on the pressure side of the airfoil, but the computational results show that the flow decelerates on the pressure surface until around 75% axial chord, after which there is a slight acceleration toward the trailing edge.

Based on the vane pressure distribution and a previous test with a coarse ten-sensor array, the hot-film array has eighteen sensors positioned in the chordwise direction at 4, 8, 12, 16, 20, 24, 28, 32, 36, 40, 44, 48, 52, 56, 60, 70, 80, and 90% Stator 2 suction side length (s), shown in Figure 2.5 . Researchers studying compressor boundary layers with hot-film sensors have used as few as 4 sensors placed every 25%c (Hansen and

Okiishi, 1989) and as many as 30 sensors placed every 3%c (Halstead et al., 1997, Soloman and Walker, 1995). The suction side is the focus of this study because of its larger peak velocity and thus, larger amount of diffusion, rendering this surface more susceptible to boundary layer transition. Furthermore, previous studies have shown vane clocking either has no effect on the pressure side or small effects at low loading conditions which experience negative incidence.

The film substrate, to which the array is mounted, has extra chordwise length near the leading edge so that it can be wrapped around the leading edge terminating on the vane pressure side to avoid tripping the boundary layer on the suction surface. Although the applied film adds approximately 0.006 inches to the vane leading edge thickness and provides a smoother vane surface, vane wake measurements show that it has little effect on the vane's profile loss (Smith, 2011).

A Dantec constant temperature anemometer was used to acquire the surface-mounted hot-film sensor signals. The frequency response of the mounted sensors in the flow conditions evaluated with a square-wave test was 30 kHz, which is comparable to previous tests with similar sensors. The blade pass frequency of Rotor 1 is 3.0 kHz, of Rotor 2 is 2.75 kHz, and of Rotor 3 is 2.5 kHz, and thus, several harmonics of the blade pass frequencies were captured.

Although small, the temperature gradients in both the flow field and hardware of this compressor are measurable and could affect the hot-film measurements. A study (Smith, 2011) using several overheat ratios was conducted to assess the thermal sensitivity. From these data, overheat ratios of 1.2 or more provided similar results.

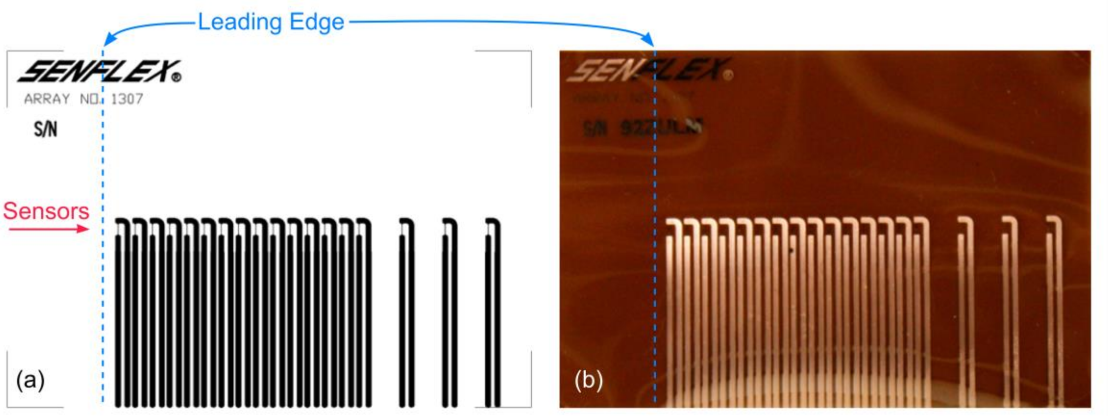

Figure 2.5 Hot-film sensor array, (a) drawing (b) photo

#### 2.5.2.3 Quasi-Wall Shear Stress Analysis

Using a once-per-revolution trigger, the unsteady QWSS data are ensemble averaged using:

$$\langle \mathrm{QWSS}(t)\rangle = \frac{1}{\mathrm{N}}\sum_{\mathrm{i}=0}^{\mathrm{N}-1} \mathrm{QWSS}_{\mathrm{i}}(t)\ , \tag{2.4}$$

where N is the number of ensembles (500 rotor revolutions for the surface-mounted films). Next, the data will be broken into random and periodic fluctuations. The stochastic fluctuations are described by the ensemble averaged root mean square value (RMS), given by:

$$\langle \mathrm{RMS}(\mathrm{QWSS(t)})\rangle = \sqrt{\frac{1}{\mathrm{N}}\sum_{\mathrm{i}=0}^{\mathrm{N}-1}\left(\mathrm{QWSS}_{\mathrm{i}}(\mathrm{t}) - \langle \mathrm{QWSS(t)}\rangle\right)^2}\ . \tag{2.5}$$

The final statistical quantity used to evaluate the boundary layer development is the skewness. As the third-order moment, skew is a measure of the distribution’s symmetry about the mean value:

$$\langle \mathrm{Skew}(\mathrm{QWSS}(t))\rangle = \frac{1}{\mathrm{N}}\sum_{\mathrm{i}=0}^{\mathrm{N}-1}\left(\mathrm{QWSS}_{\mathrm{i}}(t) - \langle \mathrm{QWSS}(t)\rangle\right)^3\ . \tag{2.6}$$

The skew of a signal indicates how the signal has deviated (in a positive or negative manner) from the mean of the signal. The skew of the surface-mounted hot-film measurements can be used to determine the state of the boundary layer through the transition process. A laminar boundary layer will have a skew near zero. If the boundary layer is mostly laminar with only occasional turbulent fluctuations, then the skew will be positive but small. When the boundary layer becomes more turbulent, with only a small laminar component, the skew becomes negative. When the boundary layer becomes completely turbulent, it has a skew of zero. Skew is normalized by the maximum time-averaged skew for the entire ensemble averaged revolution. Thus, using QWSS, RMS, and skew altogether, unsteady vane boundary layer transition can be understood.

## 2.6 Stator 2 Insert for Special Instrumentation

To implement specialty instrumentation within the Stator 2 passage, new hardware was manufactured – one new Stator 2 half ring. This ring was then electrical discharge machined (EDM) into 3 sections. Additional modifications were made to the casing to allow for extra tie rods to secure the sections and through holes for wire routing. The smallest section contains two vane passages. The research used a version of this insert section with flush mounted high- frequency response pressure

To acquire unsteady surface pressures, high-frequency response pressure transducers were embedded into the two vanes of a Stator 2 insert. Each vane was instrumented with 8 Kulite LQ-062 pressure transducers. The sensors were positioned at 50% and 80% span, at 10%, 20%, 30%, and 40% chord on the pressure side of one blade and the suction side of another, such that they measure the same vane passage. The transducers did not have screens which resulted in a higher frequency response, as much as 100-150 kHz per manufacturer’s specifications. Details regarding the pressure calibration can be found in Murray (2014).

These data were acquired at several loading conditions (L1-L7), but unfortunately the dynamic range of pressures anticipated at L8 and L9 was too high for the pressure transducers. Six clocking configurations were included. These data were sampled at 300kHz for over 500 rotor revolutions.

## 2.7 Flow Visualization

Flow visualization was performed using a mixture of kerosene and powder paint. The mixture is inserted upstream of the compressor while it is operated at a steady operating condition. The mixture flows through the compressor, and eventually the kerosene evaporates leaving streaklines of paint on the flowpath surfaces, particularly in regions of flow recirculation. This section outlines the details of the mixture, injection implementation, and image capturing.

The paints utilized for this work were powder paints that can be found in a typical craft store. Best results were obtained with paints that fluoresce, though their specification labels did not indicate this capability. The two brands used in this research are Rich Art Fresco Powder Tempera Turquoise and Sargent Art Gothic Powder Paints Orange. It should also be noted that other colors from the same brands did not fluoresce except for Rich Art Fresco Powder Tempera Magenta. To determine if a paint would be suitable for compressor flow visualization, a sample was mixed with kerosene and tested on a flat plate (with similar surface finish as the compressor stators) using an air jet. Approximately, ten different paints and colors were tested in a variety of mixture ratios.

Some paints do not dissolve well with Kerosene and some were grainy. The various colors of paint also result in an array of contrast quality against the metal surface. From these observations, paint choices were down selected. The mixture ratio is key to providing a thin layer of paint on the vanes. To increase coverage, a larger volume of paint can be introduced to the compressor. Best results occurred with a 2.5:1 kerosene-to-paint mixture ratio. A higher mixture ratio results in thinner coverage of paint, often failing to provide good contrast or definition for imaging, while a lower ratio tends to coat the blading too heavily inhibiting the definition of streaklines on the surface due to in adequate flow of the paint.

The total volume of paint injected into the machine must also be considered. Similar to the effects of mixture ratio, too much overall volume will completely coat the blading, removing the definition of surface flow patterns. For the data presented here, approximately 150mL were used for each test. This amount was determined based on preliminary tests and will likely vary based on the mass flow rate and number of stages in the machine.

The general procedure used for these flow visualization tests included the following steps. Kerosene and paint were mixed and put into a wash bottle. The test setup is shown in Figure 2.6, forward-looking-aft at the compressor inlet. A 6.53-mm diameter capped probe with a 3.175-mm diameter hole parallel to the flow direction, shown in the detail of Figure 2.6, was used to inject the mixture at the AIP. Smaller probes had clogging issues. For this compressor, paint injection at the AIP is sufficient for flow visualization on all stages. This is beneficial to the simplicity of the technique because it does not require multiple probes and allows the injection to be naturally pressure driven since the AIP pressure is less than atmospheric pressure due to losses in the inlet system. By injecting the paint at 20% span, full coverage on the stators from the hub to the tip is obtained since paint is flung radially outward toward the casing when passing through each rotor. This injection method does rely on the rotor to radially disperse the paint, and thus, it does not provide flow visualization of the IGV. For safety purposes, no one is allowed in the test cell during compressor operation, and thus, the paint must be plumbed from the control room to the compressor injection port. A flexible vinyl tube is connected to the end of the probe and routed to the control room. The tubing is secured to the ceiling, so that gravity aids the pressure-driven paint flow, while maintaining a healthy bend radius, to avoid clogging issues at the entrance of the probe. Circumferential positions are labeled A, B, and C in Figure 2.6; these positions are chosen based on the circumferential traversing ability at the AIP, positions of the struts, and locations of the other instrumentation.

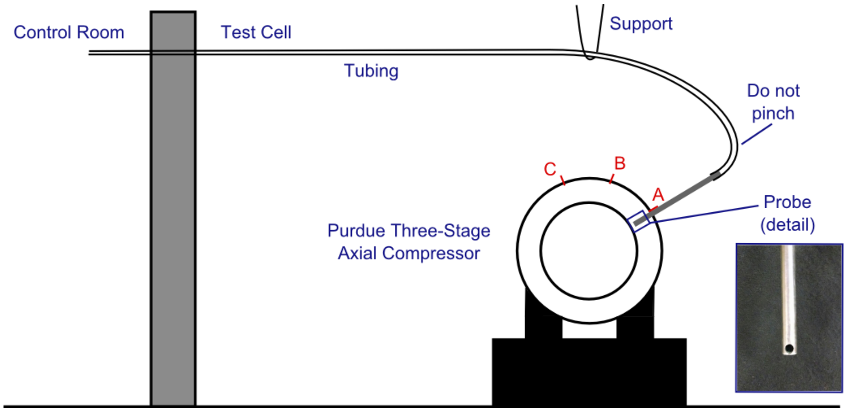

Figure 2.6 Schematic of flow visualization setup

Once the compressor operating point is set, paint is injected at the first circumferential position. Visual confirmation (via cameras or a window into the test cell) is useful to identify possible clogging issues. After the mixture is injected, the operating condition was held constant for about 10 minutes to ensure that the kerosene had evaporated, the paint was dry, and a change in the flow field would not affect the streaklines. Multiple colors of paints and multiple circumferential locations provide an opportunity to obtain multiple loading conditions in a single test.

Since the rig must be disassembled and cleaned after each test, it is tempting to pack as many tests in as possible before disassembly. However, the cleanest datasets have been achieved from tests where only a single operating condition with a single color of paint was used. Most of the images presented were collected with this method. All three circumferential positions at the AIP are used with the same paint and loading condition, but at each location a different volume of paint is injected with the hopes of providing the right amount of coverage to a particular vane row. For example, to ensure Stator 3 receives enough coverage, more paint is injected at location C, knowing that this sector will have too much coverage for Stators 1 and Stators 2. However, less mixture will be injected at locations A and B to provide the ideal coverage for those vanes rows (while providing insufficient coverage to Stator 3).

Flow visualization in this facility is relatively quick, simple, and inexpensive but acquiring the images can be labor intensive. Approximately six hours is needed for two people to disassemble and prepare the vanes to be photographed. All images in this paper were taken with a Canon Rebel XSi DSLR camera with an EF-S 18-55mm f/3.5-5.6 SI lens. The compressor has monolithic shrouded vanes, which present some difficulty in finding a good angle to view as much of the suction side of the vane as possible. Since the paint is deposited in regions of recirculating flow, most of paint is near the trailing edge. Thus, all pictures are taken aft of the vane, looking forward. Each image was setup to see the maximum amount of the vane suction side without the trailing edge of the adjacent vane overlapping the leading edge of the imaged (in-focus) vane. The lens was positioned perpendicularly with the imaged vane, and thus, the pictures are taken square to the suction side of the vane. This positioning is repeated for each vane. It is useful to have a system to rotate the stator ring one vane passage at a time to allow the position of the camera and tripod to remain unchanged and improve consistency of image angle for all vanes. Ideally, fiducial markers could be permanently applied to each vane in the same orientation and used as references while taking and post processing images. For this study, the trailing edge and fillets of each vane are used as pseudo-fiducials when comparing vane-to-vane variations.

Testing various lighting situations can benefit the resulting photo quality. The images presented in this paper used light from overhead fluorescent light bulbs and a lamp with a CFL bulb. Often the overhead light was blocked from the leading edge of the vanes to reduce glare and reflection on the metal surfaces. A lightbox might be useful. The ultraviolet light used was a 100 Watt ultra violet black light lamp. When using these lamps, the angle of the incoming light should be as square with the vane passage as possible to prevent the formation of shadows in the corners.

Figure 2.7 shows an example of three general lighting conditions with the fluorescent paint: visible, mixed visible and ultraviolet, and ultraviolet from left to right. The blue color does not stand out particularly well under plain visible light on the metal stator surface in Figure 2.7a, but under the UV light in Figure 2.7c, the streaklines are clear with high contrast, especially within the recirculating region. The middle image with mixed lighting can be useful to make the paint standout without losing the surrounding geometry. Three images like these are acquired for each vane, ideally while maintaining the camera position and changing only the lighting (and camera settings) between the pictures. One benefit to reproducing the same camera angles and lighting for each vane is that camera settings should remain relatively constant for the three light conditions. For most images in these tests, the focal distance remained about the same, 35 to 49mm, shutter speeds varied from 1/8 to 1/2sec, and aperture setting from f/4.5 to f/7.1. No flash was used as partial metering kept the streaklines in the separated regions in focus, and an ISO of 200 was set to maintain quality in low light setting, avoiding grainy images.

Once complete, thorough cleaning of the vanes is important. If the paint is not adequately removed, even trace amounts of residual paint will appear in the UV pictures during the next flow visualization test.

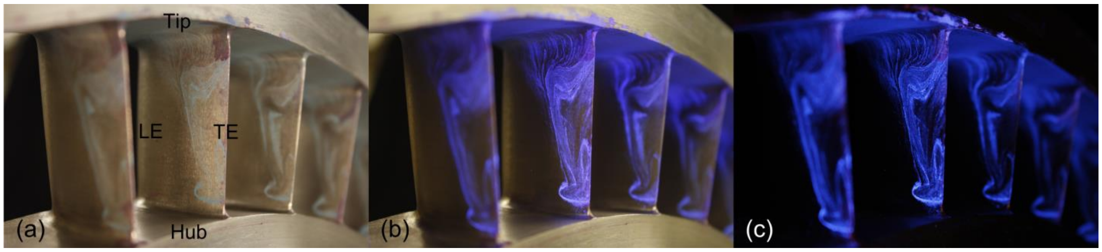

Figure 2.7 Lighting comparison with (a) visible, (b) mixed, and (c) UV

# CHAPTER 3. ASPECTS OF COMPRESSOR CORRECTED CONDITIONS AND PERFORMANCE REPEATABILITY

When measuring small changes in steady compressor performance, it is important to ensure reliable, repeatable day-to-day performance, especially in a facility that draws in atmospheric air like the Purdue Three Stage Compressor. Temperature, pressure, and relative humidity, all have effects on the working fluid's properties. Neglecting these effects can result in non-repeatable performance. This chapter will discuss the role of humidity and real gas properties for correcting rotational speed and mass flow rate, correcting performance to represent standard day density rise and work coefficient, and Reynolds number and inlet temperature effects on steady compressor performance. Addressing proper accounting for ambient conditions will provide confidence in the interpretation of small changes in performance presented later in this study. These results will focus on the effects on overall compressor performance (total pressure ratio), but will call upon some interstage data to support the conclusions drawn herein. These experiments utilize seven-element total pressure rakes for total pressure and static pressure taps at the compressor inlet and exhaust and between every blade row, as noted in Figure 3.1.

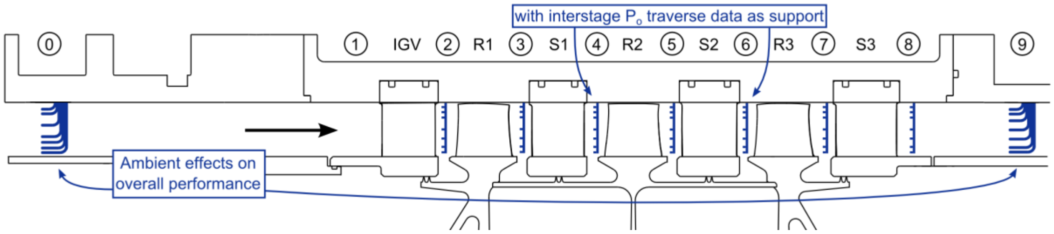

Figure 3.1 Summary of steady performance data collection

## 3.1 Humidity Accounting

The basic formulations for correcting rotational speed and mass flow rate to standard day conditions, which are presented in textbooks and the classroom, do not account for any water content in the air. The presence of water changes the properties of the working fluid, and thus, broadens the variables to be considered. Similarity analyses are used to equate test conditions to standard day reference conditions. This section will present derivations for corrected rotational speed and corrected mass flow rate which includes relative humidity and real gas effects.

### 3.1.1 Corrected Rotational Speed

The corrected speed is derived by maintaining a constant blade tip Mach number (as defined by Dixon, 2005), where the velocity is represented by the product of diameter, *D*, and rotational speed, *N*, and normalized by the speed of sound at stagnation conditions, $a_o$:

$$\Pi_N = \frac{DN}{a_o} \equiv \Pi_{N,real}\ . \tag{3.1}$$

Equation (3.1) is also analogous to the first dynamic scaling step applied by Cumpsty (2004), for which a speed of sound based on stagnation temperature is used instead of static temperature because stagnation temperature is available with typical instrumentation. This initial definition of the Pi parameter defined in Eq. (3.1) is the non-dimensional speed parameter for a real gas, $\Pi_{N,real}$. Turbomachinery textbooks (Dixon, 2005; Cumpsty, 2004; Lakshminarayana, 1996; Walsh and Fletcher, 2004; Wright, 1999; Balje, 1981; Saravunamuttoo et al., 2009) typically apply the assumption of a thermally-perfect gas to simplify Eq. (1) using the definition of the speed of sound at stagnation conditions:

$$a_o = \sqrt{\gamma R T_o}\,, \tag{3.2}$$

which yields the following definition for an ideal gas:

$$\Pi_N = \frac{DN}{\sqrt{\gamma R T_o}} \equiv \Pi_{N,ideal}\,, \tag{3.3}$$

where $\Pi_{N,ideal}$ is the Pi group for an ideal gas speed parameter, $\gamma$ is the ratio of specific heats, $R$ is the specific gas constant, and $T_o$ is stagnation temperature. Equations (3.1) and (3.3) provide the Pi groups from which the corrected speed formulae may be derived.

In each case, Eqs. (3.1) and (3.3) can be independently equated for two conditions (enforcing similarity between the conditions) which will be named “reference” and “actual.” To abide by typical turbomachinery language, the actual speed will be denoted by the mechanical speed, $N_{mech}$. These two conditions apply to the same physical machine, where there is no change in the diameter, $D$. Using Eq. (3.1) for a real gas, this relation simplifies to

$$N_{ref,real} = \frac{N_{mech}}{a_{o,act}/a_{o,ref}} \equiv N_c^*\,. \tag{3.4}$$

The reference condition rotational speed in Eq. (3.4) represents the corrected speed with the inclusion of humidity effects, which will be denoted by $N_c^*$. Humidity present in test conditions is thus accounted for when calculating the stagnation speed of sound for the actual (or test) conditions. For a thermally-perfect (ideal) gas, the speed of sound presented in Eq. (3.2) is applicable. Under the additional assumption of a calorically-perfect gas, the product of $\gamma$ and $R$ is constant for a particular gas mixture. This simplification yields

$$N_{ref,P} = \frac{N_{mech}}{\sqrt{T_{o,act}/T_{o,ref}}} \equiv N_c \,. \tag{3.5}$$

Eq. (3.5) is the well-known "classical" representation of corrected rotational speed for a dry air formulation, $N_c$, which is found in most turbomachinery texts, and it is derived using a perfect gas assumption.

### 3.1.2 Corrected Mass Flow Rate

Through a method similar to the one outlined for corrected rotational speed, two equations can be derived, via similarity analysis, to represent the corrected mass flow rate for both a real gas and a perfect gas. Mass flow rate can be non-dimensionalized with a velocity, $v$ (the product of diameter and rotational speed), an area which is proportional to the machine diameter squared, and a stagnation density, $\rho_o$:

$$\frac{\dot{m}}{\rho v A} \propto \frac{\dot{m}}{\rho_o (DN) D^2} = \Pi_{\dot{m}} \,. \tag{3.6}$$

Through the Buckingham Pi Theorem (1914) additional non-dimensional Pi terms can be created by multiplying existing Pi terms. The product of Eqs. (3.1) and (3.6) creates

$$\Pi_N \Pi_{\dot{m}} = \frac{\dot{m}}{\rho_o a_o D^2} \equiv \Pi_{\dot{m},real}\ , \tag{3.7}$$

which is the non-dimensional Pi parameter for mass flow rate for a real gas, $\Pi_{\dot{m},real}$. Assuming a thermally-perfect (ideal) gas and using Eq. (3.2), the Pi parameter for mass flow rate becomes:

$$\Pi_N \Pi_{\dot{m}} = \frac{\dot{m}\sqrt{RT_o}}{P_o D^2 \sqrt{\gamma}} \equiv \Pi_{\dot{m},ideal}\ , \tag{3.8}$$

where $\Pi_{\dot{m},ideal}$ is the non-dimensional Pi group for mass flow rate with the ideal gas assumption.

Similar to the procedure for corrected speed, Eqs. (3.7) and (3.8) can be independently equated between “reference” and “actual” conditions to achieve similarity. For this derivation, there is no change in diameter for the same physical machine. Therefore, Eq. (7) reduces to

$$\dot{m}_{ref,real} = \dot{m}_{act} \left( \frac{\rho_{o,ref} a_{o,ref}}{\rho_{o,act} a_{o,act}} \right) \equiv \dot{m}_c^*\ , \tag{3.9}$$

which represents the corrected mass flow rate incorporating humidity effects, $\dot{m}_c^*$. When the perfect gas assumption is used, $\gamma$ and $R$ are constant, and Eq. (3.8) reduces to

$$\dot{m}_{ref,perfect} = \dot{m}_{act} \frac{P_{o,ref}}{P_{o,act}} \sqrt{\frac{T_{o,act}}{T_{o,ref}}} \equiv \dot{m}_c\ , \tag{3.10}$$

which is recognizable as the “classical” corrected mass flow rate for a dry air formulation, $\dot{m}_c$.

Equations (3.4) and (3.5), with (3.9) and (3.10), make up the corrected conditions for rotational speed and mass flow rate, respectively. For these equations, the following definitions apply because the reference condition exists as a dry air composition:

$$
\begin{gathered}
a_{o,ref} = \sqrt{\gamma_{ref} R_{ref} T_{o,ref}} \\
\rho_{o,ref} = \frac{P_{o,ref}}{R_{ref} T_{o,ref}} \\
P_{o,ref} = 1\ \text{atm} = 14.7\ \text{psi} \\
T_{o,ref} = 518.67\ {}^{\text{o}}\text{R} = 288.15\text{K} \\
\gamma_{ref} = 1.4 \\
R_{ref} = 53.351 \frac{\text{ft lb}_{\text{f}}}{\text{lb}_{\text{m}}\ {}^{\text{o}}\text{R}} = 287.058 \frac{\text{J}}{\text{kg K}}\ .
\end{gathered}
\tag{3.11}
$$

The importance of the significant figures used to define the reference conditions in Eq. (3.11) should also be considered. While the actual values for a dry composition of air as a perfect gas may have more significant figures, to maintain consistent comparison with computations, the number of significant digits used in the reference conditions in Eq. (3.11) should match those used in numerical computations. Misrepresenting these values or any required unit conversion factors could affect the calculated corrected conditions.

### 3.1.3 Effects of Humidity on Corrected Conditions

To maintain a desired corrected rotational speed, a test operator may apply Eqs. (3.4) or (3.5) for $N_c^*$ or $N_c$, respectively, and determine the required mechanical speed for the machine, $N_{mech,Eq.(3.4)}$ or $N_{mech,Eq.(3.5)}$. By comparing these two corrected speed formulations, the relative effect of humidity on the mechanical speed is determined. Figure 3.2(a) shows the difference between mechanical speeds calculated from Eqs. (3.4) and (3.5) as a percent difference,

$$
\frac{\left(N_{mech,Eq.(3.4)} - N_{mech,Eq.(3.5)}\right)}{N_{mech,Eq.(3.4)}}\ 100\%, \tag{3.12}
$$

over a range of inlet total temperature and relative humidity for the same corrected speed.

The calculation presented in Eq. (3.12) is also affected by the inlet total pressure for the speed correction from Eq. (3.4), where pressure is used to calculate the stagnation speed of sound and the absolute humidity. However, the difference in mechanical speeds (Eq. 3.12) is a weak function of pressure when compared to the contribution of temperature and relative humidity. As a result, an average pressure of 14.3 psi (98.6 kPa) is used for this calculation. A ±0.4 psi (2.8 kPa) change in total pressure would shift the contours in Fig. 1(a) by the amount shown by the bars on the 0.1% and 0.8% contours (a day-to-day ambient pressure variation of ±0.2 psi from average is typical at Purdue University). Figure 3.2(a) also shows the measured weather conditions at the Purdue Compressor Research Laboratory in West Lafayette, Indiana for representative points in 2013 during which experimental data were collected with the Purdue Three-Stage Compressor. Of these data, the triangular symbols denote the test conditions that result in the largest effect of compressor operational speed. This figure shows that differences in excess of 0.5% of the proper mechanical speed exist under these hot and humid weather conditions.

The implications of this potential difference are dependent on the facility in question. For example, a low-speed compressor facility that operates at a design speed of 500 rpm may find a performance difference due to a 0.5% speed discrepancy within the uncertainty of the measurements. However, for an intermediate-speed axial compressor that operates at 5,000 rpm or a high-speed centrifugal compressor that operates at 50,000 rpm, such as the compressors at Purdue University, may experience a measurable performance change for a 0.5% change in rotational speed.

It is important for this discussion that the rotational speed of the compressor is precisely maintained, or else shifts due to incorporating humidity in correction methods are inconsequential. The drive system that controls shaft speed at the Purdue Compressor Research Laboratory is capable of maintaining an operating speed within 0.01% of the desired set point. As a result, shifts of rotational speed by over 0.5% can be easily detected during operation.

Figure 3.2(b) shows the differences between actual mass flow rates calculated from Eqs. (3.9) and (3.10) as a percent difference for the same corrected mass flow rate,

$$\frac{\left(\dot{m}_{act,Eq.(9)}-\dot{m}_{act,Eq.(10)}\right)}{\dot{m}_{act,Eq.(9)}}\ 100\%. \tag{3.13}$$

These data show differences of up to 1% are present when certain weather conditions exist (hot and humid). It should be noted, for research compressors which utilize a low flow rate, the relative effect of 1% may not be distinguishable within the propagation of measurement uncertainty for the calculated corrected flow rate. Nonetheless, it is important to realize the potential effect.

The corrected mass flow rate is a calculated parameter which could be re-calculated in post-processing to include humidity. The corrected speed, on the other hand, must be accounted for real-time during the experiment if a particular speedline is desired. If a particular speedline is not desired, there is still an additional risk that the data may represent a scatter of results over several corrected speeds. This could be problematic for a test campaign acquiring detailed data over the course of multiple days, weeks, or months for which flow physics trends need to be compared at particular speeds. Furthermore, for these extended campaigns, if there is a need to return to a particular operating condition (corrected mass flow rate) on a day with significantly different ambient weather conditions, there is an additional emphasis on also implementing accurate real-time mass flow rate corrections. This ensures the same operating point will be investigated on each test day.

The possible range of humidity effects on corrected conditions and calculated parameters using the equations laid out here have been reported by Berdanier et al. (2015). Figure 3.3 shows these results of how humidity could affect the speedline performance by the yellow-shaded region where the “Reference” line is a compressor performance at 100% corrected speed at reference conditions. To emphasize the importance of accounting for humidity effects, Figure 3.3 shows a series of important research topics relative to these humidity-based performance changes. Specifically, a rotor tip clearance study (Berdanier and Key, 2015a) was performed in the Purdue three-stage compressor facility for tip clearance heights of 1.5% (the Reference line) and 3.0% span. The effect of doubling the rotor tip clearance is on the same order as the effect of humidity since the results fall mostly within the shaded area.

Also in Figure 3.3, the effects of vane clocking on steady compressor performance in the Purdue three-stage compressor facility, which will be discussed in the following chapter, are shown. These results are indicated by bars showing vane clocking effects on total pressure ratio. It is widely known that vane clocking has a small but measureable effect on performance. However, proper humidity accounting must be considered during such experiments since the change in total pressure ratio due to vane clocking falls within the range of performance that would result if humid air properties are not used when calculating corrected parameters.

Finally, a survey of literature yields results from other important compressor research topics including rotor eccentricity (Graf et al., 1998), surface roughness (Bons, 2010), under-stator-platform knife-seal clearance (Wellborn and Okiishi, 1999), and inlet distortion (Hynes and Greitzer, 1987). To assess the effect of humidity relative to these research areas, the published results from these external projects have been applied as representative shifts to the "Reference" speedline. Ultimately, if humidity is not taken into account when setting corrected performance parameters, the difference in measured performance will be on the same order of the major research topics shown in Figure 3.3. Therefore, it would be difficult or nearly impossible to interpret the results for these types of experiments.

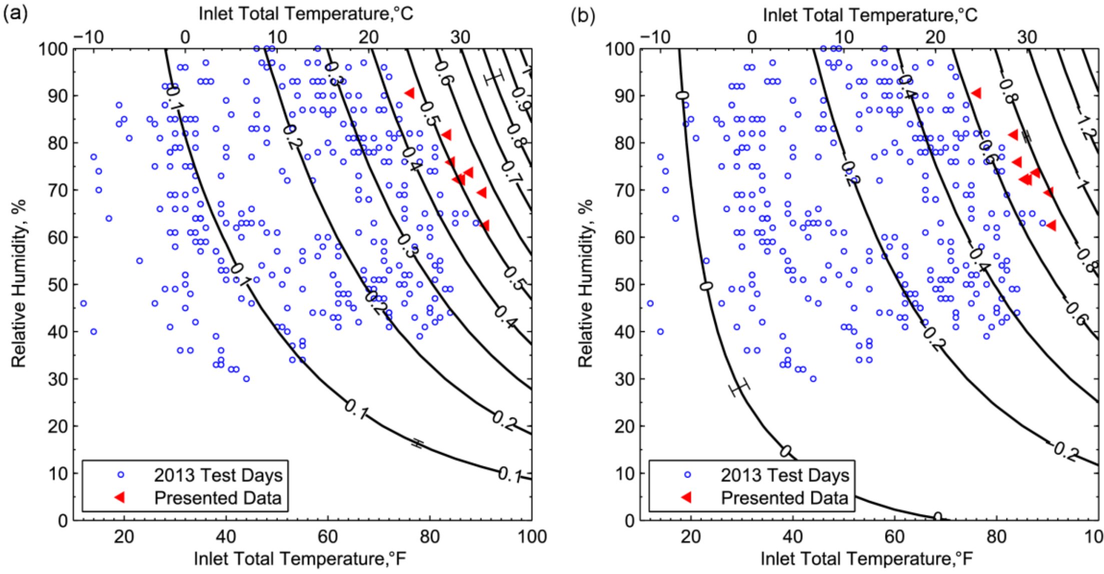

Figure 3.2 Effect of humidity on (a) calculated mechanical speed and (b) actual mass flow rate as lines of constant percent difference

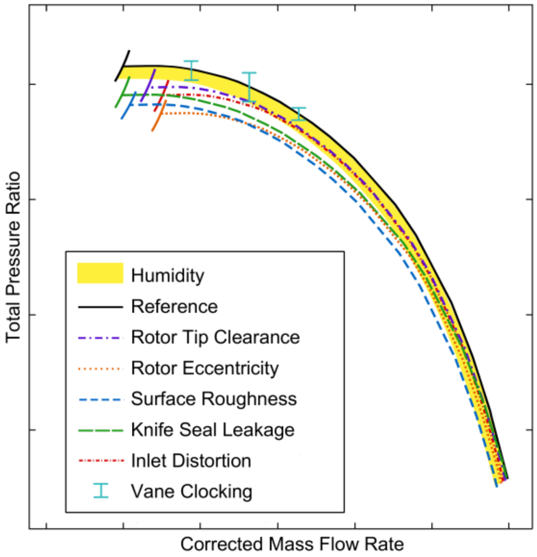

Figure 3.3 Approximate effects of major research areas on compressor performance compared to humidity effects (Graf et al., 1998; Bons, 2010; Wellborn and Okiishi, 1999; Hynes and Greitzer, 1987)

## 3.2 Correcting Performance for Density and Work

After incorporating humidity and real gas effects into corrected inlet conditions for rotational speed and mass flow rate, there remain measurable and repeatable discrepancies between compressor performance on a cold and hot day. This is shown in Figure 3.4 for compressor overall total pressure ratio for the 3% and 4% tip clearance configurations. Corrected mass flow rate has been normalized by a nominal loading condition half way up the speedline. These data represent the average of a 20-point circumferential traverse and are repeatable for the similar inlet conditions. Data from two rotor tip clearance heights are presented to show that the trends persist in multiple hardware configurations. While data will be shown at the 1.5% tip clearance later in the discussion, traversed speedlines at both inlet temperatures were not available at the smallest tip clearance, and thus, it is not included in Figure 3.4. This discussion focuses on the differences in total pressure ratio. The throttle setting was not controlled to ensure that the corrected mass flow rates between the hot and cold days matched, and thus, there is no conclusion to be drawn in the different mass flow rates (the horizontal offset) for the different temperatures presented in Figure 3.4.

The discrepancy between hot and cold day total pressure ratio (TPR) is most significant at high loading conditions. The maximum difference occurs at the near stall operating condition, the lowest mass flow rate. At the near stall condition, the TPR difference is 0.0056 (0.417%) for the 3% tip clearance and 0.0015 (0.113%) for the 4% tip clearance. With a measurement uncertainty on the order of the differences shown for the 4% clearance configuration, the discrepancy at the 3% clearance configuration is about four times larger than the measurement uncertainty, and it motivates the need to understand the differences in performance between a hot day and a cold day.

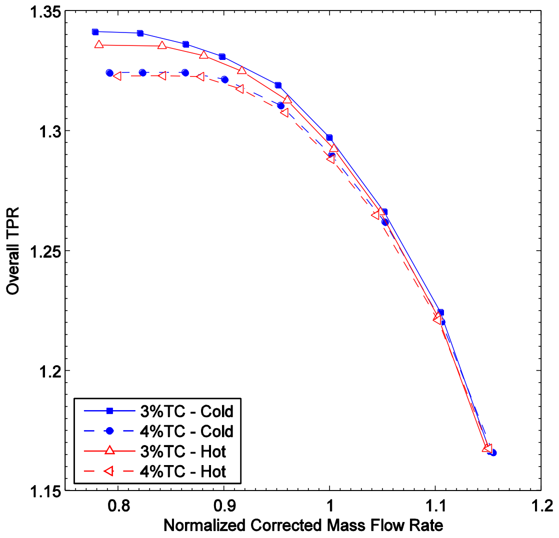

Figure 3.4 TPR discrepancy between a hot day and a cold day and 3% and 4% rotor tip clearance

### 3.2.1 Density Ratio and Work Coefficient Correction Procedure

Compressor research facilities which use unconditioned atmospheric air are subject to the changes in fluid properties of air with ambient conditions: temperature, pressure, and humidity. The variations of these atmospheric conditions make it likely that the compressor will not achieve the same pressure (or density) rise as it would with the reference conditions (Eq. 3.11), because it will begin at a different initial state on the Mollier Enthalpy-Entropy diagram. Thus, varying ambient conditions change the compression process including enthalpy rise (work input) and entropy rise (losses).

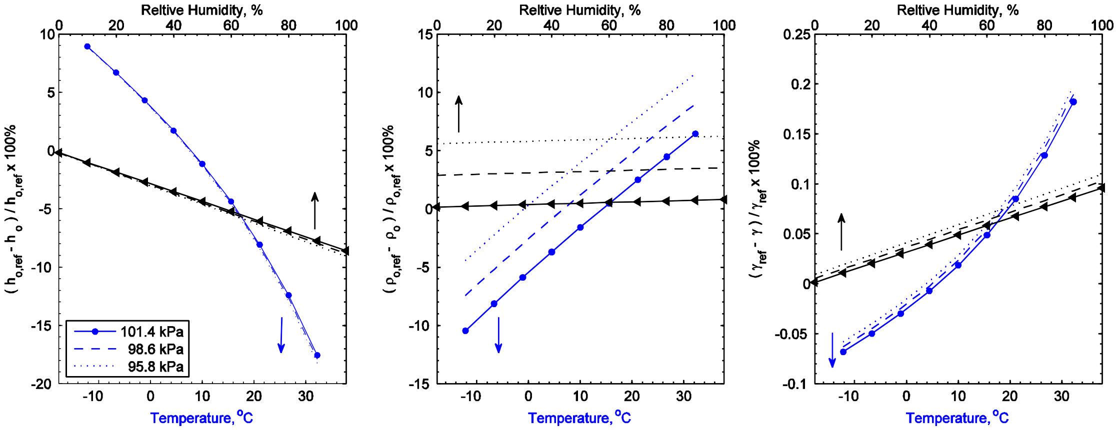

Figure 3.5 Effects ambient pressure, temperature and relative humidity changes from reference conditions on the enthalpy, density and ratio of specific heats of air in terms of percent difference.

Figure 3.5 shows the percent difference in total enthalpy, $h_o$, total density, $\rho_o$, and ratio of specific heats, $\gamma$, compared to air at reference conditions for a variety of inlet pressures, temperatures, and relative humidity values that could occur throughout a typical year in the Midwest United States. The effects of temperature alone were calculated over a range of -12 to 32°C (10 to 90°F) while holding relative humidity (RH) constant at the reference condition (0%RH); this is shown in blue along the bottom axis in Figure 3.5. Similarly, the effects of relative humidity were considered over a range from 0 to 100%RH while holding temperature constant at reference conditions (15 ºC), and this is shown in black along the upper axis in Figure 3.5. Each of these trends is shown for three pressures: 95.8, 98.6, and 101.4 kPa (13.9, 14.3, and 14.7 psi). Temperature is the strongest driver of changes in these fluid properties. At 32.2 ºC (90ºF), dry air has an enthalpy which is over 20% larger than that for standard day conditions. Furthermore, high humidity at reference temperature can increase total enthalpy by 8% over dry air, while pressure has only a small effect.  Density is a weak function of relative humidity, but a 2.8 kPa (0.4 psi) change in pressure changes the air density by nearly 3% from reference conditions. These same changes in ambient conditions affect the ratio of specific heats by less than 0.5%.

To correct compressor performance for these ambient condition fluctuations, density ratio and work coefficient will be held constant between the true test conditions and the ideal reference conditions, similar to the procedure outlined in the ASME PTC for compressors and exhauster [6].

First, the density ratios are equated between the test and reference conditions:

$$\left(\frac{\rho_{o,e}}{\rho_{o,i}}\right)_{ref} = \left(\frac{\rho_{o,e}}{\rho_{o,i}}\right)_{test}, \tag{3.14}$$

where $\rho_{o,e,test}$ and $\rho_{o,i,test}$ are calculated stagnation densities at the compressor exit and inlet, respectively, based on measured variables during test operation, and $\rho_{o,i,ref}$ is the reference density from Eq. 3.11. The only unknown in this relation is $\rho_{o,e,ref}$, which can be calculated by rearranging Eq. 3.14,

$$\rho_{o,e,ref} = \rho_{o,i,ref}\left(\frac{\rho_{o,e}}{\rho_{o,i}}\right)_{test}. \tag{3.15}$$

Next, the work coefficients are equated between the test and reference conditions:

$$\left(\frac{h_{o,e}-h_{o,i}}{{U_t}^2}\right)_{ref} = \left(\frac{h_{o,e}-h_{o,i}}{{U_t}^2}\right)_{test} \tag{3.16}$$

where $h_{o,e,test}$, $h_{o,i,test}$, and $U_{t,test}$ are calculated directly from measured variables or through the use of REFPROP with measured variables as inputs. Similarly for the reference conditions, $h_{o,i,ref}$ and $U_{t,ref}$ may be calculated, leaving $h_{o,e,ref}$ as the only unknown. Equation 3.16 may be rearranged to solve for the stagnation enthalpy at the exit based on reference conditions,

$$h_{o,e,ref} = h_{o,i,ref} + {U_{t,ref}}^2\left(\frac{h_{o,e}-h_{o,i}}{{U_t}^2}\right)_{test}. \tag{3.17}$$

Using $\rho_{o,e,ref}$ and $h_{o,e,test}$ calculated from Eqs. 3.15 and 3.17, respectively, as input parameters, the total pressure and total temperature at the compressor exit under reference conditions may be calculated (using REFPROP),

$$\rho_{o,e,ref}\ ,\ h_{o,e,ref} \rightarrow P_{o,e,ref}\ ,\ T_{o,e,ref}\ . \tag{3.18}$$

And thus, corrected total pressure ratio,

$$TPR_{corr} = \frac{P_{o,e,ref}}{P_{o,ref}}\ , \tag{3.19}$$

and corrected total temperature ratio,

$$TTR_{corr} = \frac{T_{o,e,ref}}{T_{o,ref}}, \tag{3.20}$$

can be determined.

### 3.2.2 Effects of Correcting for Density and Work Coefficient

The density and work coefficient correction outlined in Eqs. (3.14) through (3.20) was applied to circumferentially traversed data at 100% $N_c$ for both a cold day and a hot day, shown in Figure 3.4. As a result of this correction process, the difference between the cold and hot day performance is reduced, but the shift is small. The percent difference between the measured $TPR_{test}$ and the corrected $TPR_{corr}$ is on the order of 0.06%; this is shown in Figure 3.6 for the 3% and 4% TC configurations. These data are presented as a function of corrected mass flow rate which has been normalized by a nominal loading condition half way up the speedline. The largest difference between the measured $TPR_{test}$ and the corrected $TPR_{corr}$ is on the order of 0.065% (or 0.00087 in TPR). This is smaller than the measurement uncertainty and is not a discernable shift if shown with the data in Figure 3.4.

The combination of ambient temperature, pressure, and relative humidity on the hot days resulted in densities and work coefficients similar to that at reference conditions. Therefore, data acquired on the hot days were corrected significantly less compared with the data from the cold days. Although it may appear there is a trend associated with loading condition, the correction differences from choke to stall are due to a gradual shift in ambient conditions that occurred while acquiring the data. Also, the 3% TC cold day data have a jump between 0.9 and 0.95 normalized corrected mass flow rate because this speedline was acquired on two different days. The four points closest to stall were acquired on a day with colder ambient inlet temperature, requiring a larger shift in work coefficient and density compared to those at higher flow rates.

Although this correction results in a small TPR shift that is less than the measurement uncertainty, it has been applied to all data (both overall compressor data and interstage data) presented in the remainder of the chapter to eliminate potential differences.

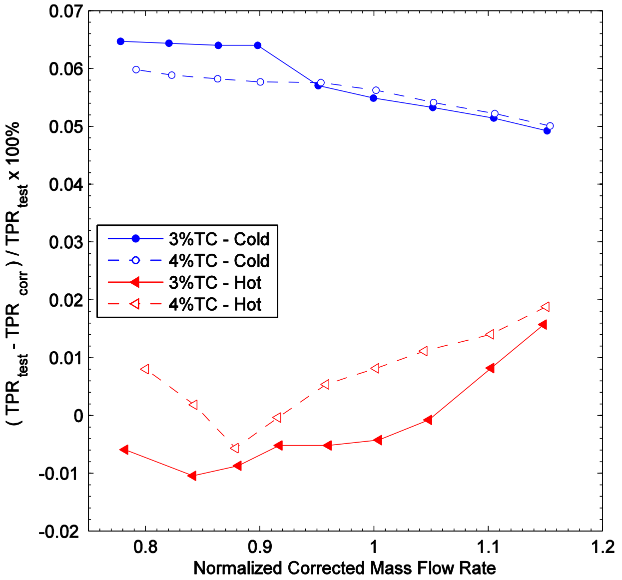

Figure 3.6 Percent difference change in TPR with density and work coefficient correction on a hot and cold day

## 3.3 Reynolds Number Considerations

Reynolds number is the fundamental non-dimensional quantity which is derived from non-dimensionalizing the Navier-Stokes equation, and it represents the ratio of inertial forces to viscous forces. When conducting compressor tests subject to varying ambient conditions, complete similarity cannot be ensured for all non-dimensional parameters. Standard operation allows for blade tip Mach number to be held constant between reference conditions and test conditions through corrected speed. To look at the effect of Reynolds number on compressor performance, this study considered multiple definitions of Reynolds numbers with different length scales and velocities. Smith (1964) comments on these choices and suggests blade chord as the appropriate length scale because it has the greatest effect on blade boundary layer development compared to other length scales. For this reason, blade chord was used as the length scale for all Reynolds numbers defined for this study. Smith also notes that the velocity should be selected based on the location where viscous effects are the greatest.

Two Reynolds number definitions were considered. The first uses rotor tip speed, $U_t$, and chord, $c$, for the length scale,

$$Re_{machine} = \frac{\rho U_t c}{\mu}. \tag{3.21}$$

This definition is commonly used by other authors and is representative of the machine Reynolds number. However, when considering loss development on blading, it is more appropriate to use the inlet velocity to each blade row, $v$ or $w$ (absolute or relative frame of reference), and chord,

$$Re_{blade} = \frac{\rho v c}{\mu}. \tag{3.22}$$

This alternate definition is more representative of airfoil performance. Changes of length scales due to thermal growth are neglected in this analysis compared to the more significant changes of flow velocities and fluid properties, leaving chord and radius constant for all operating conditions.

Large shifts in ambient conditions can cause the working fluid properties to change, therefore driving corresponding changes in Reynolds number. Standard compressor testing procedures allow for Mach number similarity between the test and reference conditions through a correction process for rotational speed, but there is no prescribed method to also maintain Reynolds number similarity. Reynolds number effects are often considered small and, thus, they are often neglected. However, deviations from the Reynolds number at reference conditions can become large on significantly hot or cold days. Previous authors (ASME PTC10) have defined a Reynolds Index,

$$Reynolds\ Index = \frac{Re_{test}}{Re_{ref}}, \tag{3.23}$$

which represents a ratio of the test Reynolds number to the reference Reynolds number. Reynolds Index can be used as a metric to gauge how far the test Reynolds number has changed from reference conditions due to differences in fluid properties. Figure 3.7 shows the Reynolds Index on the hot and colds days for the data presented in Figure 3.4. The test Reynolds number approaches a ±10% difference from the reference Reynolds number – a value which could become increasingly important for some compressors, especially those near the transitional Reynolds number. The changes in test Reynolds number arise from varying inlet conditions of temperature, relative humidity, and pressure. The variations in these ambient inlet conditions and the resulting Reynolds number experienced over the course of a year of testing in the Midwest United States are shown in Figure 3.8. While relative humidity and pressure affect Reynolds number, it is a strong function of inlet temperature.

Figure 3.8 shows the changes in both machine and blade Reynolds number, as defined by Eqs. (3.21) and (3.22), as a function of inlet temperature and relative humidity. The blade Reynolds number shown here is based on Rotor 1 inlet conditions, using the relative velocity at Rotor 1 inlet and the Rotor 1 chord. The blade Reynolds numbers for Rotor 2 and Rotor 3 are similar. These values should be compared with the loss curves for the airfoil shape. For these double circular arc airfoils, the profile loss is not affected by this change in Reynolds number. The stator inlet Reynolds numbers range from $3.5\times10^5$ to $4.5\times10^5$ and are similar through the compressor whereas the rotor inlet Reynolds numbers increase slightly through the machine. The blade Reynolds numbers are all above the critical value (about $2.5\times10^5$), and they exist in the minimum-loss region for the airfoils (NASA, 1965). Thus, the offset in total pressure ratio shown in Figure 3.4 on cold versus hot days is not associated with a transitional Reynolds number. Also, Figure 3.8 shows that the choice of blade Reynolds number versus machine Reynolds number definition does not result in a large difference in Reynolds number, especially when compared to the differences in Reynolds number associated with day-to-day variations in compressor inlet conditions.

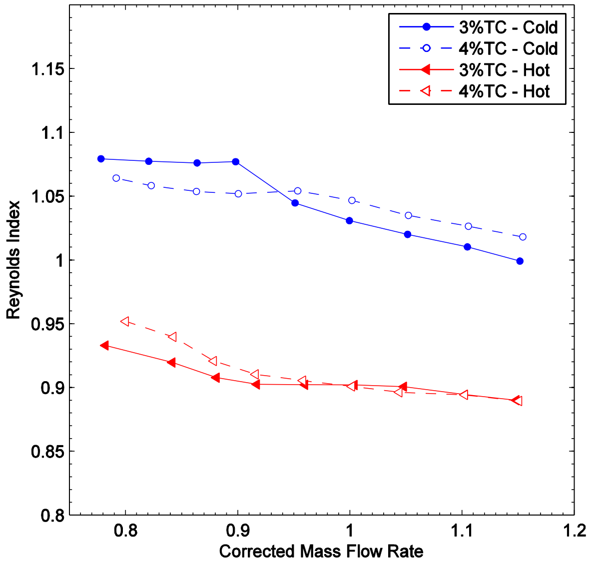

Figure 3.7 Reynolds Number Index on a hot and cold day

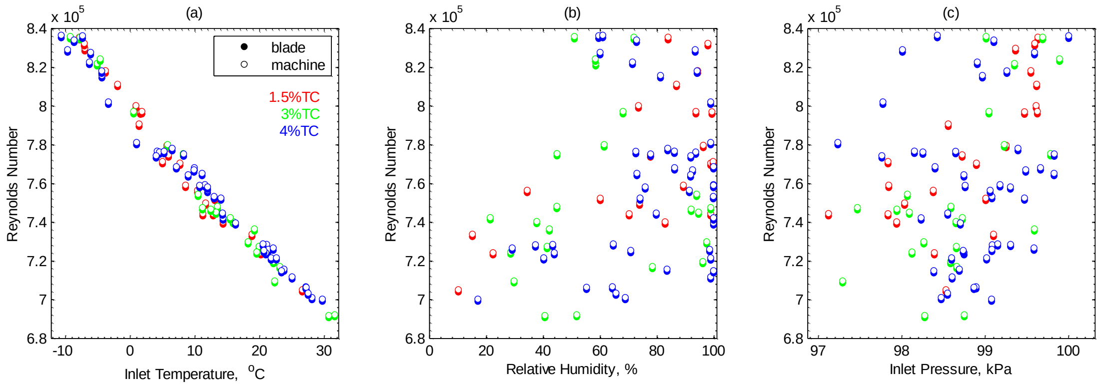

Figure 3.8 Machine and blade Reynolds number fluctuations with ambient conditions (a) temperature (b) relative humidity (c) pressure

## 3.4 Effects of Inlet Temperature

Despite the inclusion of the performance corrections for density and work and the additional consideration for Reynolds number variations, differences in compressor overall total pressure rise still persist. The differences in total pressure ratio shown in Figure 3.4 are consistent with untraversed data acquired over the course of a full calendar year at the facility, as shown in Figure 3.9 for all three tip clearances. Over the same range of ambient temperatures, the 4% TC is less affected, compared to the 1.5% and 3% TC configurations. The two smaller tip clearances have a general negatively-sloping trend of pressure ratio with increasing inlet temperature, whereas the 4% TC does not display a distinct trend with inlet temperature.

To understand the cause of these compressor performance differences, the pitchwise data downstream of each row were interrogated. Figure 3.10 shows total pressure (normalized by compressor inlet total pressure) downstream of each row at mid-span at a near-stall loading condition under cold and hot inlet conditions. On the cold days, each of the rotors appears to achieve more pressure rise uniformly across the vane pitch. At the stator exit planes, the cold day produces slightly narrower wakes. At the hub the stator wakes have almost no difference between the cold and hot days. On the other hand, near tip, the trends between a cold and a hot data are similar to the midspan data, if not stronger, shown in Figure 3.11 for 80%span. The Rotor 1 exit and Stator 2 exit at midspan (Figure 3.10) are the most different from the wakes shown in Figure 3.11. At 80%span, Rotor 1 has even more pressure rise difference at between the cold and hot day performance. And Stator 2 has a higher overall pressure.

Circumferentially averaging these data results in radial total pressure profiles downstream of each row for a hot and cold day; the results from this process are shown in Figure 3.12. The total pressure ratios have been normalized by the radial area-average so that the shapes between the different cases may be more easily compared. In this figure, the profiles are qualitatively similar, but there are small, yet appreciable differences near the tip and the hub. On a hot day, the tip region has more total pressure loss – a result which is most prominent at axial measurement planes downstream of Rotor 1 and Stator 2. This observation suggests differences in tip flows exist between the cold and hot days.

The flow physics in the tip region are dominated by rotor tip clearance flows which form large amounts of blockage and contribute significantly to loss development in compressors. Rotor tip clearances were measured with each point of the traversed data considered in the previous figures. The average rotor tip clearances are shown with the respective average total pressure rise in Figure 3.13 at the near stall loading condition. Cold day operation results in a small rotor tip clearance, while hot day operation results in a slightly larger rotor tip clearance due to differences in thermal growth between the aluminum casing shroud and stainless steel rotor. A 28 ºF (15.6 ºC) change in inlet temperature results in a change of rotor tip clearance height of approximately $2.4\times10^{-3}$ in. (an 8% difference for the baseline 1.5% TC configuration with a nominal 0.030 in. rotor tip clearance). While Figure 3.13 shows the expected result of decreased total pressure ratio with large increases in nominal rotor tip clearance, it also reveals that the small change in tip clearance due to changes in ambient temperature, and the corresponding change in measured total pressure ratio, follows the same trend. This result indicates that the small difference of performance which remains between the cold and hot days is likely due to small differences in tip clearance which are often considered negligible. When the ambient temperature varies, the thermal growth of the rotor and casing reaches a different steady state condition, and the radial stresses in the blades also change as a result of the changing mechanical rotational speed. These changes effectively produce a different machine depending on the ambient temperature.

The radial total pressure profiles between cold and hot days from all three nominal rotor tip clearance can be compared to see the gradual shift in performance at both a nominal loading and near stall loading condition, Figure 3.14 and Figure 3.15, respectively. Only the Rotor 1 exit and Stator 2 exit data are shown here because they exhibit the largest differences with tip clearance (as discussed with Figure 3.12). The profiles shapes for the 3% TC configuration fall between the 1.5% and 4% TC configurations for both loading conditions. The nominal loading condition in Figure 3.14 shows overall less difference in profile shape with increased tip clearance, but the trend is still present. At higher loading conditions, the rotor tip clearance flows are stronger and contribute to the increased losses at these conditions, and thus the shifts in radial profiles are more significant, as shown in Figure 3.15. The cold data have less total pressure loss at the tip, except for the 4% TC results. The trends at 4% TC are unclear, which is consistent with the observations from Figure 3.9 showing a less distinct trend in TPR with ambient temperature. This is because a 0.004 in. change in tip clearance is less significant for a 0.080 in. nominal rotor tip clearance than for a 0.030 or 0.060 in. rotor tip clearance. The trends at 3% TC are nearly as strong as those at 1.5% TC, an observation which could suggest the 3% TC configuration represents a critical point in the loss development with increased tip clearance. For example, for the Stator 2 exit profiles in Figure 3.15, the 3% TC is near the point where the profiles shift from having more loss in the hub to more at the tip.

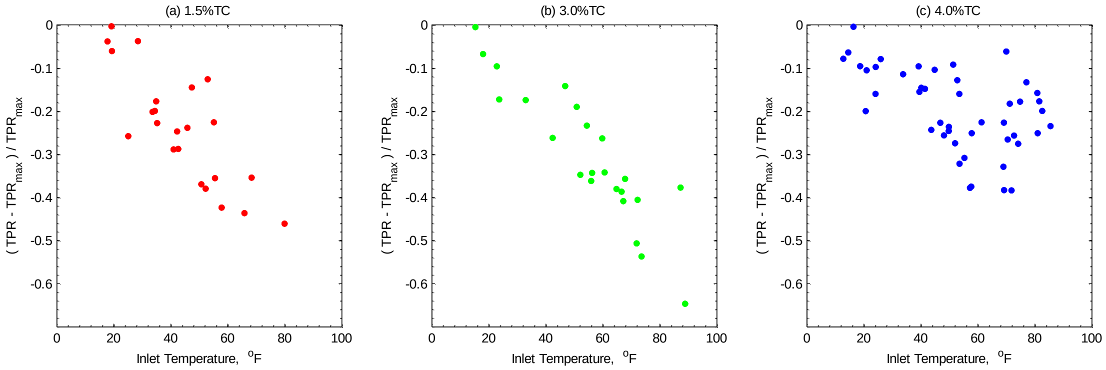

Figure 3.9 TPR variations with ambient temperature for three nominal tip clearances (a) 1.5%TC (b) 3%TC and (c) 4%TC

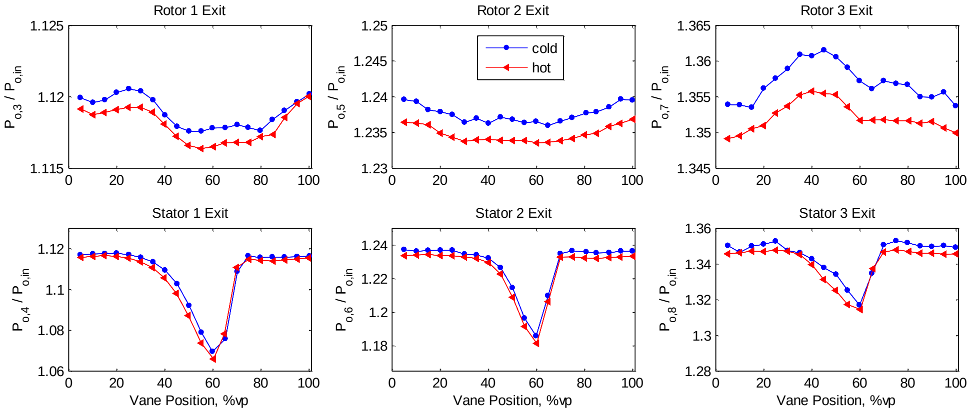

Figure 3.10 Total pressure wakes at midspan for 3%TC at near stall loading, hot and cold days

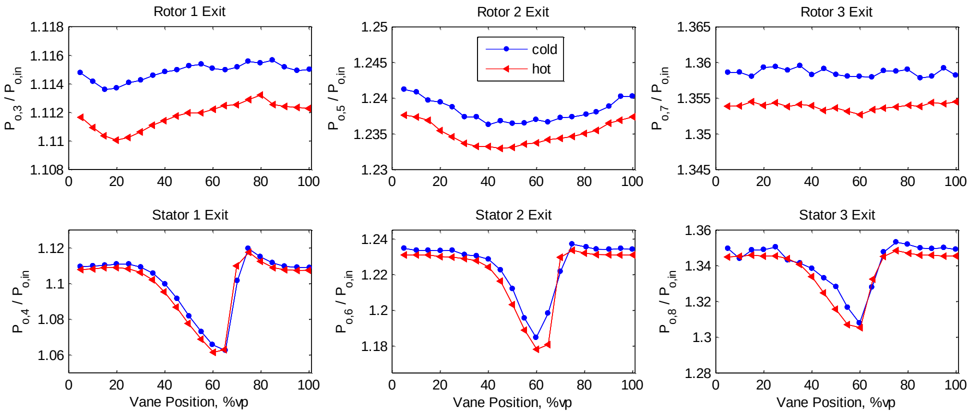

Figure 3.11 Total pressure wakes at 80%span for 3%TC at near stall loading, hot and cold days

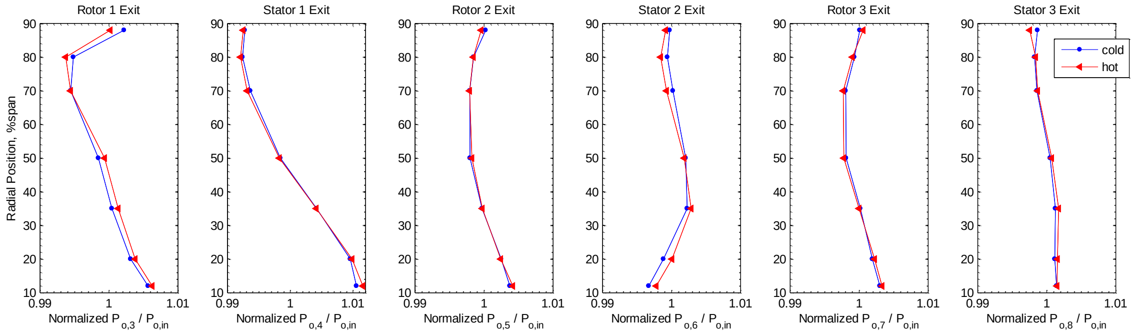

Figure 3.12 Radial total pressure profiles from traversed data downstream of each row for a cold and hot day for the 3% TC

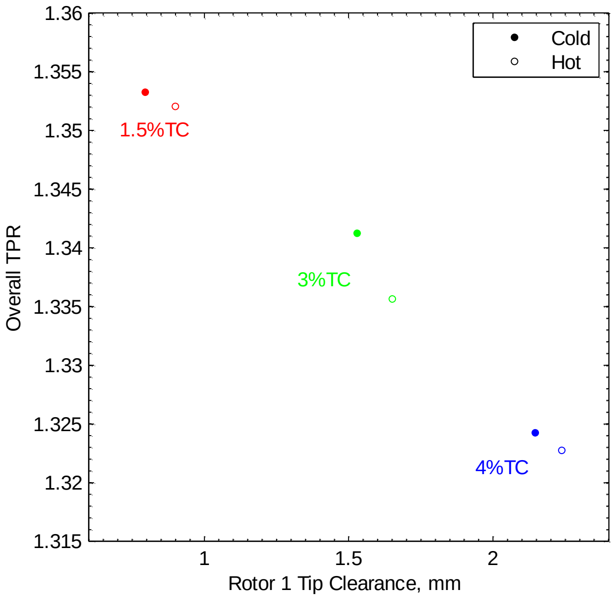

Figure 3.13 TPR trends with measured Rotor 1 tip clearance at a near stall operating condition

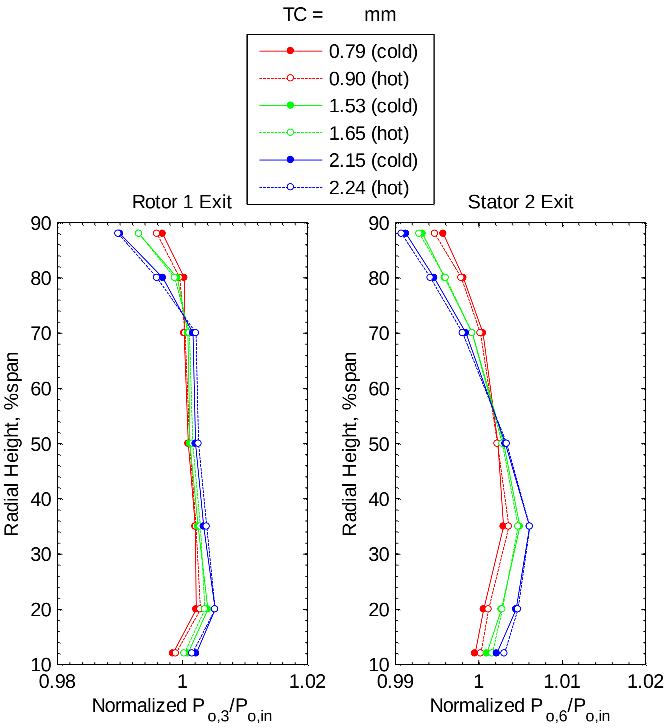

Figure 3.14 Radial profiles for three nominal tip clearances on a hot and cold day at nominal loading

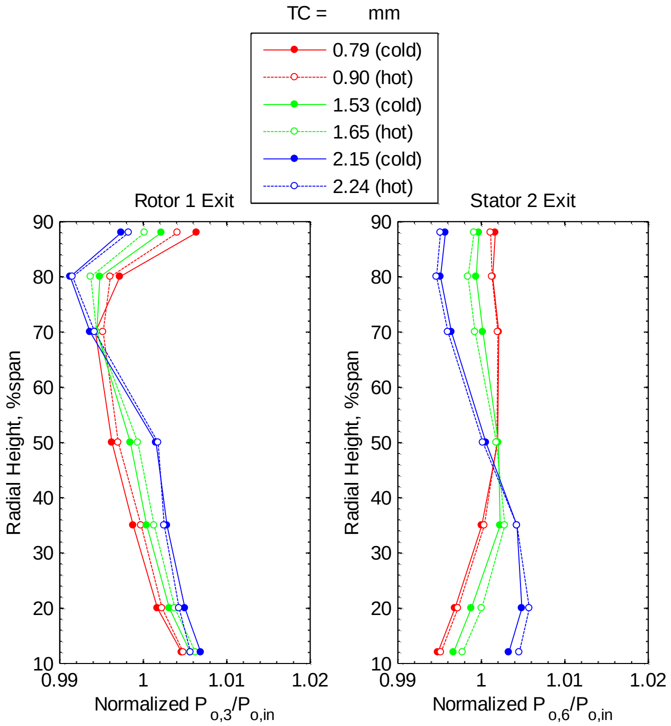

Figure 3.15 Radial profiles for three nominal tip clearances on a hot and cold day at near stall loading

# CHAPTER 4. FLOW VISUALIZATION

Surface flow visualization provides an outlet to observe and measure compressor flow patterns in a continuous manner as opposed to other discretized measurements, like probe traverses and hot film arrays that will be presented in later chapters. Not only does this technique allow for a quantitative assessment of separated flow on the stators and endwall flows, but these images have an unparalleled ability to communicate concepts simply and effectively. In particular, the technique used in this research highlights stator corner separations and the over-rotor endwall flows well. These regions contain important flow structures and behaviors which contribute significantly to overall compressor losses and their effects will be discussed in detail in later chapters with respect to various blade row interactions. Flow visualization tests have been carried out in many hardware configurations and operating conditions to examine several research topics in the Purdue Three-Stage Axial Compressor; the cases that will presented in this chapter are summarized in Table 4.1.

## 4.1 Overview of Flow Visualization

The powder paint and kerosene flow visualization technique used for this study most clearly defines surface flow patterns in recirculation regions. In axial compressors with shrouded stators, like the Purdue 3-Stage Compressor, corner separations are prevalent and the resulting profile loss contributes significantly to the overall losses of the machine (Cumpsty, 2004). These separations form where the vane boundary layer meets the endwall boundary layers. This discussion will focus primarily on the vane surface separations, but this phenomenon also causes the endwall to experience separations, and severe cases of this lead to hub corner stall (Horlock et al., 1966). Figure 4.1a shows an example image of a stator with corner separations at both the hub and tip endwall junctions on the suction side of a Stator 1 vane. Flow goes from left to right in the figure; the stator hub is at the bottom of the image and the tip is at the top as noted. This vane is positioned at the compressor casing splitline, and therefore may be imaged straight-on, whereas all later images presented were acquired from the trailing edge looking upstream. The corner separations are marked in Figure 4.1b and appear as semi-triangular patterns. For this Stator 1 vane at the high loading condition, the tip has a larger corner separation than the hub, as a result of many design factors including but not limited to flow angles, diffusion factor, and Rotor 1 performance. The streaklines in the separated regions reveal the recirculation patterns in the flow, as sketched in Figure 4.1c. Several critical points are identifiable in the surface flow topology. At least four saddle points (S) and four nodes (N) are present, which follows the rule given by Flegg (1974) that the number of saddle points and nodes must be equal for a vane row with no tip gap. There may be regions that have indistinguishable critical points due to resolution of paint or flow pattern complexities like the region where the tip and hub meet and near the endwalls. When comparing many Stator 1 vane images from the same dataset, there is another possible node location near the saddle point at the tip. This type of detailed analysis of the surface flow topology is useful to comparisons with computational models, particularly with respect to the acceptability of turbulence models.

Table 4.1 Summary of flow visualization cases presented

| Topic | Operating Conditions | Rows | Other Notes |
|---|---|---|---|
| Basic Surface Topology | HL | S1 | |
| Baseline Surface Flows | NL, PE, HL | S1, S2, S3 | |
| CFD comparison | HL | S3 | |
| Rotor Tip Clearance | NL, HL | S1, S2, S3 | 1.5%, 3%, 4%TC |
| Endwall Flows | PE, HL | R1, S1, R2, R3 | 1.5%, 3%, 4%TC |
| Instrumentation Effects | HL | R2, S2, S3 | |
| Variability | HL | S1, S2 | 1.5%, 3%, 4%TC |

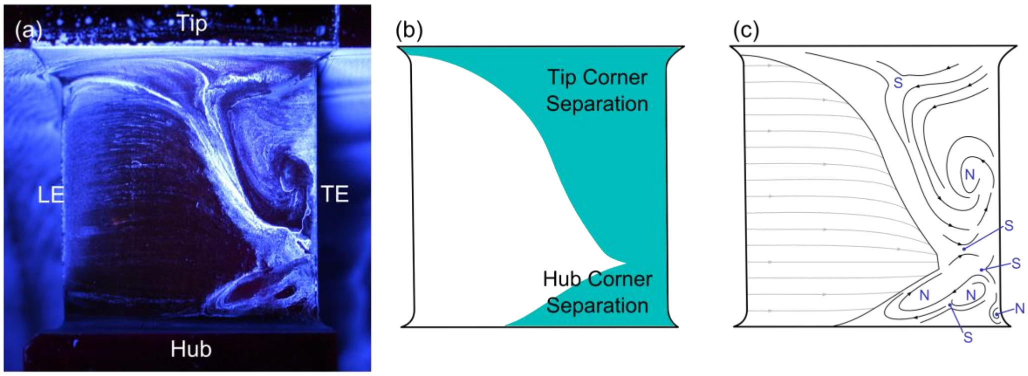

Figure 4.1 Basic surface flow topology for Stator 1 at the high loading condition (a) image, (b) corner separations, and (c) drawn flow topology with saddle points (S) and nodes (N) labelled

### 4.1.1 Effects of Loading Condition

Figure 4.2 presents an overview of the suction side surface flow visualization images on Stator 1, Stator 2, and Stator 3 at the four loading conditions. The image of

Stator 1 at peak efficiency loading, Figure 4.2d, is labelled indicating the vane hub, tip, leading edge (LE) and trailing edge (TE). This image orientation will remain consistent throughout this chapter unless otherwise noted. As loading increases, the compressor experiences a stronger adverse pressure gradient which makes the boundary layers both along the endwalls and the vane suction surface more susceptible to separations. As each of these flows weaken, the secondary flows formed at their junctions become stronger, and thus, the corner separations grow in size. The corner separations also increase in size further downstream through the compressor, where Stator 3 has larger separations than Stator 1. The flow conditions in the rear stages contain increased turbulence intensity, no defined freestream due to stronger secondary flows, and more unsteady disturbances due to wakes from upstream blade rows. All of these factors influence boundary layer transition and separation, particularly the unsteadiness from upstream wakes, which make these processes periodic. The increased wake interactions and stronger secondary flows result in earlier vane boundary layer separation in the rear stages of the compressor. (Mayle, 1991; Halstead et al., 1994; Cumpsty, 2004)

At the nominal loading condition shown in Figure 4.2a-c, all three stators have larger recirculation regions at the tip compared to the respective hub regions. The amount of separated area increases with each downstream stator, though Stator 1 and Stator 2 are quite similar. These trends fall within expectations of this relatively low loss operating condition but are also specific to the design of the compressor. When loading is increased from nominal loading to the peak efficiency loading condition, this trend changes, and each stator’s separation pattern is unique. Changes in the radial distribution of the flow with increased loading are specific to the compressor design and are governed by various aspects of stage matching (Cumpsty, 2004). The flow patterns on Stator 1 are similar at nominal and peak efficiency conditions, whereas the Stator 2 and Stator 3 hub corner separations grow more and both have boundary layer separation along the entire span. At peak efficiency, the Stator 2 tip still has a larger separated region than the hub, while the Stator 3 hub and tip separations are nearly equivalent. For this case shown in Figure 4.2d-f, Stator 1 experiences similar inlet conditions as in Figure 4.2a at nominal loading, but the effects of increased loading, stronger wakes and adverse pressure gradient are more substantial to the inlet conditions for Stator 2 and Stator 3. All three vanes have large increases in corner separation size at the hub and tip between the peak efficiency and high loading condition (Figure 4.2g-i), which is consistent with the large increased losses expected at high loading conditions. By high loading, Stator 1 has full spanwise boundary layer separation. Stator 2 and Stator 3 have separations extending much further forward on the vane surface. The final images, Figure 4.2j-l, are at the near stall loading condition. This operating point is at 5%stall margin and the flow at this condition contains high levels of loss and unsteadiness. The flow visualization shows that all three stators have significant suction side boundary layer separation. The tip region (approximately 75%-100%span) of Stator 1 is completely separated, beginning from the leading edge. This is difficult to see in Figure 4.2j, but can be seen in Figure 4.3, looking downstream at the leading edge.

These increases in separation between peak efficiency and high loading correspond well to total pressure loss changes between the two loading conditions. Circumferential vane traverses with seven-element total pressure rakes and casing static pressure taps positioned between each blade row as described in Chapter 2 were used to calculate total pressure loss coefficients, $Y_p$. Loss coefficients were defined as the difference in total pressure across the vane row normalized by the dynamic pressure at the inlet of that vane row like the loss comparisons later in Section 5.2. These data were circumferentially and radially area-averaged to provide an overall total pressure loss coefficient for all three stators at each operating condition and the results are summarized in Table 4.2 as a percent difference from the nominal loading condition. For example, the overall total pressure loss coefficient across Stator 1 increased by 3.3% difference between nominal loading and peak efficiency, but the increase from peak efficiency to high loading is significantly more. This trend is consistent for all three stators and not surprising. The overall compressor efficiency at the nominal loading condition is near peak efficiency, while the high loading condition is much less efficient (Berdanier and Key, 2015).

The surface patterns at the high loading condition have several identifiable nodal points and saddle points in the surface topology of all three stators. The spiral node in the tip recirculation region at the trailing edge of Stator 3 is visible in all three loading conditions. For the nominal (Figure 4.2c) and peak efficiency conditions (Figure 4.2f), it is about the same size and is located at 60%span, but at the high loading condition (Figure 4.2i), it grows in size and moves down to midspan. Analyzing the movement of the surface topology provides more evidence to how the separations grow and where the flow shifts between each test case.

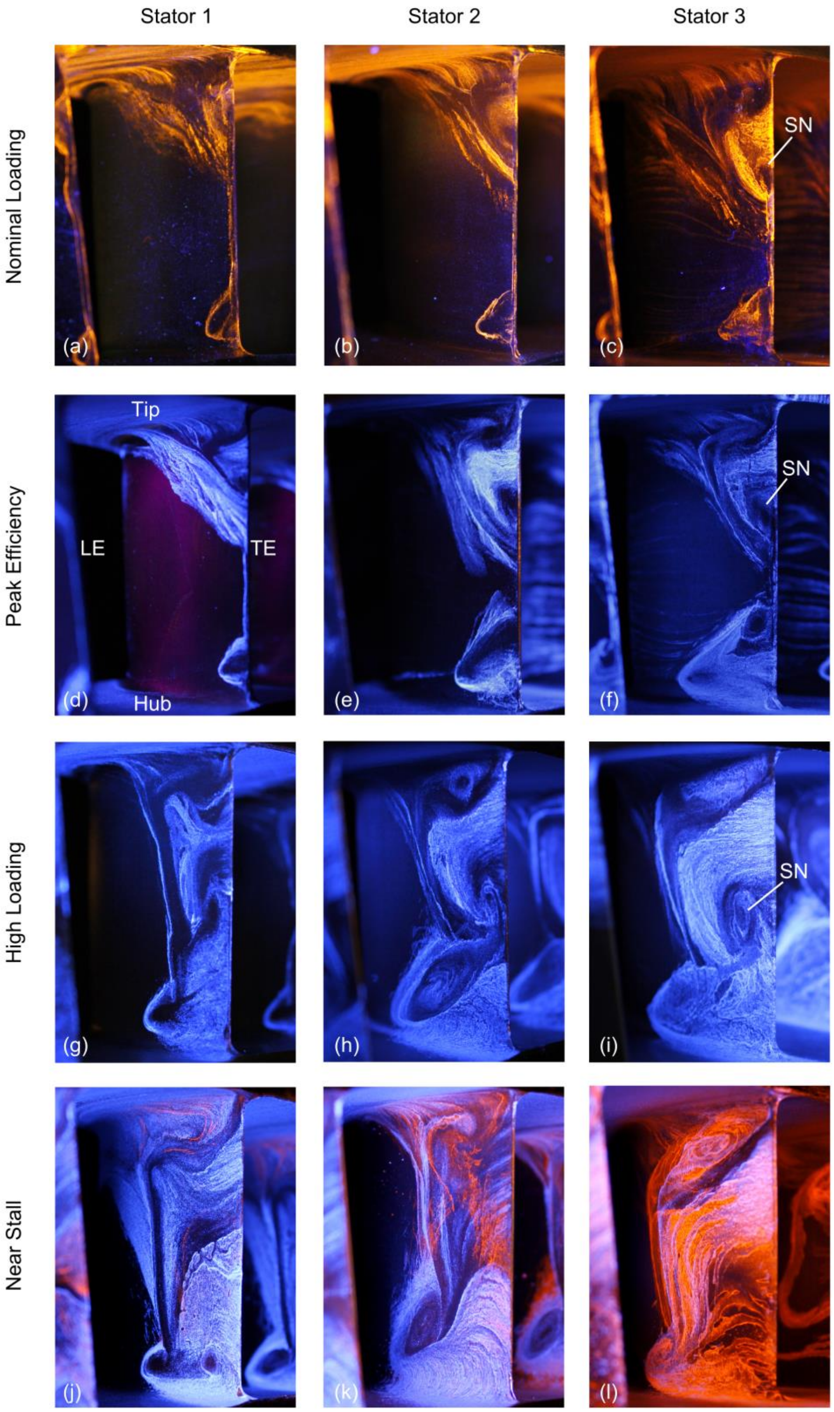

Figure 4.2 Surface flow visualization of corner separations for Stator 1 (left), Stator 2 (middle), and Stator 3 (right) at three loading conditions: nominal loading (a-c), peak efficiency (d-f), high loading (g-i), and near stall (j-l)

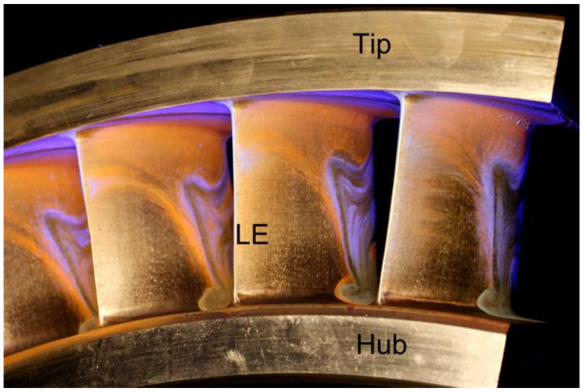

Figure 4.3 Stator 1 at near stall conditions viewed from the leading edge looking downstream

Table 4.2 Summary of percent difference in loss coefficient from nominal loading

| Operating Condition | S1 | S2 | S3 |
|---|---|---|---|
| Peak Efficiency | 3.3% | -1.1% | 4.8% |
| High Loading | 27.2% | 48.6% | 44.2% |

### 4.1.2 Comparison with CFD

Surface flow visualization like those presented in Figure 4.2 can be particularly useful for comparison with CFD and allows model developers to better understand where their codes fall short. Figure 4.4 shows a comparison to CFD of the Stator 3 suction side surface flow at the peak efficiency loading condition. The model used for comparison in this study is a steady, three-dimensional, Reynolds-averaged, Navier-Stokes (RANS) solver with a fourth-order, Runge-Kutta solution to finite volumes with numerical dissipation which is typical for compressor designers to use in the design sequence. The model assumes axisymmetric flow by solving for only a single passage for each row and uses mixing planes to transfer information between the stationary and rotating reference frames. A Baldwin-Lomax algebraic turbulence model was used; lower order turbulence models are common for turbomachinery industry design practices. The rotor tip clearance was modelled with a periodic boundary condition. Further details on these computations can be found in Monk (2014). The streamlines shown for the CFD, Figure 4.4b, are calculated at a distance of four grid cells off the vane surface. The hub corner separation matches well between the experiment and model. The size of the separated region is a bit smaller in the model, but the spiral node is in the same position. The losses at the tip, on the other hand, are largely under predicted in the model. This is likely because the rotor tip leakage flow was not modelled well, which is a common issue in turbomachinery CFD. Gupta et al. (2003) and VanZante et al. (2000) present issues encountered with various tip flow models. The experiment shows that the corner separations from the two endwalls nearly meet at about 40-50%span, but the model’s tip corner separation only extends down to 75%span and the mid-span flow does not separate.

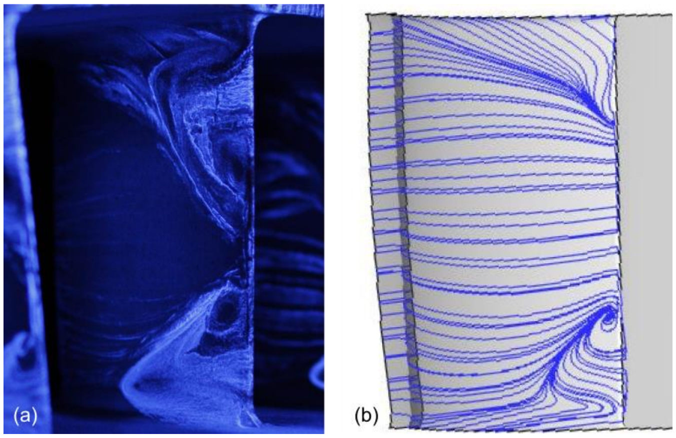

Figure 4.4 Comparison of surface streaklines on Stator 3 suction surface between (a) experiment and (b) CFD (Monk 2014) at the peak efficiency loading condition

## 4.2 Rotor Tip Clearance Effects on Stator Loss Distribution

Rotor tip leakage flows affect efficiency and stability in axial compressors. Increased rotor tip clearance allows more flow to jet from the pressure side to the suction side of the blade. This generates a larger tip leakage vortex (or region of high unsteadiness, recirculating flow) resulting in additional blockage near the tip endwall at the inlet of each stator (Wisler, 1985). This blockage forces the flow to redistribute causing more fluid to travel through the lower half of the vane span. This locally increases the mass flow rate and unloads the hub, resulting in reduced corner separations at the hub. Meanwhile the large blockage at the tip due to the increased tip leakage flow weakens the tip region and increases the amount of separation on the downstream vane. These trends can be observed on all three stators and are presented for two loading conditions, nominal loading and high loading, at three different rotor tip clearances (TC):

1.5%, 3%, and 4% TC, based on annulus height. The 1.5%TC is the baseline configuration shown in all previous figures and data in this research.

Figure 4.5 shows surface flow visualizations at the nominal loading condition for all three stators and increasing rotor tip clearance, with 1.5%TC in Figure 4.5a-c, 3%TC in Figure 4.5d-f,and 4%TC in Figure 4.5g-i. Even at this relatively low loss loading condition, the increase in rotor tip leakage flow is significant enough to shift the flow in the downstream stator from the tip to the hub. All three stators experience an increase in blockage at the tip as rotor tip clearance increases (moving down through the figure) resulting in an apparent increase in the tip corner separations. This is especially clear between the 1.5%TC and 3%TC cases, where the tip corner separation begins further upstream along the vane suction surface and extends deeper along the span. The hub corner separations of Stator 1 and Stator 2 reduce in size from 1.5%TC to 3%TC but do not appear to become any smaller when the clearance is increased to 4%TC. The Stator 3 hub corner separation remains similar in size for all three rotor tip clearances. Based on these observations, the increase in rotor tip clearance has a larger effect from 1.5% to 3%TC at the nominal loading condition. The growth in blockage from the tip leakage vortex from 3%TC to 4%TC does not significantly change the radial shift of the flow. These results correspond well with the steady total pressure traverse presented by Berdanier and Key (2015). Furthermore, they reveal that even at a low profile loss operating condition, the effects of increased rotor tip clearance are enough to alter the surface flow for the downstream stators.

The high loading case is presented in Figure 4.6 using the same format as the previous figure. This loading condition is further from the design point of the compressor and has more loss and higher pressure rise compared to the nominal loading condition. As a result, the rotor tip clearance effects on stator loss are more dramatic. The amount of boundary layer separation on Stator 1 is nearly unchanged between 1.5%TC (Figure 4.6a) and 3%TC (Figure 4.6d), but there is evidence of a stronger rotor tip leakage vortex in the streamlines at the tip. The 3%TC has significant radial shift of streamlines at the top 14%span of the separated region, as noted in the figure as radial flow (RF). When the rotor tip clearance is opened up to 4%TC (Figure 4.6g), the effects of increases in blockage at the tip are far more significant. The stator tip corner separation originates from near the vane leading edge and the radial streamlines extend down through the outer 22%span, while the hub has been strengthened by the redistributed flow resulting in a smaller hub corner separation. The surface topology of Stator 2 changes the most of the three vanes for the high loading condition. At the baseline tip clearance in Figure 4.6b, there is a large spiral node (SN) in the hub corner separation, the tip region has a smaller node, and the two separations intersect at about 42%span. Opening the rotor tip clearance up to 3%TC (Figure 4.6e) redistributes the fluid through the Stator 2 passage due to the increased blockage from the Rotor 2 tip leakage vortex and is evident in the shifts of the two nodes. The spiral node at the hub is reduced in size and originates further downstream compared to the baseline tip clearance. The small node at the tip is less defined and surrounded by more radial streamlines. The point where the two corner separations meet has moved down to about 37%span. At the largest tip clearance (4%TC) in Figure 4.6h, the spiral node at the Stator 2 hub is smaller and only reaches about 23%span. The tip now has strong radial streamlines extending down to about 72%span. Similar to both Stator 1 and Stator 2, Stator 3 experiences a shift in radial location of losses with increased tip clearance. The hub corner separation decreases in size indicating the hub is strengthened as the tip clearance increases. And the tip region contains large amounts of blockage with significant radial flow shown in the surface streamlines apparent at 3%TC (Figure 4.6f) and 4%TC (Figure 4.6i). These results show that changes to rotor tip clearance have a significant effect on the behavior of the downstream stator's surface flow field. The size and shape of corner separations which were altered with increased tip clearance affect the resulting stator wake shapes and radial profiles. These data indicate weakened tip and strengthen hub with increased tip clearance and are complemented by the work of Berdanier and Key (2015a).

The addition of flow visualization to an investigation like increased rotor tip clearance can provide a detailed description of the flow physics within the stator passage that contribute to changes in measured stage loss. The surface streamlines are data which cannot be obtained as easily with any other technique and are valuable for comparison with CFD, which often is a major aim of large experimental test campaigns.

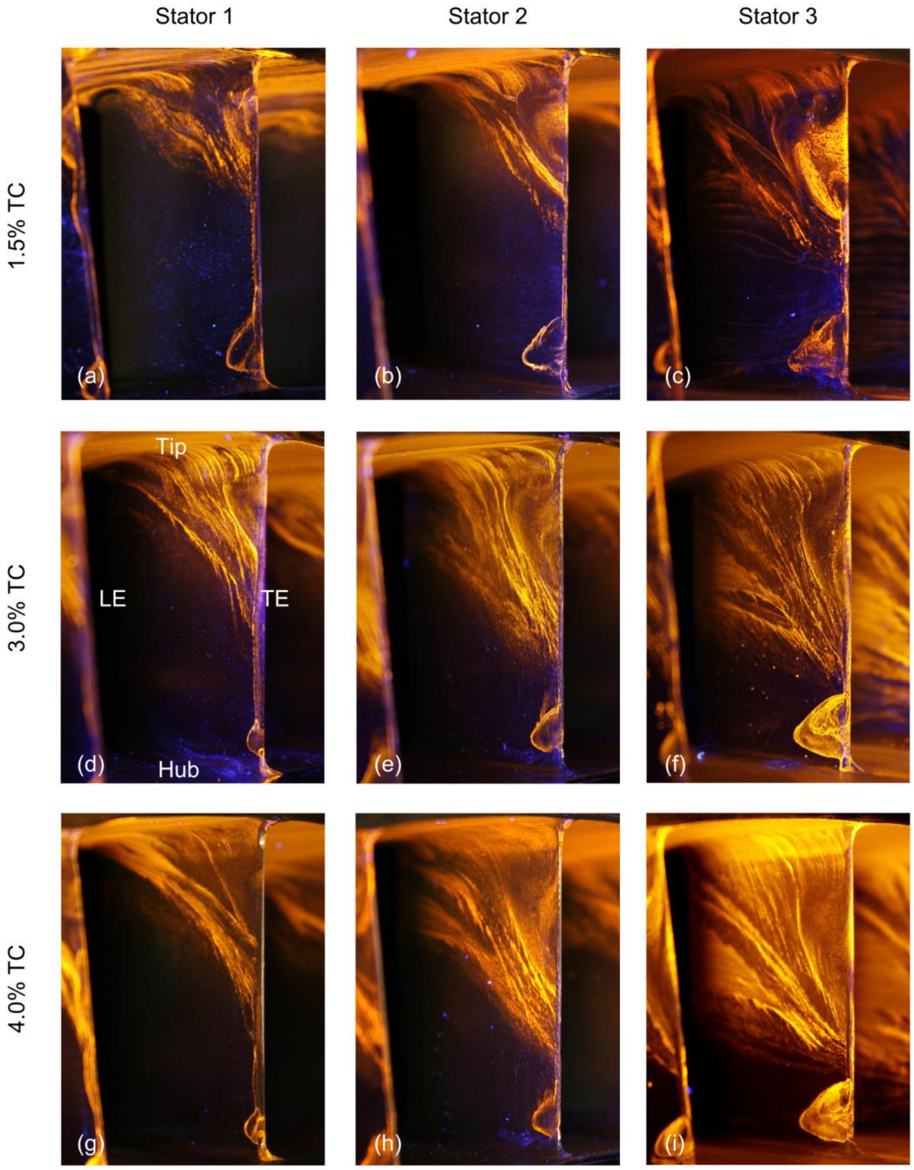

Figure 4.5 Flow visualization of vane corner separations at nominal loading for three different rotor tip clearances, 1.5% (a-c), 3% (d-f), and 4%TC (g-i)

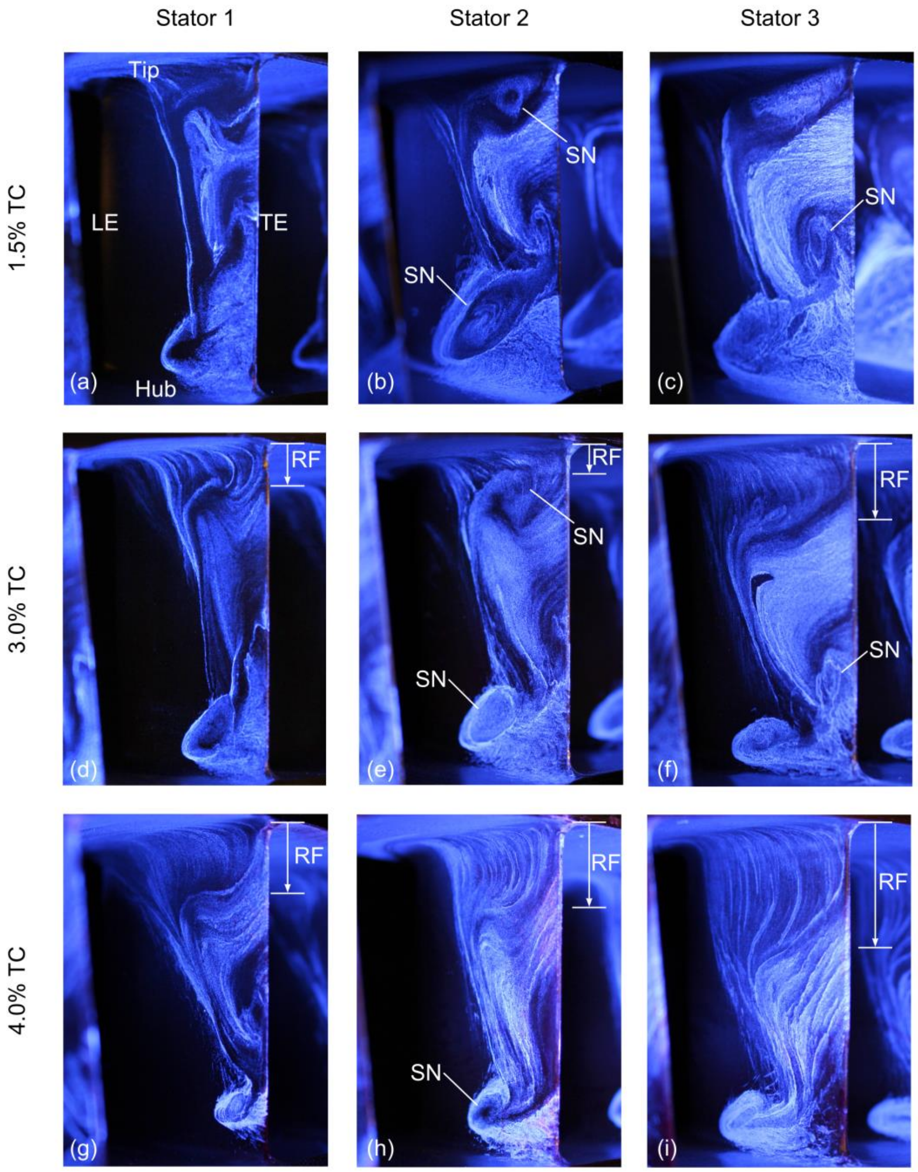

Figure 4.6 Flow visualization of vane corner separations at the high loading condition for three different rotor tip clearances, 1.5% (a-c), 3% (d-f), and 4% TC (g-i) with surface flow features highlighted: the extent of radial flow (RF) streamlines and movement of some spiral nodes (SN)

## 4.3 Endwall Flows

The flow visualization technique also deposits paint in streamline on the casing endwall, providing insight to the movement of some secondary flows. The patterns which form over the rotors include the bulk endwall fluid motion, stator wakes including the corner separations, and rotor tip leakage flow. These flows are presented for each rotor at nominal and high loading for three rotor tip clearances.

### 4.3.1 Rotor Endwalls

Surface flows along the casing endwall over Rotor 2 at the baseline tip clearance are show in Figure 4.1. Flow is from left to right, and rotor rotation is downward. The stator vane locations are outlined and a representative rotor blade is located in the proper axial position. The Stator 1 (S1) wakes are visible immediately downstream of the Stator 1 trailing edge. Their trajectory angle is roughly that of the absolute flow angle until they reach the Rotor 2 (R2) leading edge at which point they begin to turn and follow the rotor rotation.

The effects of the Stator 1 wakes are visible and form an interaction pattern near the Rotor 2 leading edge. This pattern is evidence of the movement of the Rotor 2 tip leakage vortex which is caused by the rotor passing through the Stator 1 wake low momentum fluid. As the rotor enters the stator wake, a deficit in absolute velocity, it experiences an increase in incidence, as show in Figure 1.2. The change in incidence increases the loading on the rotor and moves the peak pressure rise upstream, and thus the pressure graduate across the rotor tip from pressure side to suction side is stronger. The larger gradient drives more leakage flow and the movement of peak pressure rise alters the location of the jet. Both of these factors alter the trajectory and size of the blockage (vortex-like structure) which forms from the tip leakage flow. Downstream of this, the surface streamlines over Rotor 2 follow the rotor rotation direction. At the Rotor 2 trailing edge, there is a distinct change in the angle of the streamlines; downstream of Rotor 2, the surface streamlines follow the absolute flow angle and more closely align with the Stator 2 (S2) inlet metal angle. Near the leading edge of Stator 2, the effect of the Stator 2 potential field is visible in the streamlines.

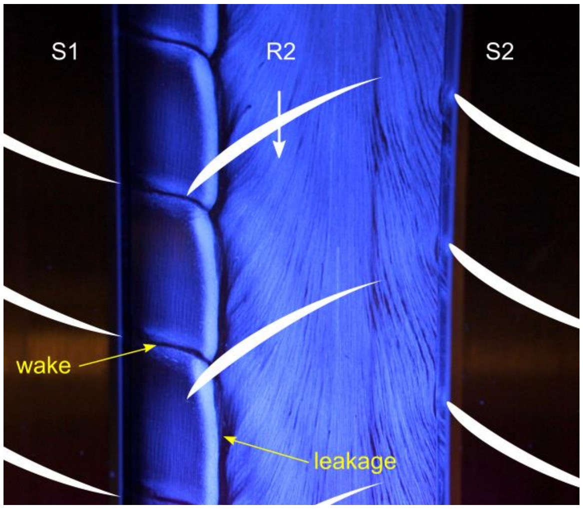

Figure 4.7 Flow visualization of casing endwall over Rotor 2 at HL

The over-rotor streamlines for all the rotors for the baseline tip clearance are shown in Figure 4.8 at the nominal (top) and high (bottom) loading conditions. The orientation is consistent from the previous figure. The rotor tip leakage flow pattern is located further downstream at about 40% axial chord for the nominal loading condition. This is expected for this loading because the peak pressure rise of the rotors occurs further from the leading edge. The also corresponds well to over rotor pressure data presented by Berdanier (2015c). The stator wake – rotor tip leakage pattern is weaker at this loading because the stator wakes are not as deep or as wide, less loss and separation as seen by the stator surface flows. With smaller incoming wakes, the rotor responds less because the change of inlet conditions is shorter and less drastic. It is also of interest that this interaction even occurs over Rotor 1. The IGV wakes are small and thin due to their favorable pressure gradient, but these data show that they still influence the Rotor 1 leakage flow.

Note the lack of definition in the endwall flow patterns for the nominal loading in Figure 4.8 is a function of image collection quality and not the flow physics. The baseline casing nominal loading condition dataset was the first after preliminary flow visualization testing and was not as practiced as later tests.

The high loading condition has much stronger definition and images under UV light which provide higher contrast, highlighting the surface flows. The upstream shift in tip leakage flow in clear between the nominal and high loading conditions, this interaction occurs between the Rotor 2 leading edge and about 20% axial chord. This interaction pattern is unique for each rotor. Rotor 1 has a quick shift upstream at the IGV wake, but remains at a constant axial position for the rest of the vane passage. Rotor 2’s shift upstream is larger circumferentially, but it remains relatively straight for the rest of the vane passage except for a slight shift downstream immediately before the Stator 1 wake. The pattern over Rotor 3 has the most movement, the curvature of the pattern makes it never remain at the same axial position and particularly different from Rotor 1 and Rotor 2 in the amount of downstream shift before interacting with the Stator 2 wake.

Presented in the same manner, Figure 4.9 shows the over-rotor flows for the 3%TC case at nominal and high loading. The paint coverage and images for the nominal loading condition are of better quality for this dataset compared to the baseline rotor tip clearance. In the nominal loading Rotor 3 image there are also disturbances in the streamlines between Stator 2 wakes due to some leakage flow which is coming from above the stator shroud in the casing. With better contrast in this figure, it is clear that the amount the leakage path shifts in the wake is greater at high loading compared to nominal loading. This is due to the high loading condition producing deeper wakes and a large absolute velocity deficit will result in a larger change in relative flow angle (rotor incidence). At high loading, the bump in the tip leakage pattern for Rotor 1 is more pronounced. The patterns for Rotor 2 and Rotor 3 have more curvature. This observation of more curvature in the pattern is due to the thickening of the upstream wakes, especially at the tip, at the higher loading and larger rotor tip clearances. Thicker wakes which gradually return to the main passage or ‘freestream’ flow on the suction side will cause the downstream rotor to experience a gradual change in incidence as it leaves the wake fluid. The jump in the pattern is sharp as the rotor approaches the stator wake because the pressure side leg of the wake is steep. The higher contrast images also reveal another pattern in the flow. Downstream of tip leakage pattern, there is a less well-defined region with less paint deposited in a negatively sloped trajectory (in the direction of rotor rotation and toward the trailing edge). This pattern appears in each image, but it is most pronounced over Rotor 2 and Rotor 3 at high loading. It is possible that this is the upstream wake trajectory.

At the 4%TC, shown in Figure 4.10, the shift in trends are again slightly more dramatic, particularly at high loading. The increased width in stator wake width at the tip draws the rotor tip leakage pattern over Rotor 2 and Rotor 3 to become more asymmetric in curvature. These rotor enwall flow data compliment the over-rotor pressure measurements acquired by Berdanier (2015c).

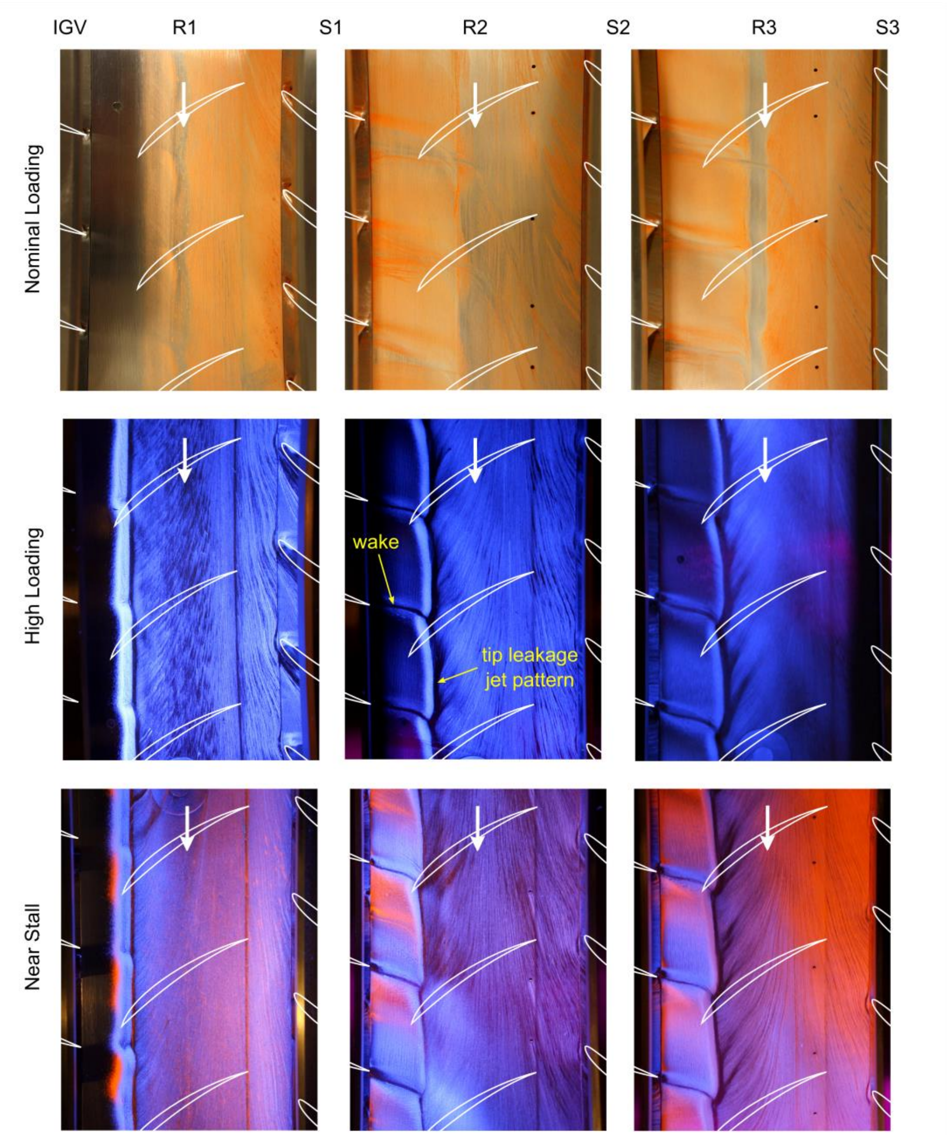

Figure 4.8 Flow visualization of casing endwall over each rotor at NL and HL for the baseline rotor tip clearance (1.5%TC)

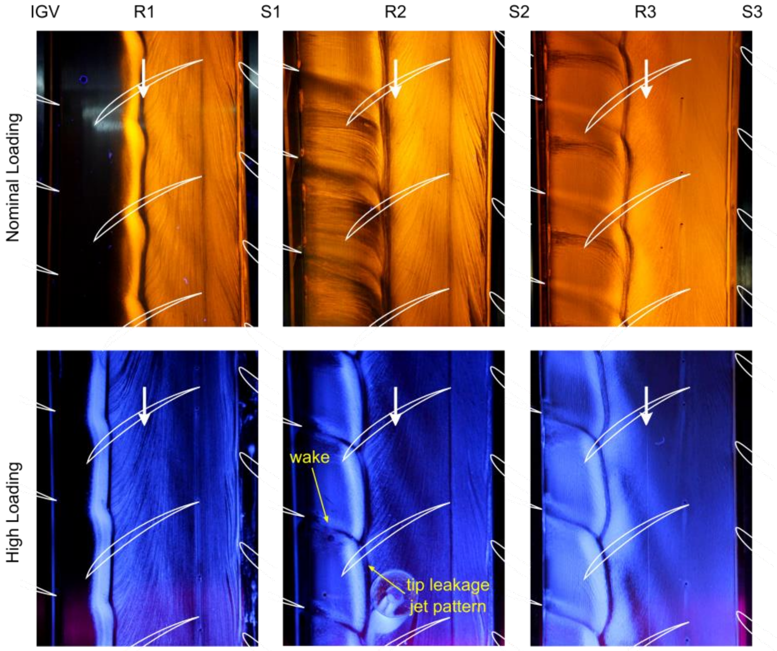

Figure 4.9 Flow visualization of casing endwall over each rotor at NL and HL for 3.0%TC

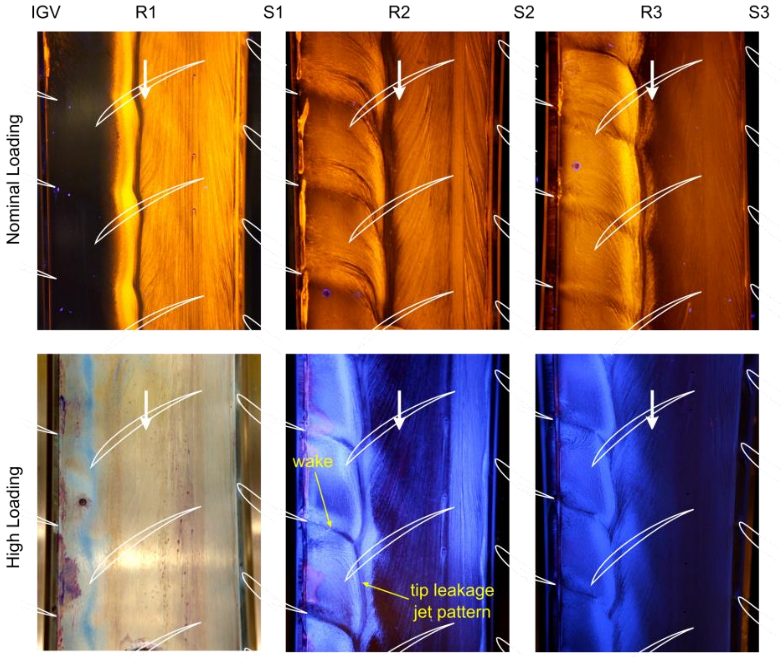

Figure 4.10 Flow visualization of casing endwall over each rotor at NL and HL for 4.0%TC

### 4.3.2 Stator Endwalls

The endwall streamlines also highlight the behavior of the secondary flows in the stator row. Figure 4.11a shows the casing endwall in the Stator 1 passage for the nominal loading condition. This image is looking upstream at the stator trailing edge with the tip of the vane to the right and the hub to the left. The endwall fluid has low momentum and is subject to the pitchwise pressure gradient in the vane passage. This drives the endwall fluid to sweep from the pressure side of one vane, across the passage to the suction side of the adjacent vane. The blue streamlines in Figure 4.11a enter the vane passage near mid-passage or slightly closer the pressure side. By the time these streamlines reach the trailing edge they are closer to the suction side of the passage, as a result the endwall fluid experiences overturning. This fluid also interacts with the formation of the corner separation, which is visible in Figure 4.11b. This is a high loading case with large tip corner separations originating near the vane leading edge. This interferes with the overturning of the endwall flow because the corner separation encompasses a larger portion of the endwall. The endwall fluid enters the corner separation region and is carried onto the vane suction side. In Figure 4.11c, the stator tip endwall is shown for the near stall case. As shown earlier in this chapter, this loading condition has very large corner separations. The streamlines along the endwall in the stator passage reveal that the tip corner separation for Stator 1 encompasses nearly half of the passage at near stall loading conditions.

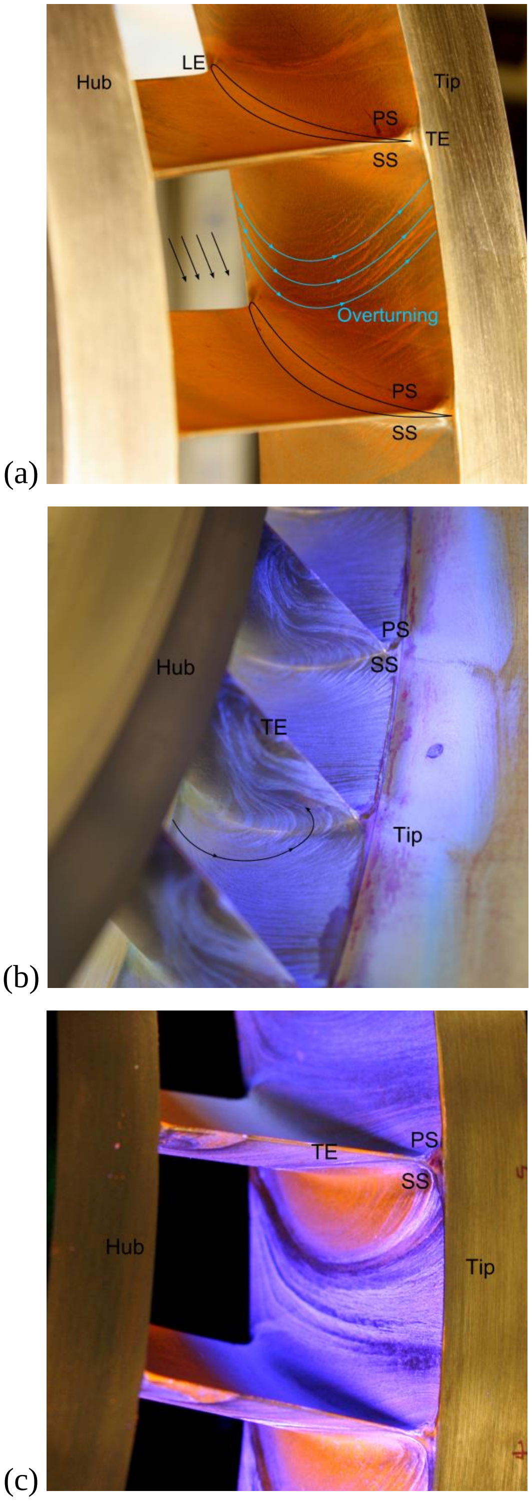

Figure 4.11 Secondary flows on stator passage endwalls highlighting (a) overturning, (b) entrainment in to corner separation (c) large tip corner separation

## 4.4 Influence of Instrumentation and Hardware Features

The utility of surface flow visualization goes beyond corner separations, endwall flows, and comparison with CFD; it can provide useful insight to other flow patterns and the effects of real geometry features on compressor flow physics. Paint is deposited throughout the flowpath during these tests marking many flow features tied to effects of instrumentation or flowpath imperfections. Since CFD models may not include the as-built and as-instrumented geometries, this is a way to visualize the impact of these hardware features on the flow field. Figure 4.12 highlights several of these patterns.

Many instrumentation ports are accessed through the casing, and thus, the endwall flow reveal many of these ports. Like the images of the over-rotor endwall flow, detail of the sinusoidal nature of the streamlines affected by the potential fields of the vanes is shown in Figure 4.12a. This image is looking up at the casing endwall, near the Stator 2 leading edge. In addition to the Stator 2 potential field, this picture includes a 6.35mm (0.25in) diameter instrumentation port and the disturbance it creates in the surface streamlines. This disturbance is minimal and not close to any active measurement locations.

The paint mixture also highlights any leakage path, for example Figure 4.12b. Viewing Stator 3 (S3) at the spilt line of the compressor casing, small leakage paths are apparent at both the tip and hub. The leakage path at the hub is likely affecting the hub corner separation on this vane, and thus, this vane is not used in any analysis.

Figure 4.12c shows two special Stator 2 vanes (the two left-most vanes), which do not have fillets at the tip but instead feature a small tip gap at the casing-side shroud. This feature provides the capability to replace the metal casing block over these stators with a window, allowing optical access into this vane passage. However, the presence of the tip gap results in leakage flow and a different flow pattern, compared to the shrouded vanes. Figure 4.12c shows the effects of the tip gap on both the tip corner separation as well as the casing endwall flow pattern. On the casing near the suction side of the two vanes with a tip gap, it is clear there is a jet of fluid moving perpendicular to each of the vanes. These observations are valuable and guide researchers to accurately measure flow phenomena and not hardware anomalies. All four vane rows in this compressor include two vanes with the tip gap feature. Stator 2 (pictured) and Stator 3 each have a downstream instrumentation port which could be affected by this irregular flow pattern, and therefore alternate circumferential ports at the same axial position are used for data acquisition downstream of these stators. This image in Figure 4.12c also supports observations from Figure 4.7. The surface patterns which form around a leakage jet are characterized by a thickening of deposited paint followed immediately by no paint. Thus, flow visualization can be used to gage the effects of accommodations for instrumentation on the flow field and facilitate the determination of their acceptability.

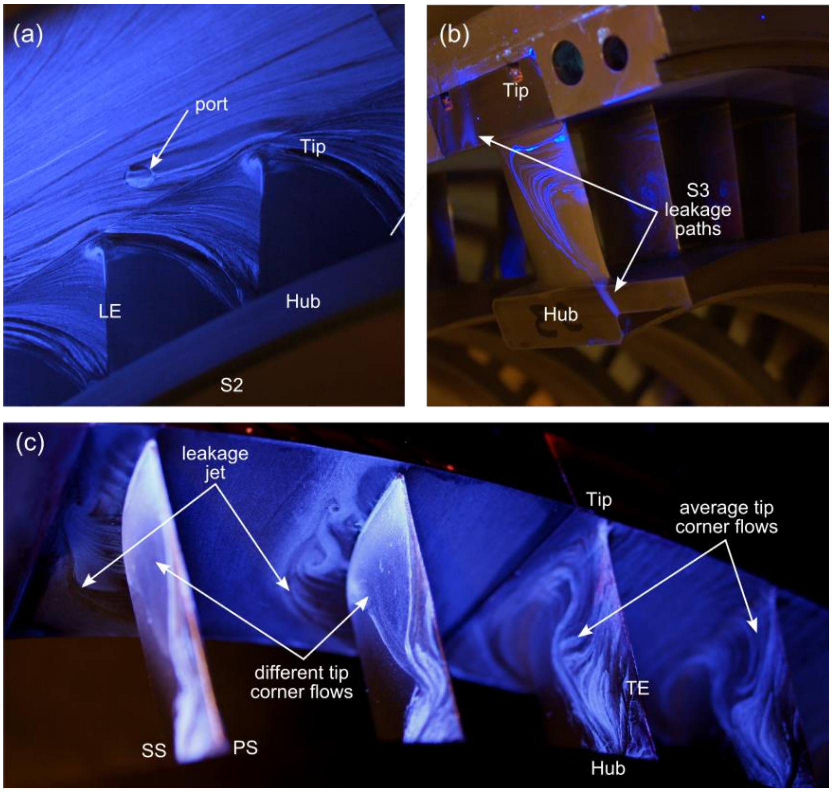

Figure 4.12 Flow visualization of other features: (a) rake ports, (b) leakage paths, (c) vanes with tip gap for instrumentation

## 4.5 Separation Line Variability

The flow visualization tests which focused on a single operating condition at a time enabled an analysis of the vane-to-vane variability. During these tests all three circumferential locations noted in Figure 2.6 were used for injection of the same paint mixture at the AIP which resulted in good surface flow patterns for a larger number of vanes in each row, particularly Stator 1. For a test at the high loading condition, 29 of the 44 Stator 1 vanes had clearly defined corner separations. Furthermore, during the imaging of the vanes, the camera angles were tightly controlled to ensure little variation between the pictures of each vane. This would allow the images to be directly overlaid and compare the amount of variation in size and shape of the corner separations.

An image processing and edge-finding code was used to analyze the vane-to-vane variability associated with the location of the corner separation. Each photograph was cropped to locate the vane trailing edge at the same position in each image, placing the hub and tip fillets in the corners of the image, as shown in Figure 4.13a. The RGB color values were separated for each pixel. Figure 4.13b shows the greyscale values of green from the image in Figure 4.13a. It may seem intuitive to use the value for blue, but the values are so high and glare on the “clean” portions of the surface cause the image to become washed out. The green values provide a sharp definition of the separation line while maintaining the details of the surface streamline patterns; a comparison of the RGB separation is shown in Figure 4.14. The matrix of green light values is converted into binary data, where the presence of green sets the pixel white, and the absence of green sets the pixel is black, Figure 4.13c. The threshold for presence of green was determined based on the sensitivity to small variations in amount to light between images without altering the separation line definition. Finally, an edge-finding scheme steps radially (vertically) through the image to locate the first and last pixel with a value of 1 (white) along each horizontal line, resulting in a picture of the separation streamline, Figure 4.13.

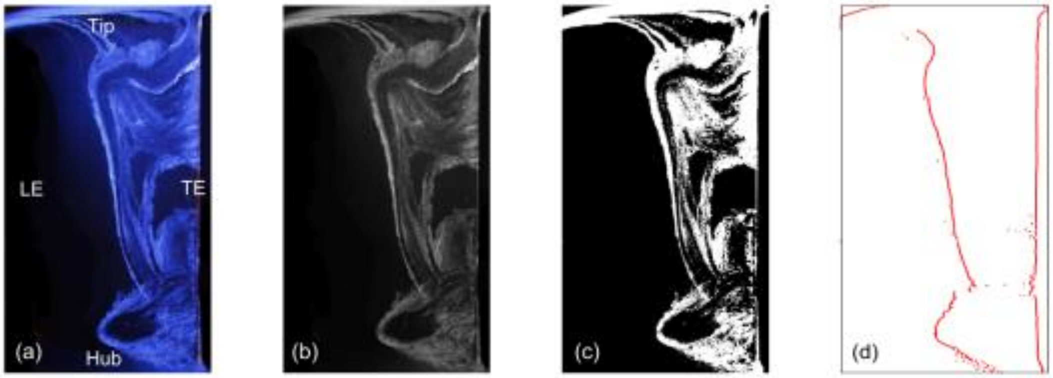

Figure 4.13 Process to identify separation line using: (a) original image, (b) RGB color separation, (c) binary image, and (d) recirculation region boundary

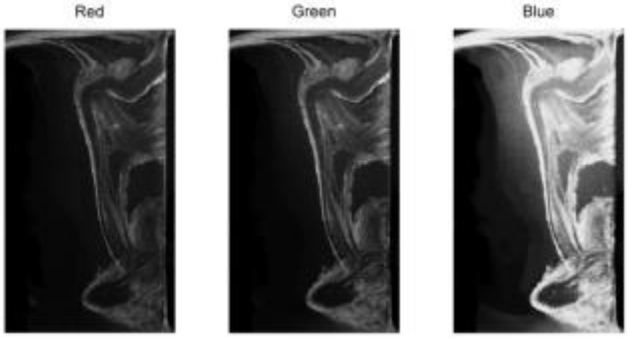

Figure 4.14 Comparison of RGB color breakdown for the blue paint

This procedure was repeated for 29 Stator 1 vanes. Figure 4.15 shows the separation streamlines from 29 Stator 1 vanes overlaid. In general, the corner separation pattern is quite repeatable. There are a few outlying profiles which are highlighted in Figure 4.15a. There are two hub corner separation lines which extend further upstream than all the others; these are colored red and labelled “A”. The hub corner separation of two vanes extends higher radially and further upstream; these are blue and labelled “B”.

A few others extend higher radially but are closer to the trailing edge, and these are the green profiles in region “C”. The profiles labelled A and C are experience flow disturbance from the wakes of the support struts located at the compressor inlet. The two vanes labelled B are both close to the strut wake trajectory and immediately adjacent to vanes which have flow-disturbing instrumentation features. This is discussed in more detail later in the results. There are instrumentation ports (for rake or other probes) immediately downstream of several Stator 1 vanes; these are labeled “Rakes” in Figure 4.15b. The surface flow patterns and separation lines for all but one of these vanes are grouped together. One of these positions would measure the performance of a stator which is influenced by a strut wake, and thus this position is not used for primary measurements. Additionally, the Stator 1 vane which is discussed in more detail and compared between many cases later in the paper is highlighted in red and labelled “Picture” in Figure 4.15b. This vane also lines within the average profiles. The largest variation in separation line location shown in Figure 4.15 is approximately 14% of the suction side length, while most are within a region that covers 7% of the suction side length. These observations provide confidence in the repeatability of this technique while offering a basis by which to identify outliers due to flow non-uniformities from struts or hardware differences, and it also provides a bound on possible vane-to-vane variability.

Finally, with separation lines for many vanes located around the compressor, the circumferential variability of the vane separation lines may be examined. Figure 4.16 shows the Stator 1 vanes broken into four groups based on circumferential position in the compressor. Beginning at the top splitline of the compressor and moving clockwise, Figure 4.16a shows vanes from 0-90°, Figure 4.16b shows 90-180°, Figure 4.16c shows

180-270°, and 270-360°. The top half of the compressor, 270-90°, appears to have the most variability in the upper half of the stator span, while the sector from 180-270° has the most in the hub region, including a couple of the outliners discussed previously. Generally, the region from 90-180° has the least separation line variability aside from one major outliner.

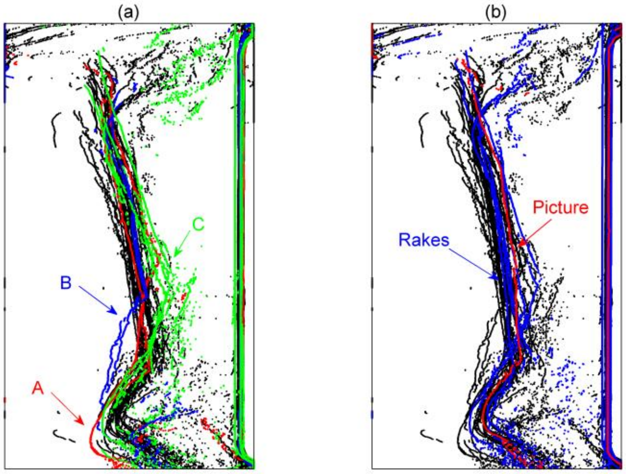

Figure 4.15 Separation lines of 29 Stator 1 vanes at the high loading condition with (a) outliers highlighted and (b) vanes of interest highlighted

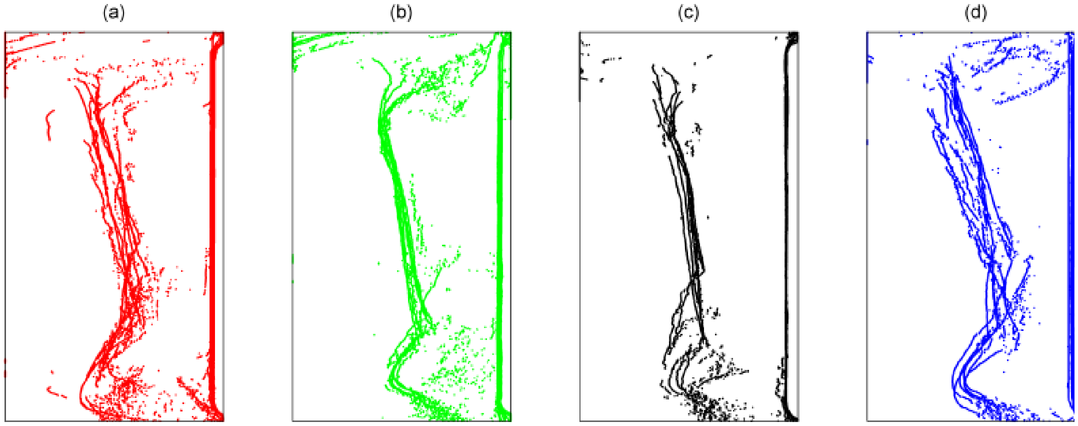

Figure 4.16 Separation line variability around the compressor where (a) 0-90°, (b) 90-180°, (c) 180-270°, (d) 270-360° clockwise from the top splitline

# CHAPTER 5. STEADY VANE CLOCKING RESULTS

As shown in the flow visualization, the stators flow fields in this compressor feature complicated 3-D separations. The vane flow fields are also affected by vane wakes from upstream stages. Vane clocking is a method to use blade row interactions to change the performance of the downstream row. By changing the relative circumferential positions of adjacent vane rows, the interaction between the upstream stator row’s wake and the downstream vane are altered. Before exploring the details regarding the unsteady flow physics of these interactions, an understanding of the extent to which these interactions affect time-averaged steady compressor performance must be established. In this chapter, vane clocking results from the Purdue three-stage compressor will be discussed as they relate to the Stator 1 wake convection and its effects on Stator 2 total pressure loss and knife seal leakage flows. Figure 3.1 illustrates the topics which will be covered in this chapter and from where the data were acquired in the flowpath. These experiments utilize seven-element total pressure rakes and static pressure taps in the casing between rows at axial positions 4, 5, and 6, as noted in Figure 3.1. The results will be presented in order of the flow path, beginning with the flow field upstream of Stator 2, and moving downstream to the Stator 2 exit.

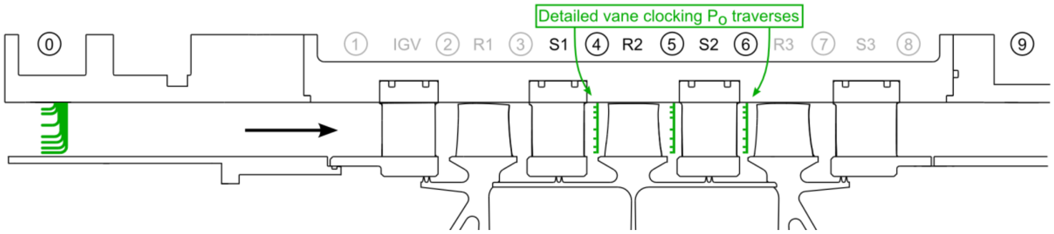

Figure 5.1 Summary of steady performance data collection

## 5.1 Flowfield Upstream of Stator 2

The total pressure field was characterized for all six clocking configurations at nine loading conditions along the 100% corrected speedline. The stagnation pressure field data include seven radial elements at every 2%vp downstream of Stator 1, Rotor 2, and Stator 2. Clear definition of the upstream flow field provides valuable information regarding the propagation, size, and shape of the Stator 1 wake, which are fundamental to the vane clocking mechanism.

### 5.1.1 Downstream of Stator 1

Total pressure data at Stator 1 exit (station 4) normalized by the area-averaged compressor inlet total pressure are shown in Figure 5.2 for the hub (12% span), midspan (50% span), and tip (88% span) regions at the peak pressure loading condition. All six clocking configurations are shown. The Stator 1 wake is the low total pressure region between 20% and 60%vp. The total pressure wake profiles from all six clocking configurations are repeatable and lay directly on top of one another, demonstrating: 1) the repeatability of the stagnation pressure and vane position measurements and 2) the consistency of the operating condition over the course of the long duration run (10-12 hours). The variation in Stator 1 wakes between clocking configurations in this figure is representative of that observed at the other eight loading conditions.

At the lower loading conditions (L1-L5), the Stator 1 wakes are mostly uniform in width and depth from hub to tip. At higher loading conditions, however, the Stator 1 loss increases and the wake grows, most significantly from midspan to the tip. Figure 5.3 shows total pressure contours (in the circumferential-radial plane) downstream of Stator 1 normalized by compressor inlet total pressure for all nine loading conditions. These data are one vane passage of data plotted twice assuming periodicity. The Stator 1 wake is uniform in width and depth from hub to tip at the lower three loading conditions (L1-L3) with only slight widening at the tip and hub regions. In contrast, at the higher loading conditions, like L8, the Stator 1 wake has a 10%vp wider wake at the tip compared with the hub, but the wake depths are similar from hub to tip. These observations are important to consider, because as the Stator 1 wake grows thicker and deeper, it encompasses more of the vane passage with a stronger total pressure deficit. This increases its interaction with the downstream rows, both how much wake fluid Rotor 2 chops and alignment with the Stator 2 leading edge, ultimately altering the Stator 2 performance.

### 5.1.2 Downstream of Rotor 2

The Stator 1 wakes convect downstream and diffuse, becoming wider and less deep. They are chopped into segments by Rotor 2 and turned as they pass through the blade row. Also, at high loading conditions, the Stator 1 wakes have significant skew after passing through the rotor blade row. Figure 5.4 shows contours of total pressure downstream of Rotor 2 / upstream of Stator 2 (station 5) normalized by compressor inlet total pressure for the nine loading conditions. The Stator 1 wake is the region of low total pressure (dark blue), which is wider and less deep in these data than those acquired at Stator 1 exit. At the L5 loading condition, the Stator 1 wake is mostly radial except at the hub, where it shifts by about 25%vp. As loading is increased, for example L7, the larger lean of the Stator 1 wake results in the wake position at the tip and hub being 50%vp out-of-phase. At some loading conditions, the Stator 1 wake diffuses more by the time it reaches the Stator 2 inlet (Figure 5.4 L7 at 50%span). These observations at the Stator 2 inlet are useful for the following discussion of results at the Stator 2 leading edge and downstream of Stator 2.

Stator 1 wake convection through the downstream rows is an important aspect of how vane clocking affects Stator 2 performance. With different compressor operating conditions, velocities and flow angles change, and thus, wake convection is affected. For example, the Stator 2 inlet total pressure data acquired at 20% span are shown in Figure 5.5 for configuration CL1 at the six loading conditions. Similar to the data shown in Figure 5.4, the low pressure regions of each series in Figure 5.5 is the Stator 1 wake; this is noted by the arrows. For the low loading condition (L1), the middle of the Stator 1 wake was at approximately 150%vp (or 50%vp) as marked by an arrow. As loading is increased, the Stator 1 wake convection path is shifted from 150%vp to 125%, 115%, 105%, 90%, 65%, 50%, 30%, and 20%vp for the L2 to L9 loading conditions, respectively. The Stator 2 leading edge will be at one location in the vane passage. Thus, for the same physical clocking offset (CL1 = 0%vp shown in Fig. 7), the level of interaction between the Stator 1 wake and the Stator 2 vane will change for different loading conditions.

While it may appear that L1 and L7 have similar impingement conditions, and L2, L8, and L9 have similar impingement conditions, these data are acquired half way between Rotor 2 exit and Stator 2 inlet - not at Stator 2 leading edge. These loading conditions (the lower versus the higher) have significantly different flow rates and velocities, so the wake convection from the rake position to the Stator 2 leading will differ. It would also be expected that L5 and the L8 cases should have opposite impingement conditions for CL1 at 20%span. Figure 5.6 compares these two loading conditions at CL1, as well as the pressure profiles of the vane clocking configuration half a passage out-of-phase, CL4. This shows that the position of the Stator 1 wake with respect to Stator 2 is the same for CL1 at L5 and CL4 at L8 at the hub. And the opposite is also apparent; the Stator 1 wake is in the same position for CL4 at L5 as it is for CL1 at CL8. These observations may hold true at the Stator 2 leading edge since these loading conditions have more similar flow rates and velocities, but require more information to be confirmed. The addition of Stator 2 leading edge total pressure measurements will strengthen the understanding of both the Stator 1 wake convection and Stator 1 wake impingement condition on the Stator 2 leading edge.

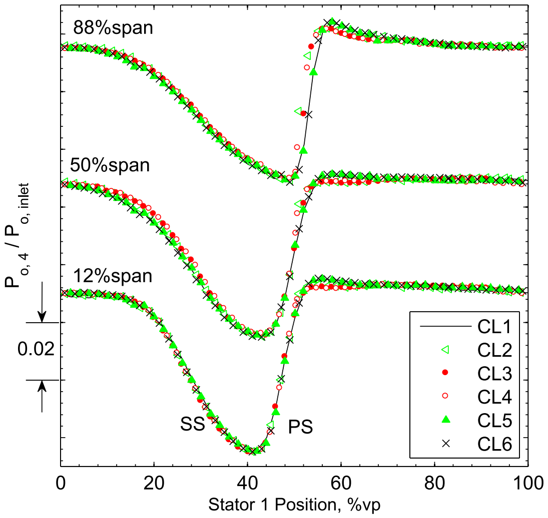

Figure 5.2 Stator 1 wakes at L8 for six clocking traverses at 12%, 50%, and 88% span

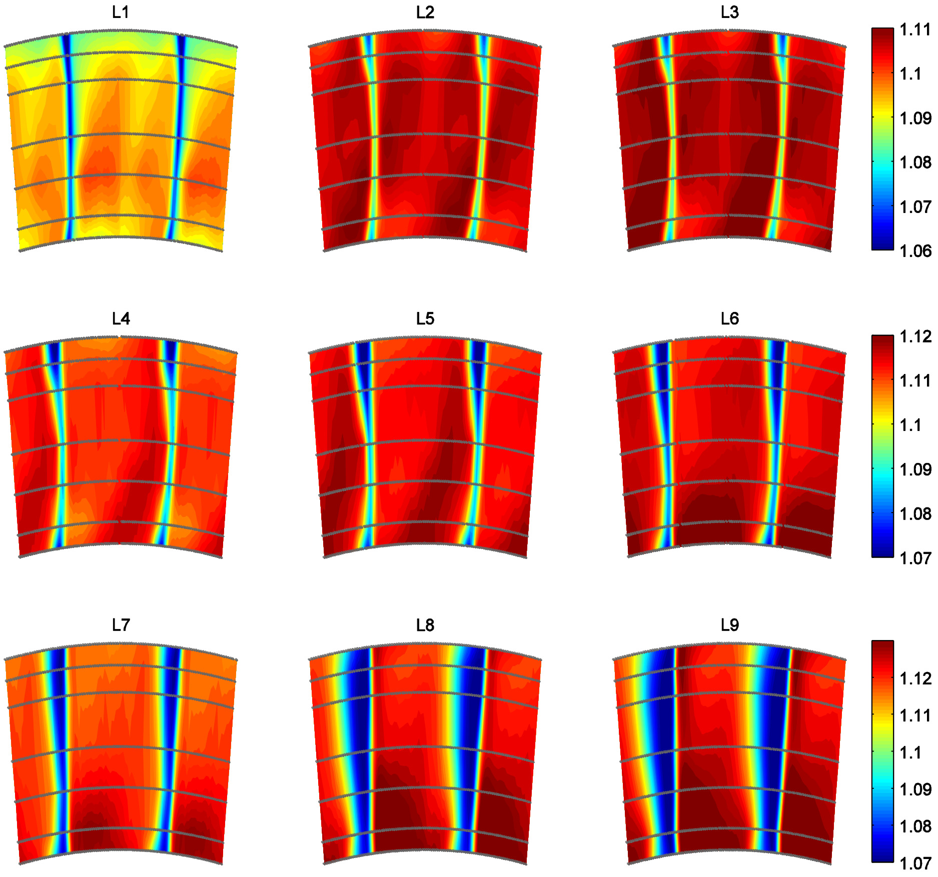

Figure 5.3 Stator 1 exit total pressure contours at the nine loading conditions

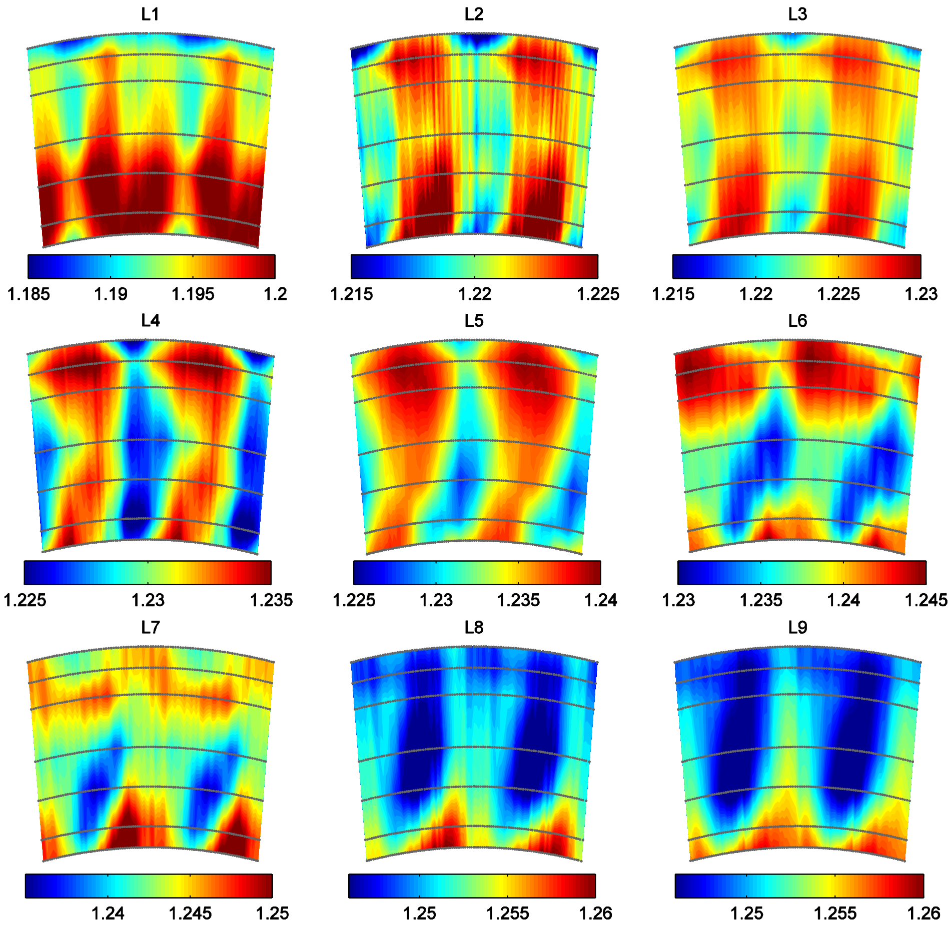

Figure 5.4 Rotor 2 exit total pressure contours at nine loading conditions

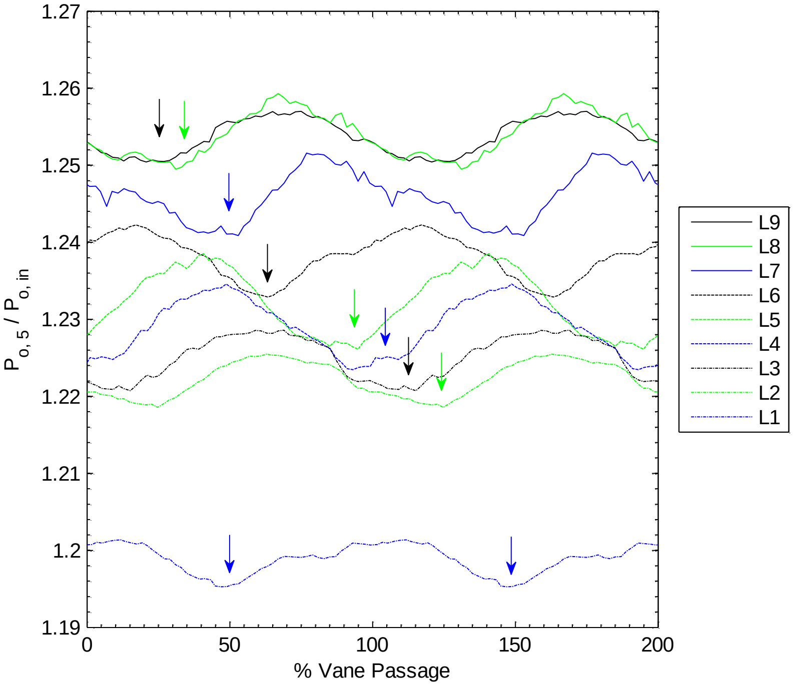

Figure 5.5 Rotor 2 exit total pressure for CL1 at 20%span for all nine loading conditions

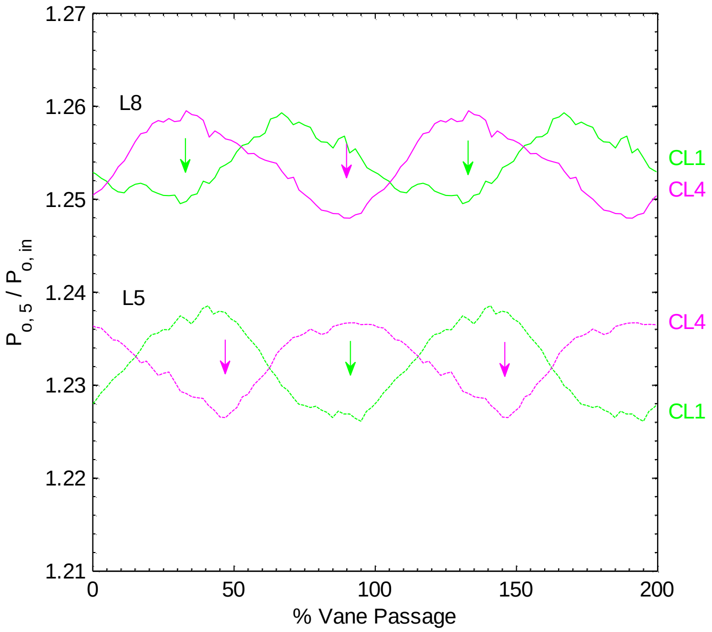

Figure 5.6 Rotor 2 exit total pressure for CL1 and CL4 at 20%span for L5 and L8

## 5.2 Vane Clocking Results Downstream of Stator 2

The total pressure flowfield downstream of Stator 2 was used to evaluate the Stator 2 performance under different clocking configurations at nine loading conditions. These data are presented as detailed wakes highlighting local vane clocking influences as well as averaged data providing -D values of the extent of vane clocking effects.

Figure 5.7 shows contours of total pressure downstream of Stator 2 normalized by area-averaged compressor inlet total pressure. The dots represent locations of data acquisition from the seven-element rake at 50 points across a vane passage. All six clocking configurations are shown for the L5 loading condition. The Stator 2 wakes are visible as radial strips of low total pressure (dark blue). The color scale has been adjusted to enhance the Stator 1 wakes, which are the green sections outlined with solid black lines. For clocking configuration CL4, the Stator 1 wakes are visible between the Stator 2 wakes, and it is close to the configuration where the Stator 1 passed through the middle of the Stator 2 vane passage at this loading condition. The movement of the Stator 1 wake across the Stator 2 passage for different clocking configurations is visible in these data. Clocking configuration CL1 is likely near the clocking configuration where the Stator 1 wake impinges the Stator 2 leading edge along most of the span for the high-design loading condition. The hub is about one configuration off from these impingement condition, with CL6 being the leading edge impingement configuration.  This is expected due to the Stator 1 wake skew observed at the Stator 2 inlet shown in Figure 5.4a.

Similar observations may be made for the other loading conditions. The Stator 1 wake leans at higher loading conditions, as shown in Figure 5.4, particularly at the high loading (L7) condition where the tip experiences Stator 1 wake impingement and the hub region has the opposite (Stator 1 wake passes through the middle of the Stator 2 passage) in the same physical clocking configuration, CL5. At the two highest loading conditions, L8 and L9, it is difficult to identify the Stator 1 wakes at the Stator 2 exit. The Stator 2 wake widths increase significantly, up to 60%vp, at these loading conditions making small changes in the mid-passage region difficult to distinguish. While these observations of the relative position of the Stator 1 wake with respect to the Stator 2 wake allow for an approximation of the leading edge impingement condition, they are not the clearest method to indicate impingement case.

Furthermore, the wake convection observations made from Figure 5.5 are also visible. For the hub region, the L5 and L7 loading conditions have almost opposite Stator 1 impingement conditions. At the station 5 (Stator 2 inlet) measurement position, the Stator 1 wake was in the same position for the low loading (L1) and high loading (L7) conditions, but since the flow rates differ by approximately 20%, the Stator 1 wake impingement condition on Stator 2 is not the same for these two loading conditions near the hub.

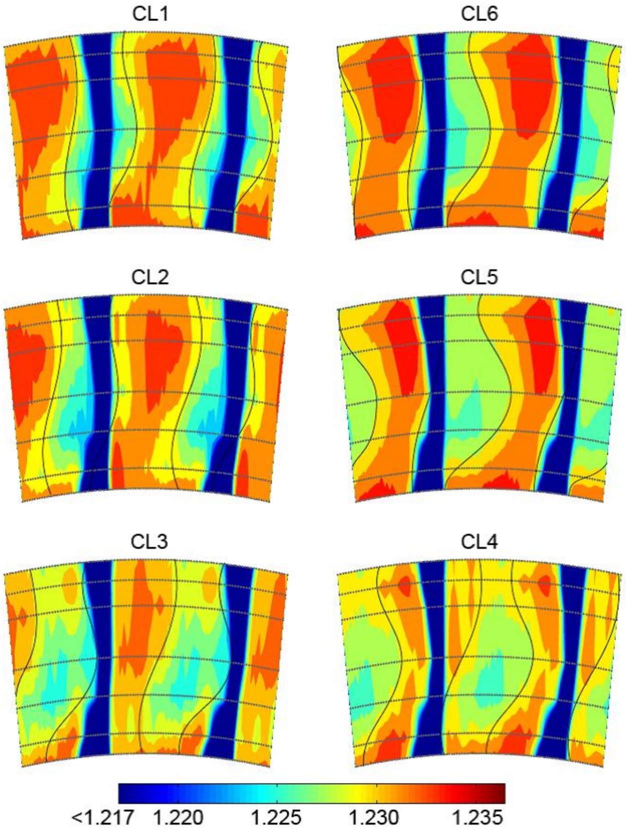

Figure 5.7 Total pressure contours at Stator 2 exit for all six CL at L5

### 5.2.1 Stator 2 Wake Profiles

The clocking effects on Stator 2 are evident in the Stator 2 wake profiles. The high resolution of data acquired in the circumferential direction (every 2%vp) provides good definition of small changes in Stator 2 wake depth and width. In all cases except for the two lowest loading conditions, the pressure side of the Stator 2 wake did not change with clocking. The low loading conditions exhibit some changes in the pressure side of the Stator 2 wake due to negative incidence at those conditions.

Figure 5.8 shows the 12%, 50%, and 88% span wake profiles for low loading (L1) and high loading (L7) operating conditions. At the L1 loading condition, Figure 5.8a, the vane pressure side is affected by vane clocking with small variations in the slope of the pressure side of the wake where it returns to the freestream, and this is most apparent at 12% span. This is contrasted with the high loading condition, where the pressure side of the wake has no variation with vane clocking, Figure 5.8b.

These data also reveal the effect of a skewed Stator 1 wake. For the low loading operating condition, CL1 and CL6 have the highest area-averaged total pressure at Stator 2 exit (smallest wakes), and CL3 has the lowest total pressure (widest wake). These effects are the same all along the span because the Stator 1 wake is not skewed at this loading condition (L1) and loading conditionL2-L5 as shown in Figure 5.4. The differences in Stator 2 wake shape associated with vane clocking are approximately 5%vp in wake width and 7% wake depth at the L1 loading condition. However, at the high loading condition (L7), CL2 has the smallest wake at the tip and CL5 has the largest wake by about 5%vp in wake width. The opposite occurs at the hub where the wake widths differ by more than 10%vp and wake depths differ by 18%. Since the Stator 1 wake is no longer radial at the Stator 2 leading edge for the high loading operating point, the tip and hub of Stator 2 are subject to opposite Stator 1 wake impingement cases. This results in opposite Stator 2 pressure loss trends for the hub and tip regions.

At high loading, the near-hub region of Stator 2 is the most responsive to vane clocking and is highlighted in Figure 5.9 for L5, L7, and L8 for only two clocking configurations, CL2 and CL5. At the L5 loading condition, the CL2 and CL5 wakes are similar to within measurement uncertainty. When increasing loading to the high loading condition, the CL2 wake width grows by about 20%vp, but the CL5 wake grows by only 10%vp. As loading is increased to the peak pressure condition (L8), the amount of wake growth between these two conditions switches: CL2 widens by about 10%vp, and CL5 widens by more than 20%vp, resulting in the largest wake occurring in configuration CL5. This difference in wake size represents a change in the amount of total pressure loss at the Stator 2 hub associated with a modulation of the hub corner separation.

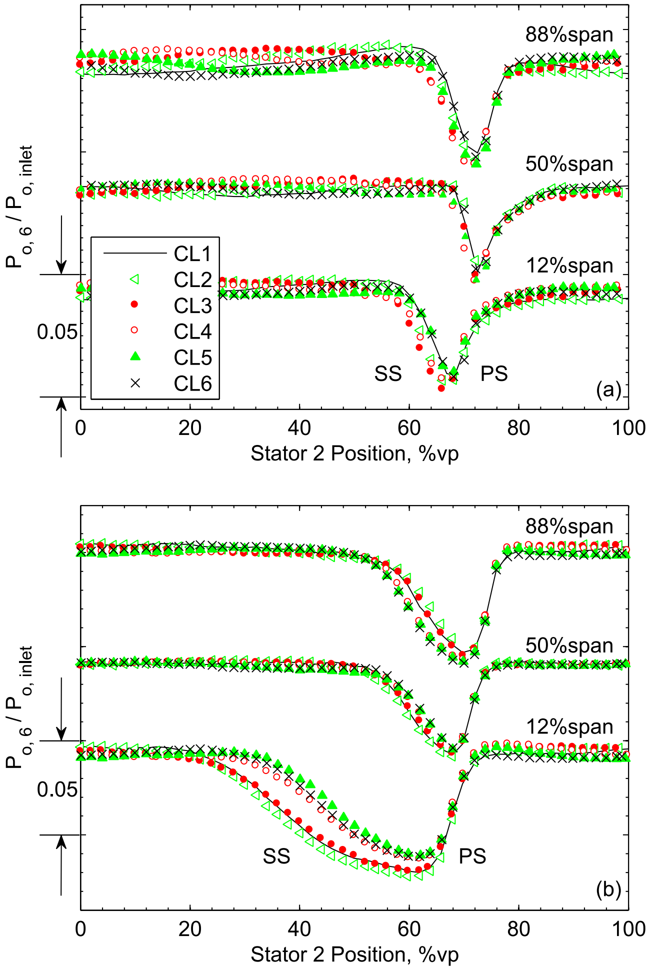

Figure 5.8 Tip, midspan, and hub wake profiles at (a) L1 and (b) L7

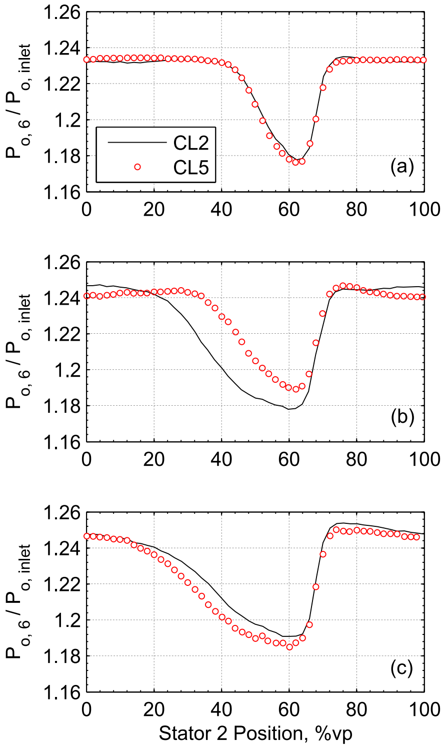

Figure 5.9 Total pressure downstream of Stator 2 at 12%span for loadings: (a) L5 (b) L7 (c) L8

### 5.2.2 Stator 2 Exit Total Pressure Radial Profiles

Radial stagnation pressure profiles were calculated using a pitchwise average of the 50-point circumferential traverse at each spanwise location. Total pressure radial profile shapes are affected by clocking configuration at the high loading conditions, while the lower loadings (L1-L4) and L5 exhibit small local shifts without a major change in the overall profile shape, Figure 5.10. The L2 loading condition exhibits minimal changes in the radial total pressure profile shape with vane clocking. Results at the L5 loading condition show that clocking has an effect on the total pressure at 80% and 88% span, but these are small when compared to the clocking effects at the higher loading conditions.

The changes with vane clocking start to become more significant at the L6 condition which exhibits effects at both the hub and the tip. At the high loading condition L7, half of the clocking configurations (CL4, CL5, and CL6) provide a nearly uniform total pressure profile from hub to tip, while the other configurations (CL1, CL2, and CL3) show a weak hub where the total pressure drops off nearly linearly from mid-span to the hub. The changes in Stator 2 profile shape near the hub at the high loading condition show that configuration CL5 maintains a fuller profile while configuration CL2 undergoes more total pressure loss at the high loading condition. It shows a somewhat bi-modal trend, especially in the hub region.

The vane clocking effects at the hub persist at the two highest loading conditions as well. As the loading condition is increased to L8 and the L9 near stall conditions, the Stator 1 convection shifts as shown in Figure 5.5, and thus, so does the impingement condition which triggers a stronger hub corner separation. The hub corner separation is triggered for configuration CL2 at the L7 high loading condition, but CL5 is resistant to the corner separation until the L8 peak pressure loading condition. At both the L8 and L9 loading conditions, CL5 has more pressure loss at the hub. Also, while clocking position still affects the lower half of the radial profile shape at near stall, the profile shapes are becoming more similar between all six clocking configurations.

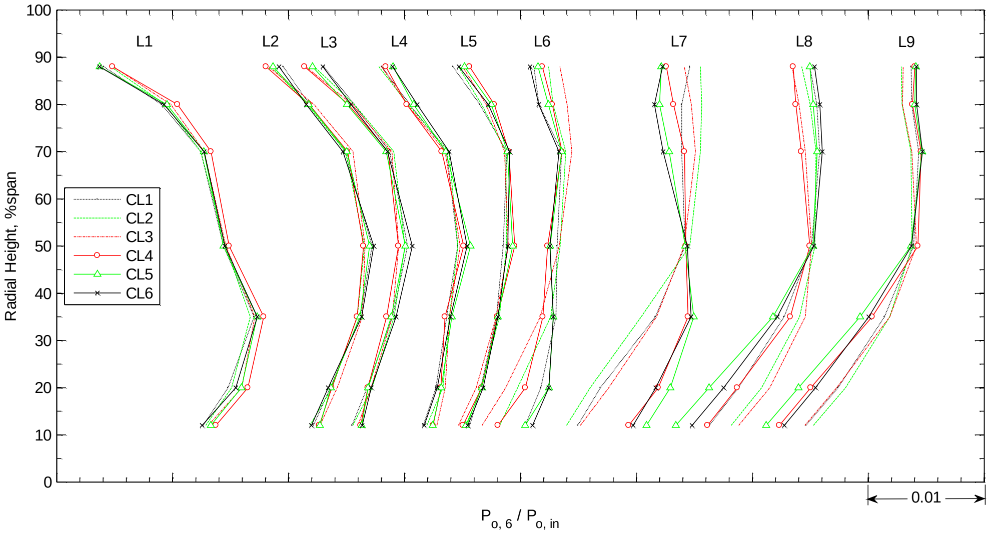

Figure 5.10 Radial profiles at Stator 2 exit for all six clocking configurations at all nine loading conditions

### 5.2.3 Stator 2 Loss

The total pressure data is also used to calculate Stator 2 total pressure loss coefficient ($Y_P$):

$$Y_P = \frac{P_{o,5} - P_{o,6}}{P_{o,5} - P_5}, \tag{5.1}$$

where the difference in total pressure across Stator 2 is non-dimensionalized by the Stator 2 inlet dynamic pressure. In Eq. (5.1), $P_{o,5}$ is the total pressure upstream of Stator 2, $P_5$ is the static pressure upstream of Stator 2, and $P_{o,6}$ is the total pressure downstream of Stator 2. Stator 2 loss coefficients are shown as a function of the clocking configuration, Figure 5.11, to highlight the sinusoidal trend in loss between clocking positions at each spanwise location. All plots are shown on the same scale for loss coefficient. At lower loading conditions (L1-L3) and around the peak efficiency point (L4 and L5), the maximum change in pressure loss between clocking configurations is roughly similar for the hub and the tip. Whereas at the higher loading conditions, the changes are more significant and the losses are greater. At the L7 loading condition, the changes in Stator 2 loss are three times as large at the hub than at the tip, and the trends at the hub are also out-of-phase with the tip region. As loading is increased further toward near stall (L9), the changes in loss due to vane clocking reduce at both the hub and tip by about 40% compared to the values at high loading (L7). The maximum and minimum configurations remain out-of-phase between the hub and tip, but due to changes in Stator 1 wake convection, the maximum and minimum loss configurations are opposite at L8 and L9 compared with the L7 loading condition. In general, vane clocking affected Stator 2 loss evenly along the span for the lower loading conditions (L1-L5), while the higher loading conditions (L6-L9) were most affected in the endwall regions, particularly near the hub.

While the localized vane clocking effects at each spanwise location are interesting, the impact of vane clocking on the overall Stator 2 pressure loss is also relevant. Therefore, these results were area-averaged in the radial direction, to determine a single one-dimensional Stator 2 loss value for each vane clocking configuration and loading condition. Figure 5.12 shows total pressure loss coefficient across Stator 2 as a function of clocking configuration. Relative to the higher loading conditions, the L1-L5 loading conditions are less sensitive to clocking. Despite the opposing trends between the hub and tip for loading conditions L6-L9, there is a strong sinusoidal trend in loss with clocking, which follows the trend observed at the hub. The L7 high loading condition is the most affected by vane clocking, while L8 and L9 decline in the amount of influence clocking has on Stator 2 loss.

Table 5.1 summarizes the results shown in Figure 5.11 and Figure 5.12 by listing the maximum percent difference in Stator 2 total pressure loss between clocking configurations for the tip (88% span), midspan (50% span), and hub (12% span), where each percent is based on the minimum loss clocking configuration for each loading and radial location. The average (Avg.) percent values are based on the minimum loss clocking configuration at each loading as shown in Figure 5.12.

The overall area-averaged change in Stator 2 loss coefficient at the low loading (L1) condition is close to the measurement uncertainty at this loading condition (±6.11%). Whereas, the vane clocking effects at the L7 high loading are more than twice as strong at the hub (48.01% difference in loss coefficient) than at the tip and result in an average difference of 21.77% pressure loss coefficient between clocking configurations. As loading increases toward stall, clocking effects begin to lessen compared to the high loading condition.

Table 5.1 Summary of Stator 2 loss coefficient changes in terms of percent difference

| $\Delta Y_P / Y_{p,\min}$ | L1 | L2 | L3 | L4 | L5 | L6 | L7 | L8 | L9 |
|---|---|---|---|---|---|---|---|---|---|
| Tip | 9.86 | 6.13 | 7.16 | 3.87 | 9.56 | 13.33 | 21.92 | 9.93 | 9.24 |
| Mid | 19.68 | 18.01 | 16.32 | 21.48 | 13.05 | 9.71 | 20.93 | 1.94 | 3.46 |
| Hub | 7.82 | 11.49 | 14.42 | 20.58 | 9.32 | 37.8 | 48.01 | 24.61 | 16.03 |
| Avg. | 5.90 | 6.62 | 5.82 | 5.43 | 4.80 | 9.64 | 21.77 | 9.61 | 6.77 |

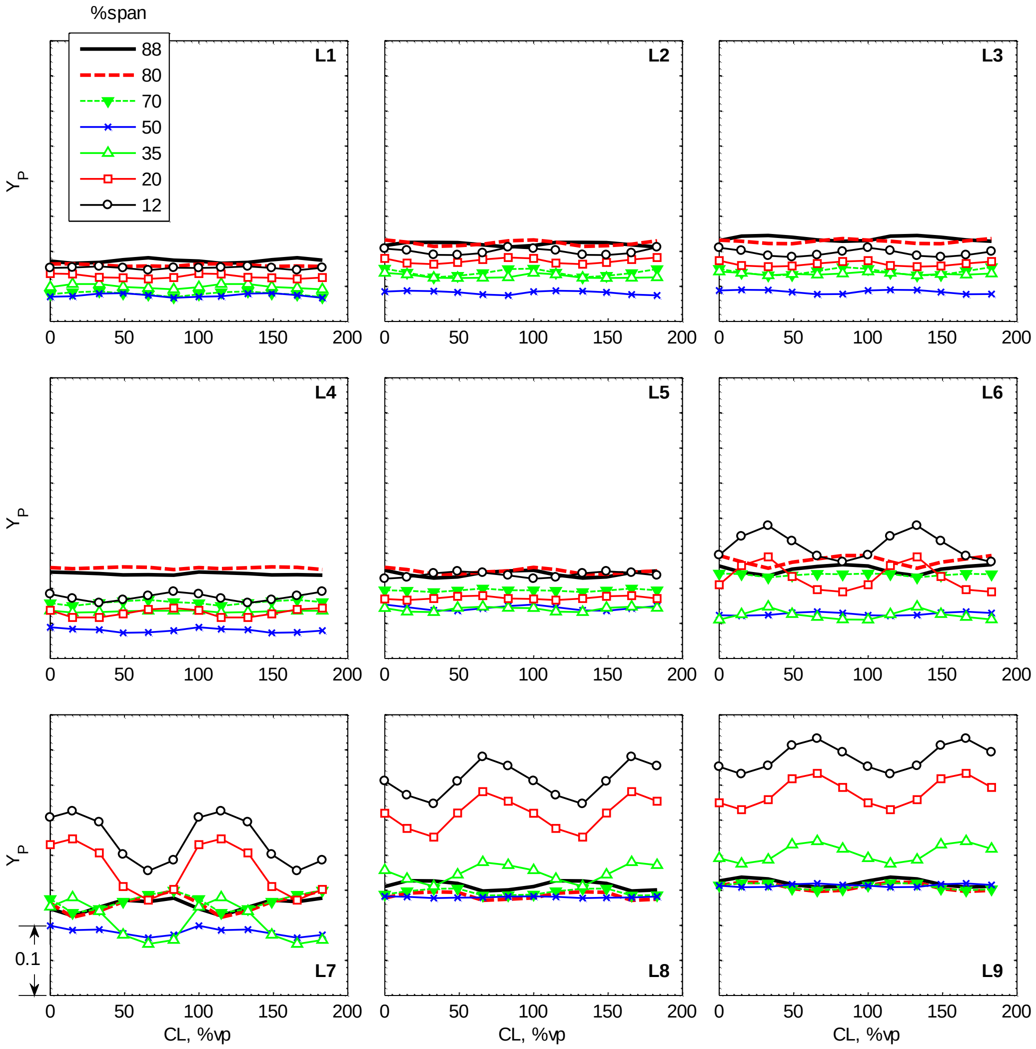

Figure 5.11 Changes in Stator 2 loss with vane clocking at all nine loading conditions

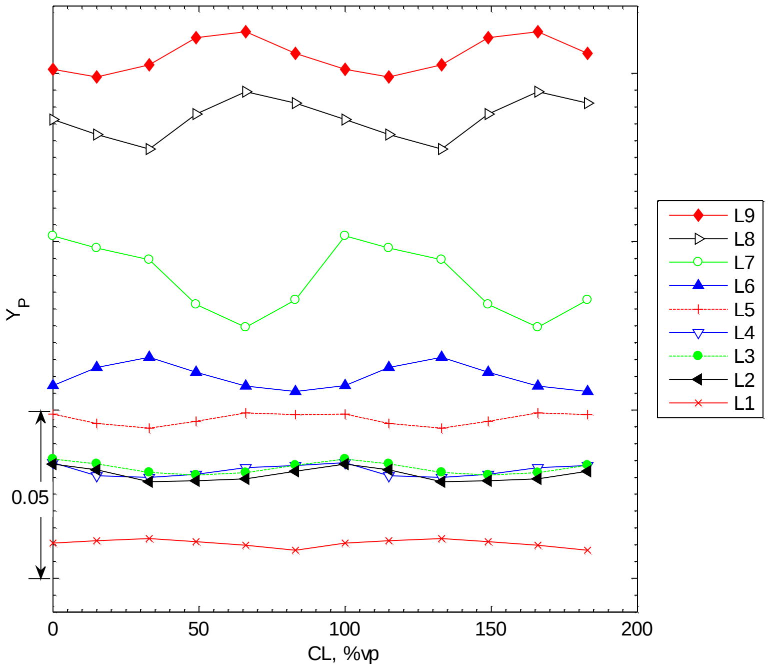

Figure 5.12 1D Stator 2 loss for all nine loading conditions

### 5.2.4 Flow Visualization of Stator 2 Corner Separations

The results from total pressure traverses downstream of Stator 2 indicate vane clocking is likely influencing the corner separations, especially near the hub. Flow visualization has been shown to highlight vane corner separations well in Chapter 4, and therefore was used to confirm the flow physics driving this change in vane wake and radial profile shapes due to vane clocking. For flow visualization the number of clocking configurations must be limited for feasibility. Therefore, the maximum and minimum total pressure loss clocking configurations were the focus for the flow visualization element of this research. This is a case where two different colored paints were used in the same run to visualize the flow patterns for two clocking configurations. Orange fluorescing paint was used for configuration one clocking configuration and injected at the AIP at circumferential locations A and B (refer to Figure 2.6), while blue fluorescing paint was used for the second clocking configuration and injected at circumferential locations B and C. This allowed each clocking configuration to be characterized with vanes visualized by only one color and a few vanes with overlapping colors to directly compare to the flow fields associated with the two clocking configurations.

The Stator 2 steady total pressure loss vane clocking trends presented this chapter were used to select the loading conditions and determine the maximum and minimum clocking configurations. A 21.8% difference in total pressure loss coefficient was observed between CL2 (max loss) and CL5 (min loss) at the high loading configuration, L7. This effect declined as loading was increased toward stall and was much less at the lower loss conditions near peak efficiency. Figure 5.13 shows flow visualization images of the Stator 2 suction side for two clocking configurations at the high loading (L7) and near stall (L9). Accompanying the images are the radial total pressure profiles shown previously.

At the L7 high loading condition, the flow visualization reveals that vane clocking modulates the size of the Stator 2 corner separations, Figure 5.13a. This finding supports the observations made based on the radial profiles downstream of Stator 2 in Figure 5.13b. CL2 has a larger hub corner separation and more total pressure loss at the hub, while CL5 has hub and tip corner separations of similar size and nearly radial total pressure profile. The change in location of the Stator 1 wake impingement on the Stator 2 leading edge causes the boundary layer to separate in different patterns.

The near stall case is shown in the bottom of Figure 5.13c-d. The steady performance results showed the difference in loss with vane clocking lessen between high loading (L7) and near stall (L9), though strong trends were still present at the hub. These trends are shown in the radial total pressure profiles in Figure 5.13d where the maximum and minimum loss clocking configurations were CL5 and CL2 respectively. As could be expected at near stall loading, the boundary layers have large separated flow regions. The other measurements taken in the stator passage in this study (surface pressures and wall shear stress presented in a later chapter) could not obtain data at this condition, due to sensor measurement limitations. Therefore, flow visualization provides insight that could not otherwise be verified by data acquired within vanes. Unfortunately, the differences in boundary layer separations between CL2 and CL5 are not significant enough to be seen in the flow visualization.

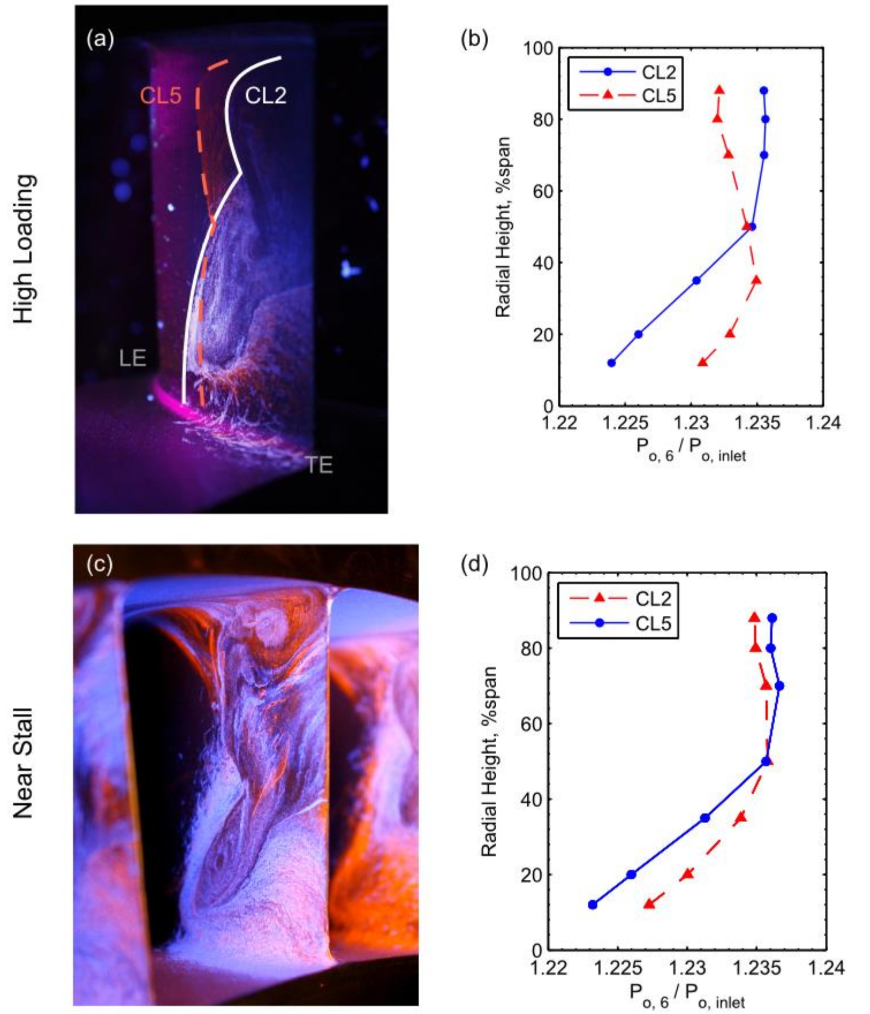

Figure 5.13 Vane clocking effects on Stator 2 boundary layer separation for the maximum and minimum loss clocking configurations at (a-b) L7 high loading and (c-d) L9 near stall conditions shown with radial total pressure profiles downstream S2

### 5.2.5 Overall Vane Clocking Trends

The steady vane clocking dataset presented in this chapter is the largest in the open literature, consisting of six vane clocking configurations at nine loading conditions. Figure 5.14 summarizes the measured difference in Stator 2 loss between the maximum and minimum vane clocking configurations at the nine loading conditions with the 100%

corrected speedline. There is a clear increase in vane clocking effectiveness beginning somewhere after the L5 loading condition. The clocking effects increase between L5 and L7, which is verified by L6. After L7, the clocking effects decline. These trends generally support the previous vane clocking studies conducted in this compressor, where vane clocking effects were strongest at a high loading condition (Key et al., 2010), but no measurable changes in stall margin is associated with vane clocking (Smith and Key, 2013). There is an inconsistency in vane clocking trends near the peak efficiency loading condition. Both Key et al. (2010) and Smith (2007) reported measurable vane clocking effects near this loading condition. Not only did these studies observe differences between clocking configurations in the upper span (near tip) region, but they also had measurable 1-D trends at this loading condition. In contrast, the vane clocking trends presented for the present research at this operating condition and at multiple conditions near peak efficiency exhibited only small local changes shifts with vane clocking and the 1D values were on the order of the measurement uncertainty. Section 3.4 highlighted the importance of inlet temperature to thermal growth changes in the compressor, resulting in different operating rotor tip clearances. This affected the overall pressure rise capability of the compressor as well as the interstage flow physics, particularly in the tip region. Those findings motivate considering the inlet temperature for these steady vane clocking data both to ensure consistency was maintained in this study and how it compares with previous studies.

Figure 5.15 shows the average inlet temperature for each clocking configuration traverse at all nine loading condition plotted as a function of mass flow rate. The average inlet temperature of the six clocking configurations is also shown for each loading. Mass flow rate is used as a representation of the loading condition because the inlet temperature, and thus thermal grown, will alter the compressor TPR. For this study, the L2 loading condition had the largest change in inlet total temperature over the course of the 12 hour test, as shown in Figure 5.15. The change occurred gradually through the test where CL1 began at 15°F and CL6 averaged 35°F. This difference of 20°F could potentially contribute to a change in rotor tip clearance of $1.4\text{x}10^{-3}$in and is likely not a significant concern. Furthermore, this would mean CL1 and CL6 should be the most different at the L2 loading condition. The radial profiles shown in Figure 5.10 show that the CL1 and CL6 average total pressure profiles are the most similar. Therefore, the inlet total temperature between clocking configurations and the nine loading conditions is not contributing the vane clocking trends observed in this chapter.

On the other hand, there is a significant difference in inlet total temperature between this study and the previous vane clocking studies completed in the same compressor. Figure 5.16 shows the average inlet temperature for the nine loading conditions in the present study compared with the average inlet temperatures for each of the loading conditions studied by Key et al. (2010) and Smith (2011). Both of these other studies were conducted under much warmer conditions (40-50°F warmer). It is possible that these studies were carried out at a significantly different rotor tip clearance, and that could be changing the vane clocking behavior near the peak efficiency point. In Chapter 6, the rotor tip leakage flow is shown to be connected to vane clocking. Susquently, these inlet temperature considerations are important to recall when trying to compare datasets.

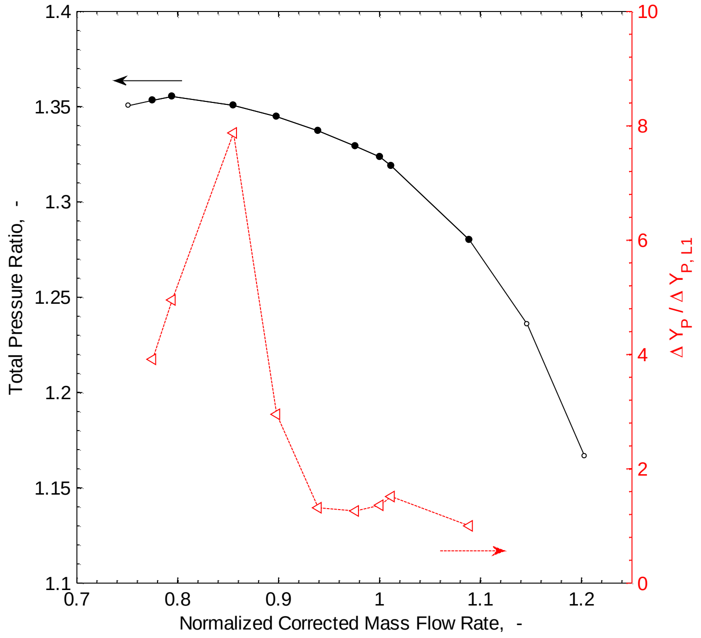

Figure 5.14 Difference in overall Stator 2 loss between clocking configurations along 100%Nc

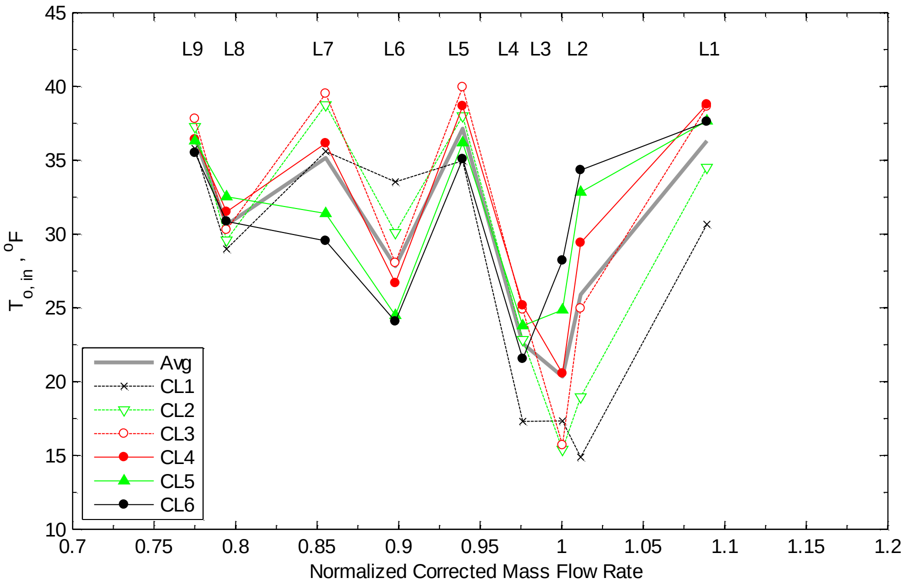

Figure 5.15 Inlet total temperature for each clocking configuration of present study

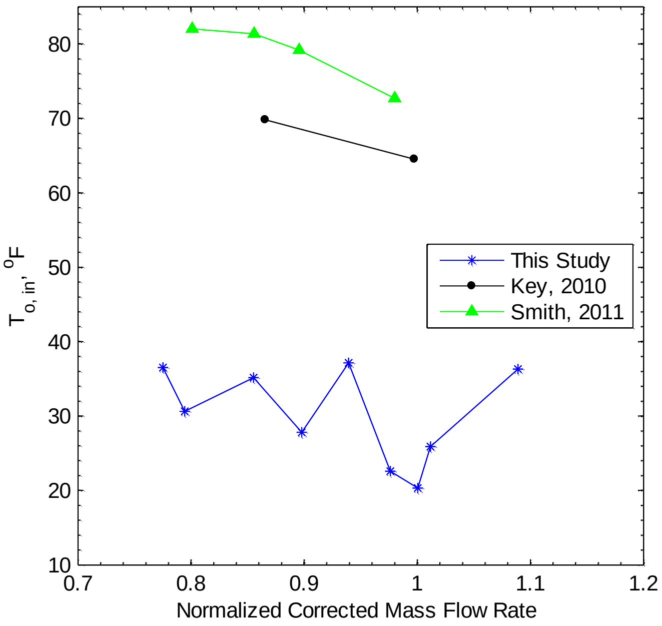

Figure 5.16 Average inlet total temperature for various vane clocking studies in the Purdue three-stage compressor as a function of mass flow rate

# CHAPTER 6. ROTOR TIP LEAKAGE FLOW EFFECTS ON VANE CLOCKING

The effects of vane clocking on steady compressor performance from Chapter 5 suggest that the position of Stator 1 with respect to Stator 2 can significantly alter the Stator 2 corner separations. Furthermore, the literature suggests these effects can be attributed to unsteady surface flows, either boundary layer transition or pressure unsteadiness. Prior to investigating these flows, the unsteadiness of the Stator 2 inlet flow should be characterized to better understand how vane clocking is affecting the Stator 2 inlet conditions. This chapter presents detailed radial traverses of unsteady total pressure at the Rotor 2 exit / Stator 2 inlet and consists of two sections. The first discusses a dataset acquired at part-speed, 74%$N_c$, with 20-point circumferential vane traverses at two loading conditions: nominal loading and high loading. These data were acquired for an aeromechanics study to understand the aerodynamic forcing on the vane, and thus part speed operation near resonance was more appropriate than 100%$N_c$ operation. The part speed flow physics are still relevant to full speed operation and thus motived additional data acquisition. The second part of this chapter includes traverses at 100%$N_c$ for several loading conditions at six clocking positions. Both of these datasets are used to illuminate the rotor tip leakage flow and explore the modulation of the tip leakage vortex as Rotor 2 passes through the Stator 1 wake.

## 6.1 Influence of the Tip Leakage Flow

Near the endwall, the rotor tip leakage vortex will provide an additional source of unsteadiness to the downstream vane row. A detailed radial traverse at 20 pitchwise positions was performed at 74%$N_c$ with a high-frequency response pressure transducer embedded in a Kiel-head probe. These measurements were acquired every 2% span from 100% to 78% span, with a coarser distribution to the hub. The unsteady total pressure measurements are presented in terms of root mean square (RMS) pressure coefficient, $C_{p,}$

$$C_{P,RMS} = \frac{\sqrt{\frac{1}{N_{EA}}\Sigma(P_{o,i}-P_{o,EA})^2}}{\frac{1}{2}\rho U_t^{\,2}}\,, \tag{6.1}$$

where $P_{o,i}$ is the instantaneous total pressure, and $P_{o,EA}$ is the ensemble-averaged total pressure. The pressure RMS is normalized by the dynamic pressure at the inlet, where $\rho$ is the inlet density and $U_t$ is the rotor tip speed.

Data at two (of the twenty) pitchwise locations at high loading are shown in Figure 6.1: 40%vp (top) and 90%vp (bottom). These pitchwise locations are half a vane passage offset from one another. RMS contours of pressure coefficient are shown for a full rotor revolution (33 Rotor 2 blade passings). There is a solid black line at 80% span to assist in comparison with other data at this location. High RMS indicates regions consisting of large unsteadiness, which is not locked to the blade-passing event, such as regions which are shedding at frequencies different from the blade passing event (flow within a wake or tip leakage flows). The vertical strips of approximately 0.003-0.004 RMS are the Rotor 2 wakes. The highest levels of RMS occur in a larger region near the tip and represent the Rotor 2 tip leakage flow. At 40%vp, the tip leakage vortex is contained entirely above 80% span, but at 90%vp, the tip leakage vortex extends below 80% span and is stronger (higher RMS).

The Fourier transforms of these data at 80% span are shown in the graphs to the right of the contours in Figure 6.1 and are markedly different for the two circumferential locations. The magnitude of the Rotor 2 blade pass frequency (33/rev) is twice as large at 40%vp compared to 90%vp. Also, the magnitude of the Rotor 1 blade pass frequency (36/rev) is three times larger at 40%vp compared to 90%vp. The spectrum at 90%vp is characterized by larger magnitudes in the higher frequencies. The second harmonic of Rotor 2 blade pass frequency (66/rev) is almost twice as strong as the fundamental frequency, and the third harmonic is approximately the same magnitude. The presence of the tip leakage vortex in the 80% span region for the 90%vp location provides an additional disturbance for every rotor blade passing event, and this distributes more energy into the higher frequencies. These observations indicate that the time averaged radial pressure profile could be significantly different depending on where the measurements are acquired in the pitchwise direction.

A mean passage is calculated from the total pressure RMS data acquired at each pitchwise location to provide a characterization of the mean tip leakage flow over a blade pass period at each pitchwise position. This is done by splitting the ensemble-averaged revolution of data into 33 segments, one for each Rotor 2 blade passage. The 33 segments are then ensemble-averaged to produce a mean passage. The differences associated with these 20 mean wakes are attributed to the effects of the pitchwise position. These results are shown in Figure 6.2 where the 20 pitchwise positions are presented in a clockwise manner to highlight the periodicity of the flow, with 0%vp in the upper left corner.

The modulation of the shape of the rotor tip leakage vortex is noticeable. Not only are the tip leakage flows at 40%vp and 90%vp different in size and location (penetration into the passage), but the shapes are also different. These changes in the tip leakage flow also have an effect on the lower half of the blade passage. When the tip leakage vortex is larger, as shown at 90%vp, there is more blockage at the tip and the fluid shifts toward the hub. This will locally increase the mass flow rate in the lower part of the span and unload that region resulting in a reduction of the radial extent of the region of large unsteadiness near the hub. At 90%vp, the high hub RMS reaches approximately 40% span, but when the tip leakage vortex is smaller at 40%vp, the large RMS region extends up to 50% span.

Figure 6.3 highlights the bounds of the tip leakage vortex modulation at 40%vp and 90%vp. The total pressure RMS contours are shown along the bottom, as presented in the previous figures. The RMS total pressure signal at 80% span is shown along the top. At 40%vp where the Rotor 2 tip leakage vortex is contained above 80% span, there is no distinct secondary peak in the 80% span averages. The pressure side (lower values of %bp) of the rotor wake is wide and the RMS pressure coefficient curve features two peaks, one on each side of the rotor wake. The trends at 90%vp are quite different since the tip leakage vortex is influencing the measurements. The RMS pressure coefficient data show higher unsteadiness in the tip leakage flow than in the wake region.

The changes in the size and shape of the tip leakage vortex as a function of pitchwise position can be explained by the interaction between Rotor 2 and the Stator 1 wake. The absolute velocity deficit in the Stator 1 wake provides an increase in Rotor 2 incidence. As incidence increases, the rotor blade loading increases, and the axial location of the peak loading on the rotor also moves upstream. The location of the peak loading along the rotor blade influences the rotor tip leakage flow, including the location at where it forms and its subsequent trajectory. This occurs in a particular circumferential region where the rotor chops the stator wake. Therefore, there is a corresponding circumferential position downstream of the rotor which will contain a tip leakage vortex with a different character as compared to that when the Rotor 2 leading edge is not in the Stator 1 wake. One of these circumferential locations downstream of Rotor 2 could be the Stator 2 leading edge, which two clocking configurations could have different Stator 2 inlet flow fields.

Figure 6.4 demonstrates the interaction between the Stator 1 wake and the Rotor 2 tip leakage vortex with an illustration of two different instances in time. Figure 6.4a shows Rotor 2 when its leading edge is between Stator 1 wakes and an example of the rotor inlet velocity triangle. The tip leakage flow in this case ends up in the middle of the pitchwise measurement positions downstream of Rotor 2. In Figure 6.4b, the leading edge of Rotor 2 is in the Stator 1 wake, where the absolute velocity, v, is smaller and the relative flow angle larger. The formation of the tip leakage flow occurs closer to the leading edge, the trajectory has a steeper angle, and the resulting vortex is larger. Different pitchwise measurement positions downstream of Rotor 2 will capture the tip leakage vortex development for this scenario.

To illuminate this effect, flow visualization results (discussed previously in Chapter 4) are shown in Figure 6.5. The trailing edge of Stator 1 and the leading edge of Stator 2 are shown with airfoils sketched in the proper geometric locations. The Stator 1 wake path is visible downstream of the vane trailing edge. When the wake reaches the

Rotor 2 leading edge, its path deviates from the stator exit flow angle and begins to follow the rotor rotation until it meets the tip leakage jet. The location of the inception of the tip leakage flow is labeled as the location where the thicker circumferential line of paint on the casing is located. The thick line of paint accumulation from the leakage flow shifts upstream in the vicinity of the Stator 1 wakes. This is in agreement with the sketches shown in Figure 6.4: when Rotor 2 passes through the Stator 1 wake, the blade loading increases, peak loading shifts forward, and a larger tip leakage vortex is formed.

Similar trends regarding the modulation of the rotor tip leakage vortex size and position were observed at the nominal loading condition, but the effects at high loading are stronger due to the larger Stator 1 wake and Rotor 2 tip leakage flows. The change in radial extent of the tip leakage vortex with pitchwise position is twice as large at high loading than at nominal loading. The wider, deeper Stator 1 wake at high loading increases the circumferential extent of the high-incidence region for Rotor 2.

These results identify a blade row interaction which is likely connected with vane clocking. The schematic in Figure 6.4 represents two different time instances in the rotor rotation past a vane row for a single clocking configuration. For the example illustrated, not only is the interaction in Figure 6.4a observed in the middle of the pitchwise positions, but the leakage flow is not interacting with the Stator 2 leading edge. In the second time instance, Figure 6.4b, the Rotor 2 tip leakage flow is interacting with the Stator 2 leading edge. For the clocking configuration shown, inlet conditions at the Stator 2 leading edge are formed when Rotor 2 interacts with the Stator 1 wake. If the clocking configuration was changed by half a vane passage, then Stator 2 inlet flow would consist of the rotor exit flow filed that develops when Rotor 2 is between Stator 1 wakes. Like the discussion at the end of Chapter 5, these observations also suggest a connection between the rotor tip flows and vane clocking. And these observations motivate a detailed investigation of unsteady Rotor 2 exit tip leakage flows for different clocking configurations at 100%$N_c$, which is presented in the following section.

Furthermore, these results motivate a need to acquire pitchwise traverses of flow field data even for data downstream a rotor. When evaluating performance trends, the pitchwise average will ensure proper representation of the average flow behavior, while from the aeromechanical standpoint, the pitchwise data provides bounds to the possible aerodynamic forcing which could occur.

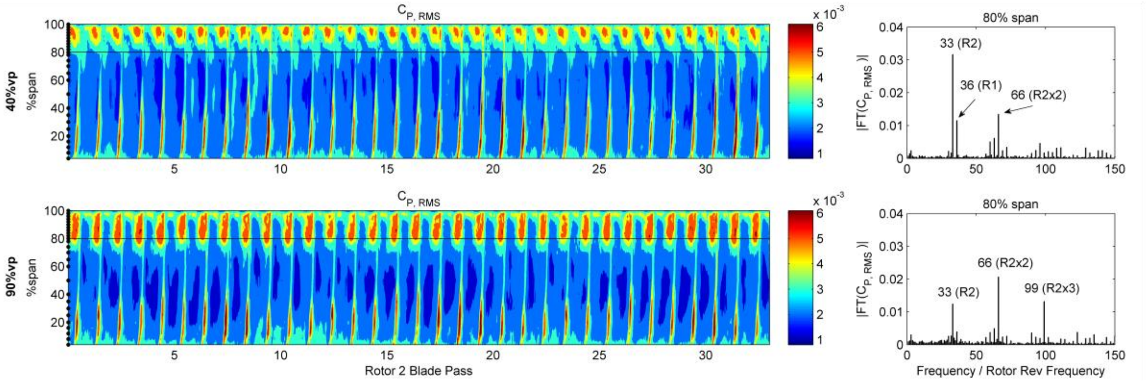

Figure 6.1 Pressure coefficient RMS contours (left) and Fourier transform of RMS at 80%span (right) for 40% (top) and 90%vp (bottom) at the high loading condition

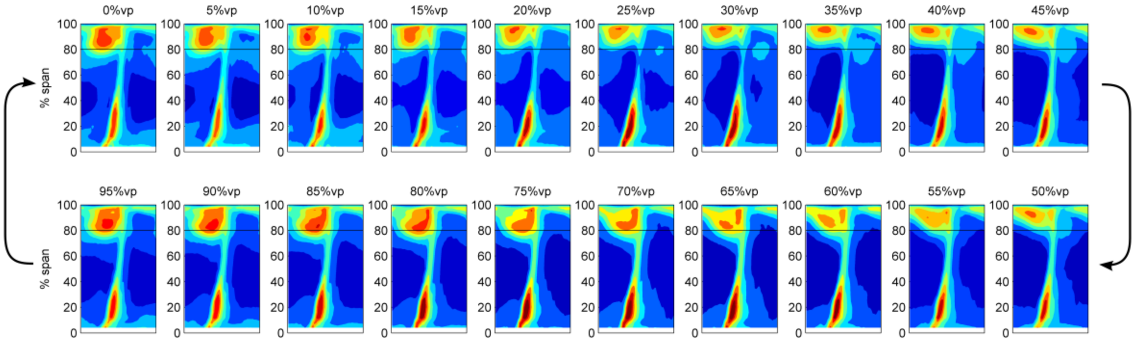

Figure 6.2 Average rotor exit flow field, in terms of coefficient of pressure RMS, at each circumferential location across the vane passage (clockwise) at high loading

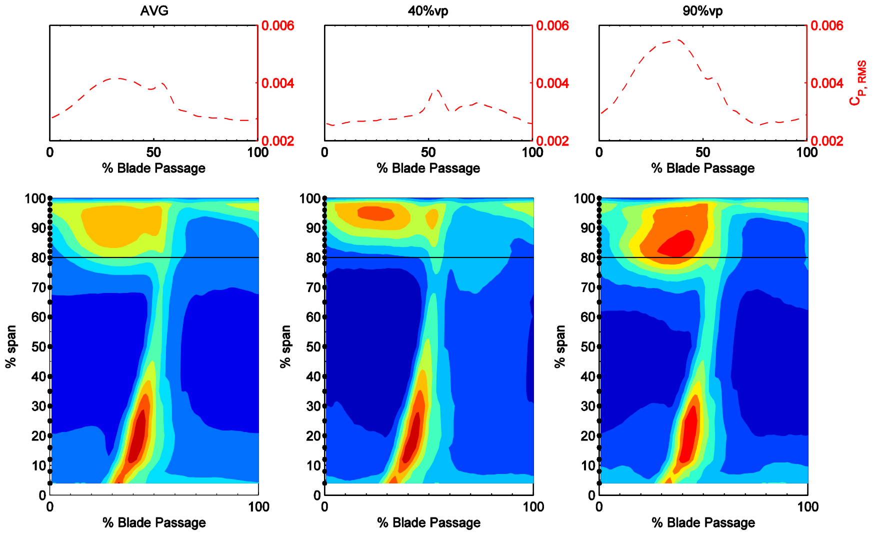

Figure 6.3 Contours of coefficient of pressure RMS (bottom) at high loading for the average passage (left), 40%vp (middle), and 90%vp (right)

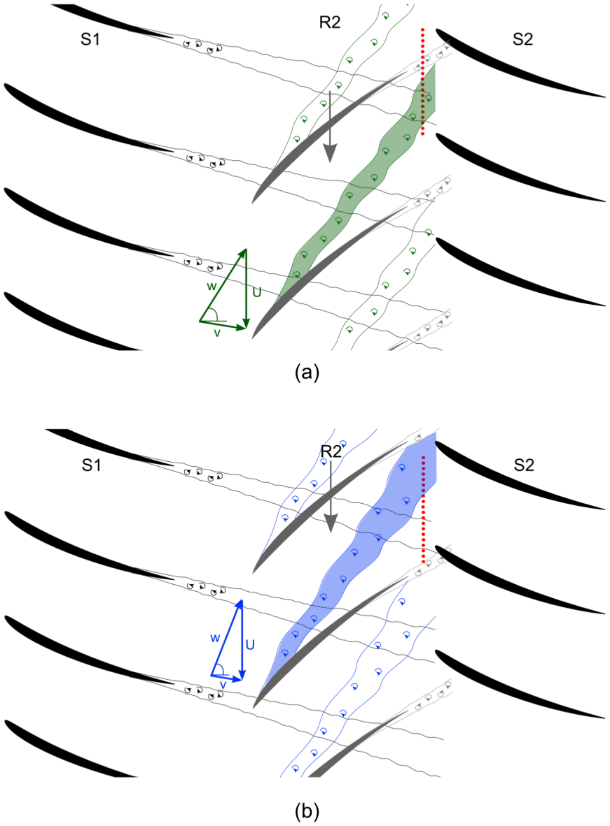

Figure 6.4 Schematic of interaction between Stator 1 wake and Rotor 2 tip leakage vortex (a) R2 passing the middle of the S1 passage (b) R2 passing through the S1 wake

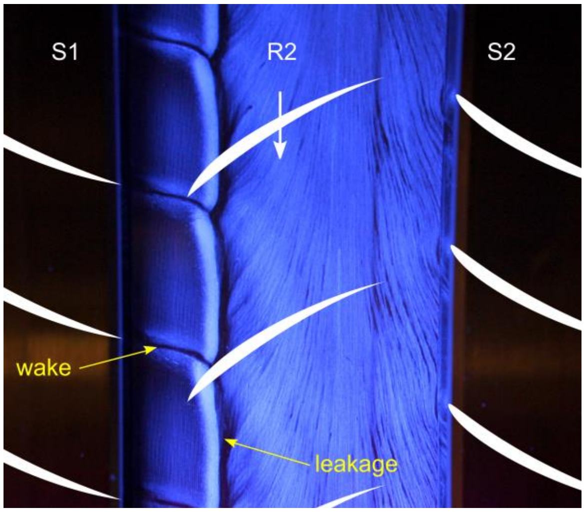

Figure 6.5 Flow visualization on the casing endwall over Rotor 2

## 6.2 Change in Rotor 2 Leakage Flow with Clocking Configuration

The interaction between the Stator 1 wake and Rotor 2 tip leakage flow influences vane clocking by altering the inlet flow field to the downstream stator (Stator 2). To investigate the effects of the Rotor 2 leakage flow changes at the Stator 2 inlet with different vane clocking configurations detailed radial traverses with an unsteady total pressure probe were completed. Instead of full vane traverses where all four vane rows are traversed in a given configuration (like those completed in the previous section), only the IGV and Stator 1 were traversed. In this case, the effects of the Stator 2 potential field are not important and the probe mimics the Stator 2 leading edge. With the probe and Stator 2 fixed, traversing the IGV and Stator 1 will illuminate the effects of vane clocking on the flow as seen by a single position in the vane pitch, such as the Stator 2 leading edge. These traverses consisted of 12 clocking configuration, including the six presented in Chapter 5 at five loading conditions: L1, L3, L6, L7, and L8. The RMS of the unsteady total pressure signal was calculated in the same way as the previous section in terms of a pressure coefficient, Eq. 6.1.

Contours of RMS for two of the twelve clocking configurations are shown for lower loading conditions (L1 and L3) in Figure 6.6 and Figure 6.7, respectively. And four of the twelve clocking configurations are shown for higher loading conditions (L6, L7, and L8) in Figure 6.8 – Figure 6.10, respectively. Each set of clocking configurations was chosen to highlight the extent of clocking effects at that loading condition. The contour scales are held constant between all figures where red is high RMS with a limit on 0.0075 and blue is low RMS with a limit of 0.003.

At the low loading condition, L1, and the peak efficiency condition, L3, the changes in Rotor 2 tip leakage flow signature between clocking configurations are small. For the L1 loading condition (Figure 6.6), the shape of the tip leakage flow blockage region remains similar. The differences reside in the strength of the unsteadiness and less than a 5%span change in radial depth. There are no other distinct differences in unsteadiness in the blade passage. Closer to design point operation, the peak efficiency conditions has slightly larger changes in the Rotor 2 exit flow field with clocking configuration. Figure 6.7 shows clocking configurations CL3 and CL6 for the L3, peak efficiency operating point. The difference in radial extent of the tip leakage flow is just over 5%span and the shapes differ more. For CL6, the region of peak RMS in the tip is very close to the casing, while for CL3 the peak RMS is lower in the passage and the overall shape is more round. There are also notable differences in the Rotor 2 wake unsteadiness at the hub. Clocking configuration CL6 has higher unsteadiness reaching closer to midspan than the CL3 hub wake. Furthermore, these clocking configuration trends are nearly opposite of those from low loading (L1). The larger rotor tip leakage blockage regions occurs in clocking configurations that are nearly half out of phase from one another between L1 and L3.

For three of the higher loading conditions (L6, L7, L8) in Figure 6.8 through Figure 6.10, the changes in the Rotor 2 tip flows are more significant, and therefore contours of pressure coefficient RMS are shown for four clocking configurations, CL2, CL3.5, CL5, CL6.5, where CL3.5 is half way between CL3 and CL4, and similarly, CL6.5 is half way between CL6 and CL1. Figure 6.8 shows RMS contours for the L6 loading condition. Each of the four clocking configurations produces a different Rotor 2 exit flow field. In terms of the tip leakage flow, CL3.5 and CL6.5 represent the bounds of the size high unsteadiness, blockage region where configuration CL3.5 extends at least 10%span lower into the passage than CL6. Configuration CL3.5 with the largest rotor tip leakage flow also has the strongest unsteadiness. The other two clocking configurations are also interesting partly because of the change in location and shape of the tip leakage flow. For CL3.5 and CL5, the lowest extent of the leakage flow is in the middle of the blade passage, as opposed to CL2 and CL6.5 which are located immediately adjacent to the rotor wake. These other clocking configurations (CL2 and CL5) also exhibit very different behavior in the rotor hub wake. Although, clocking configurations CL3.5 and CL6, have vastly different tip flows, the hub regions of the rotor wake are quite similar, especially compared to those of CL2 and CL5 with high unsteadiness. The RMS values in the CL2 and CL5 rotor wakes at the hub are larger than the RMS in the tip leakage flow. In Chapter 5, loading condition L6 was the first loading condition where significant changes with vane clocking were observed, including a measurable change in average Stator 2 total pressure loss. Similar to the steady total pressure data at Rotor 2 exit presented in Chapter 5, the flow physics overserved in these clocking configurations cannot be directly correlated to the trends with Stator 2 total pressure loss. The unsteady total pressure probe remained in the same circumferential location positioned half way between the Rotor 2 trailing edge and the Stator 2 leading edge for all cases. As the loading condition changes, the flow velocities and flow angles change which affect the flow convection. Therefore, the probe may measure the conditions which convect to the Stator 2 leading edge for one loading condition, but cannot do so for all loading conditions at a fixed upstream position.

The high loading condition which exhibited the largest total pressure loss changes with vane clocking was L7, and Figure 6.9 highlights the changes in Rotor 2 exit coefficient of press unsteadiness for four clocking configurations. The rotor leakage flow trends with clocking are similar to those at the previous loading condition, L6, but slightly shifted due to changes in flow angles and velocities between conditions. Here the CL2 and CL5 clocking configurations represent the largest and smallest rotor tip leakage blockage cases. Again the larger blockage extends at least 10%span further down in to the passage than the smaller blockage, and the larger blockage encompasses a larger portion of the passage in the circumferential direction with a more round shape. The behavior at the hub is also interesting. Instead of shifting with the tip flow behavior, the clocking configurations with the high RMS in the hub region of the rotor wake remain the same as those in the previous loading (L6). In this case, the rotor wake with high RMS in CL2 is wider at the hub than in CL5.

As loading is increased further to L8, the changes in the Rotor 2 exit flow field with clocking are still apparent, shown in Figure 6.10. The rotor tip leakage blockage regions have shifted between clocking configurations with the change in loading due to different Stator 1 wake convection. The largest and smallest Rotor 2 tip leakage flow patterns develop in the same clocking configurations as in the L7 loading condition. With the increase in loading, the large blockage in CL2 has slightly stronger RMS and is larger in size than the previous condition. Also the smallest blockage case (CL5) extends further into the blade passage than the L7 condition. The rotor wake hub regions have the strong RMS values in both the CL2 and CL5 conditions, similar to the observation at L7. Additionally, the difference between the largest and smallest rotor tip leakage flow clocking configurations is at this loading condition (L8) than the previous condition (L7). This matches the clocking trends observed in the Stator 2 total pressure loss data in which the effects of vane clocking grew with increased loading until L7 after which the changes with vane clocking decreased closer to the stall line.

These contours of pressure coefficient RMS can also be used to identify the Stator 1 wake position between the various clocking configurations. Figure 6.11 shows 12 clocking configurations in a clockwise manner of pressure coefficient RMS at the L8 loading condition. The contour levels are shown in grayscale, with white being high RMS and black representing low RMS, and the colorbar has been skewed to highlight the variations in the mid-passage flow. A red dashed line has been sketched in each figure approximating the location of the Stator 1 wake. One particularly interesting trend in these data is that the movement and shape change of the Rotor 2 tip leakage flow appears to follow the Stator 1 wake. For example, in CL1, the radially lowest portion of the blockage region is again the rotor wake and the stator wake coincides with the rotor wake. At CL2, the lowest point in the blockage region has separated from the rotor wake flow and aligns with the stator wake. This point continues to walk with the Stator 1 wake, where by CL4, they are each about half a blade passage away from the rotor wake. This indicates that the change in the rotor tip leakage flow behavior may be a combination of effects from its interaction with the Stator 1 wake. The rotor leakage flow could both be developing different as the rotor passing through the stator wake, but also the trajectory of the resulting leakage flow could be influenced by the stator wake through the passage. Measurements from within the rotor passage would be required to validate this.

Finally, these unsteady total pressure data are time averaged and normalized by the compressor inlet total pressure to show radial profiles downstream of Rotor 2. While the contour plots have indicated the level of unsteadiness Stator 2 experiences in different clocking configurations, average total pressure profiles provide an indication of the loading distribution at that the Stator 2 inlet. Radial total pressure profiles are shown for five loading conditions (L1, L3, L6, L7, and L8) in Figure 6.12 through Figure 6.16. The low loading condition and the peak efficiency condition have small local changes between vane clocking configurations. For example, L3, shown in Figure 6.13, has some distinct differences near the tip at 85-90%span. But at the higher loading conditions, vane clocking has a more dramatic effect on the profile shape. These differences occur across the entire span but are particularly strong at the hub.

These data indicate that vane clocking greatly alters the in downstream stator’s inlet flow field via altering the interactions between the upstream stator and the embedded rotor. The effectiveness of vane clocking to change the flow field shown with data at the Stator 2 inlet at various loading conditions correspond well with the steady vane clocking results at the Stator 2 exit. The lower loading conditions were less affected while the higher loading conditions experienced larger change with vane clocking. These data motivate further details regarding how Stator 2 responds to different levels of unsteadiness and blade row interactions with vane clocking, especially in the tip region, which will be shown with data from within the vane passage in the following chapter.

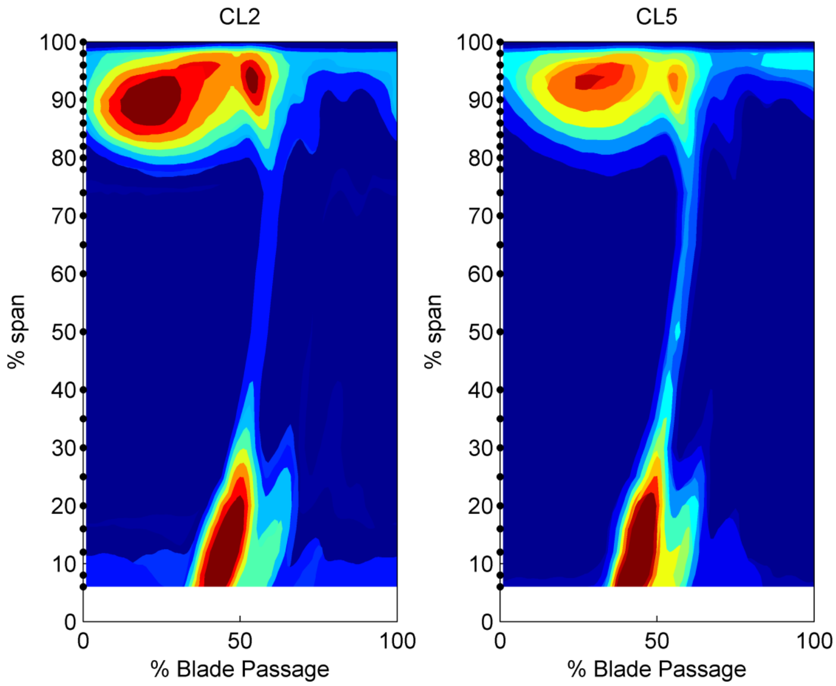

Figure 6.6 Contours of coefficient of pressure RMS at L1 for CL2 and CL5

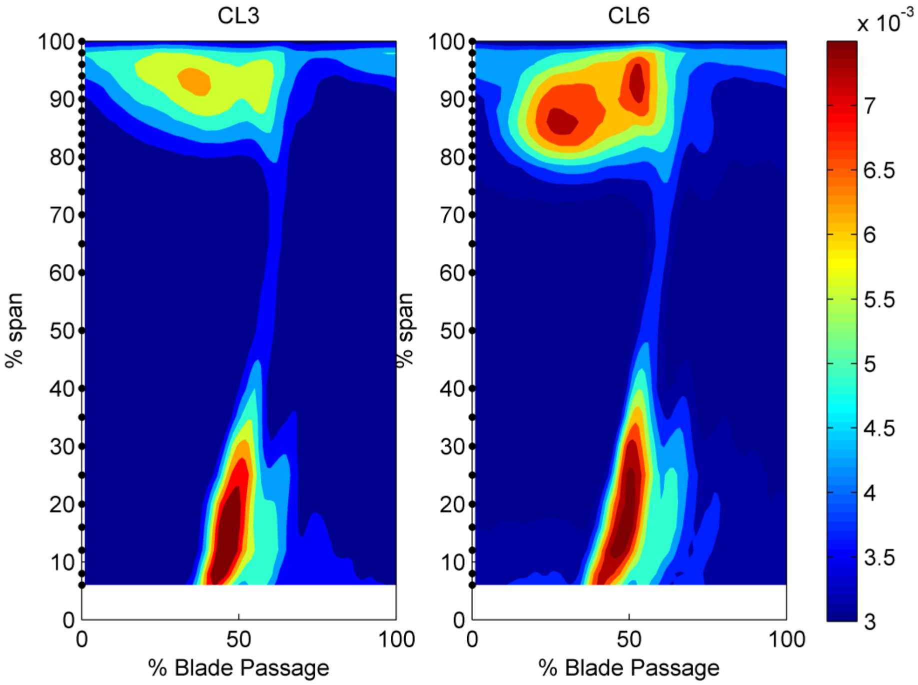

Figure 6.7 Contours of coefficient of pressure RMS at L3 for CL3 and CL6

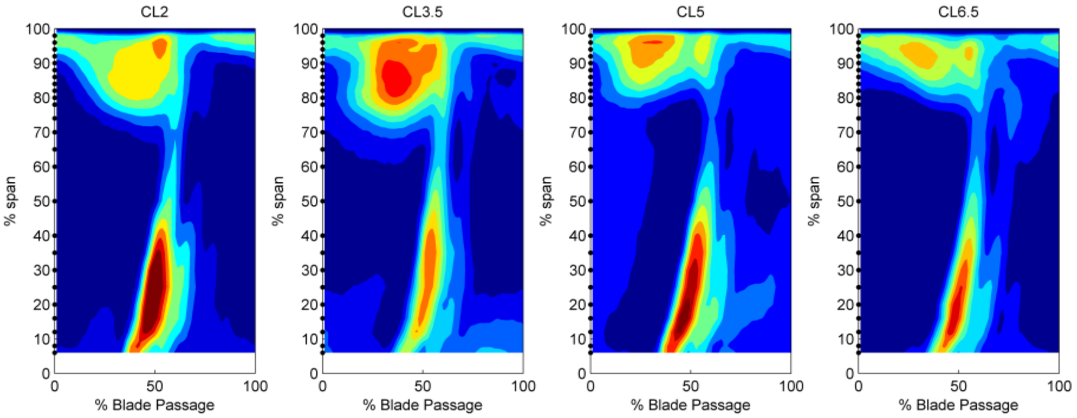

Figure 6.8 Contours of pressure coefficient RMS at L6 for CL2, CL3.5, CL5 and CL6.5

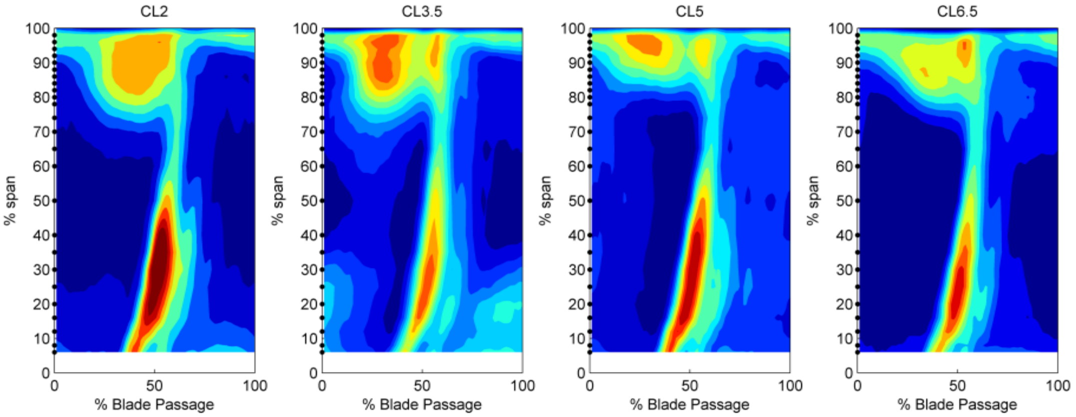

Figure 6.9 Contours of pressure coefficient RMS at L7 for CL2, CL3.5, CL5 and CL6.5

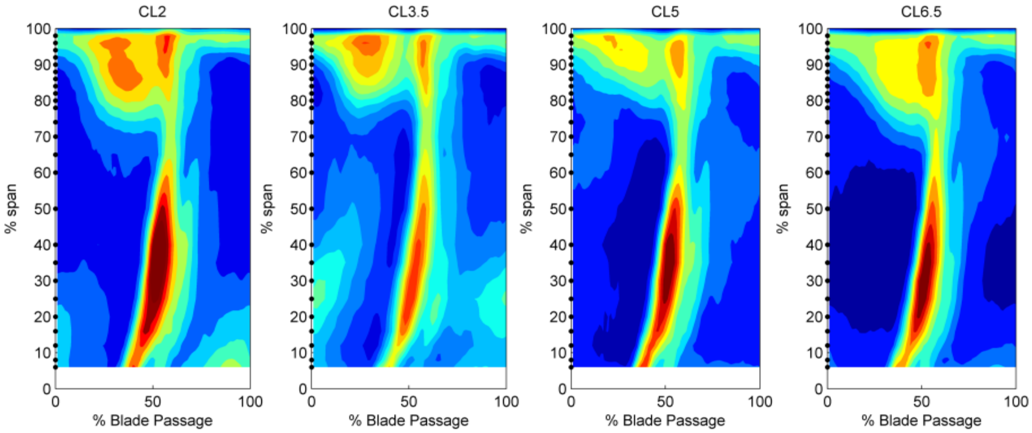

Figure 6.10 Contours of pressure coefficient RMS at L8 for CL2, CL3.5, CL5 and CL6.5

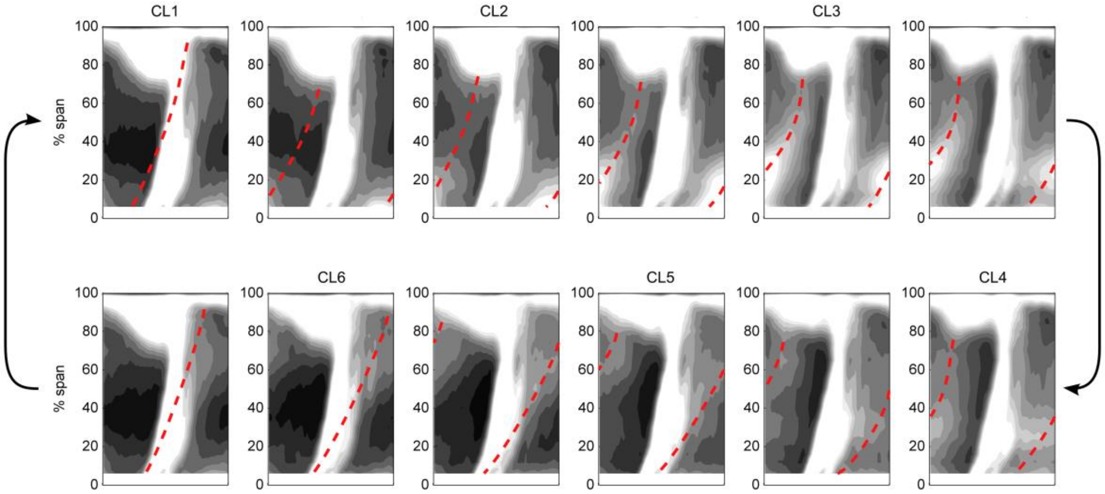

Figure 6.11 Contours of coefficient of pressure RMS at L8 for 12 clocking configurations highlighting the Stator 1 wake location

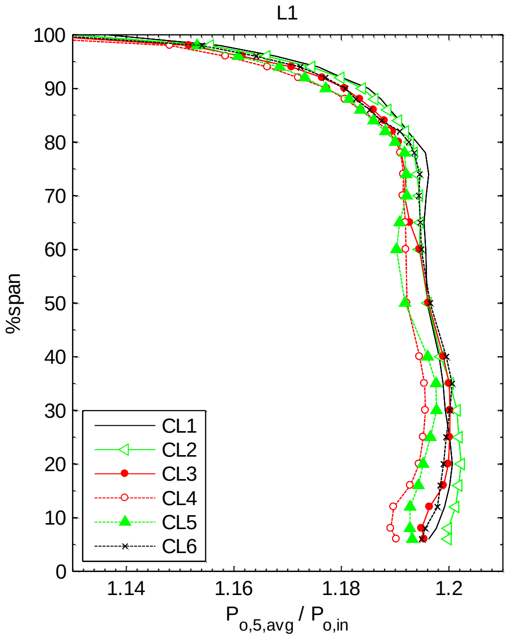

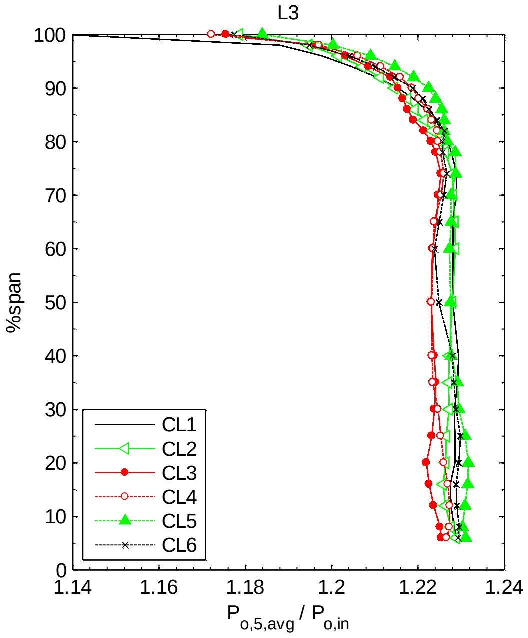

Figure 6.12 Radial total pressure profiles at Rotor 2 exit for six clocking configurations at L1

Figure 6.13 Radial total pressure profiles at Rotor 2 exit for six clocking configurations at L3

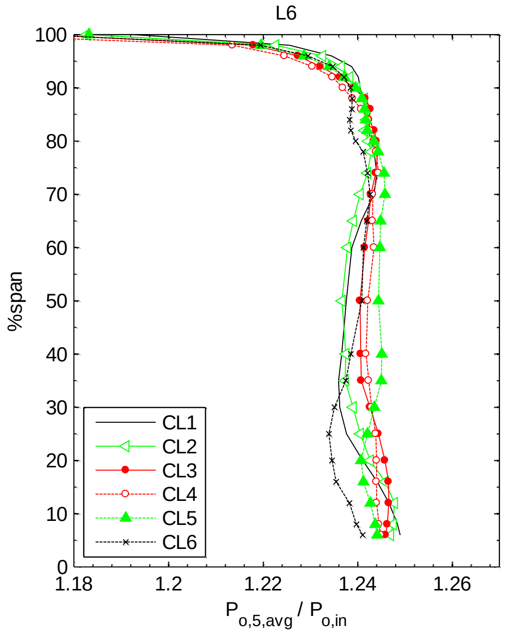

Figure 6.14 Radial total pressure profiles at Rotor 2 exit for six clocking configurations at L6

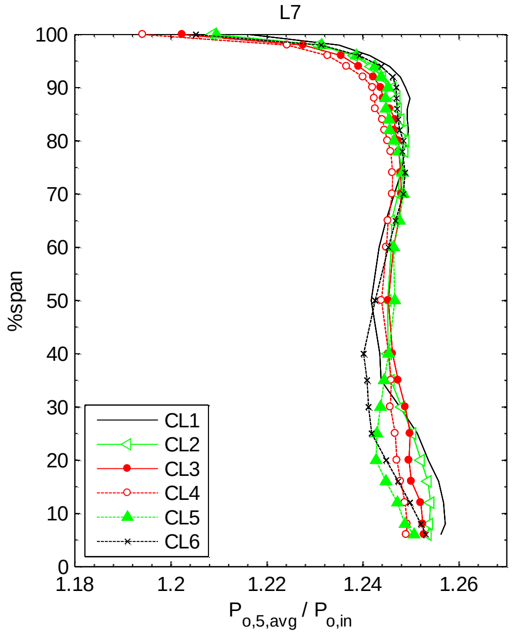

Figure 6.15 Radial total pressure profiles at Rotor 2 exit for six clocking configurations at L7

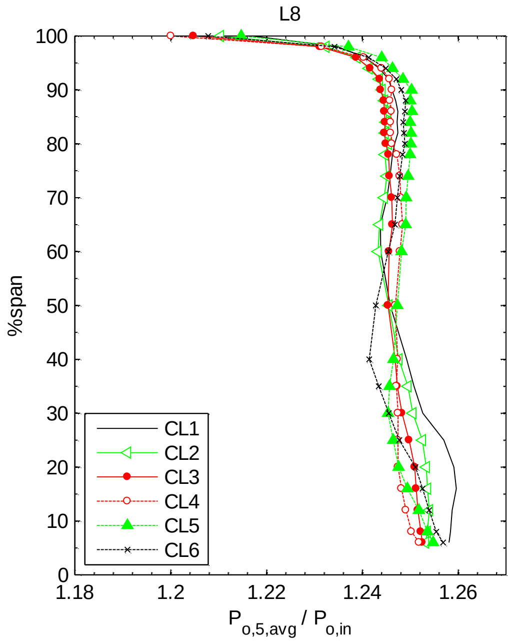

Figure 6.16 Radial total pressure profiles at Rotor 2 exit for six clocking configurations at L8

# CHAPTER 7. BLADE ROW INTERACTION EFFECTS ON STATOR SURFACE FLOWS

The effects of vane clocking on Stator 2 total pressure loss as well as unsteadiness at the Stator 2 inlet due to changes in rotor tip leakage flows prompt an investigation into the Stator 2 performance using time-resolved measurement techniques. This chapter will first address vane clocking effects on Stator 2 surface pressures using high frequency response pressure transducers embedded in the stator, and second, Stator 2 boundary layer transition is evaluated using surface-mounted hot-film anemometry. The effects of clocking on the Stator 2 surface flow development is presented at multiple loading conditions.

## 7.1 Stator 2 Surface Pressures

Vane clocking effects were measured on both the pressure side and suction side with pressure transducers at 10%, 20%, 30% and 40%axial chord, at 50% and 80%span. The transducer located at 20%$c_x$ at 50%span on the pressure side was not function upon receipt from the manufacturer, and there no data will be shown at this location. Unsteady surface pressures were acquired at six clocking configurations (CL1-CL6) at six loading conditions. This section will present data in terms of pressure coefficients and RMS similar to the previous chapter and one-dimensional trends, stator surface response, and frequency domain analysis will be shown.

### 7.1.1 One-Dimensional Pressure Distributions

The unsteady total pressure data are time-averaged to provide a description of the stator surface pressure loading. These data are shown with a pressure distribution calculated from a computational model of the compressor (Brossman et al., 2014). In Figure 7.1, pressure coefficient for 50% and 80%span are shown for two of the six loading conditions, L3 and L7. These data are for CL1 which is the nominal clocking configuration, typically used in comparison with computations. The axial location of peak pressure rise moves toward the leading edge with increased loading as expected. At the peak efficiency loading condition, the measurements and model agree that peak pressure is near 20%$c_x$. And at the L7 high loading condition, the measurements indicate that peak pressure ride is near 10%$c_x$ or closer to the leading edge; computations are not shown for this loading because it is past numerical stall.

Throughout this section the coefficient of pressure unsteadiness will be discussed in terms of an average RMS and vane clocking effects will be analyzed. Before presenting the average RMS in the following section, the surface pressure unsteadiness based on the time mean is shown and compared with the differences between clocking configurations. The scales of the effects on the Stator 2 static pressure distribution are shown by the bars in Figure 7.2 for 80%span. The RMS unsteadiness based on the time-mean are shown in Figure 7.2a. The vane clocking effects, which are shown in Figure 7.2b, are significantly smaller than the static pressure unsteadiness, and thus are scaled up by ten times to makes the changes most visible.

The effects of vane clocking on the average stator pressure differential between the pressure side and the suction side are shown in Figure 7.3 as a percent difference between the maximum and minimum configurations. Clocking Stator 1 with respect to Stator 2 has the largest effect on the Stator 2 surface pressure at the 10% and 40% axial cord locations. The lower loading conditions experience the largest relative changes in pressure coefficient, up to, but these absolute values are similar to those seen at the high loading conditions. The 80%span measurements experience larger peak differences with vane clocking than 50%span. Furthermore, the differences between clocking configurations are an order of magnitude smaller than the RMS unsteadiness values.

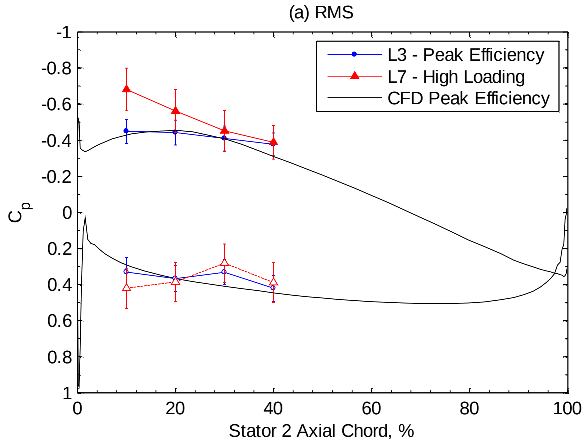

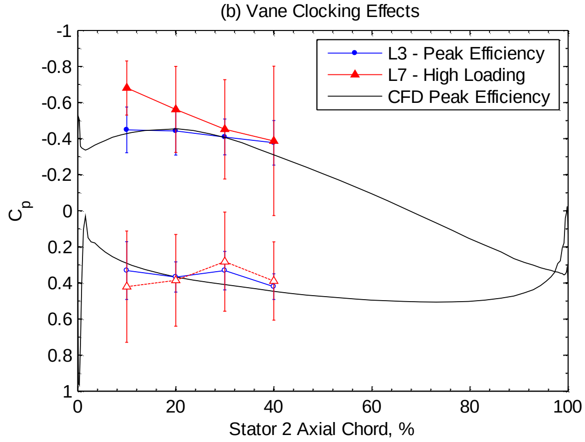

Figure 7.1 Stator 2 static pressure distribution at (a) 50%span and (b) 80%span for the peak efficiency and high loading conditions

(a) RMS

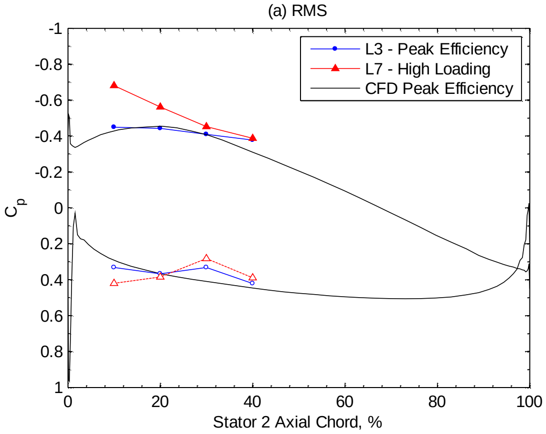

(b) Vane Clocking Effects

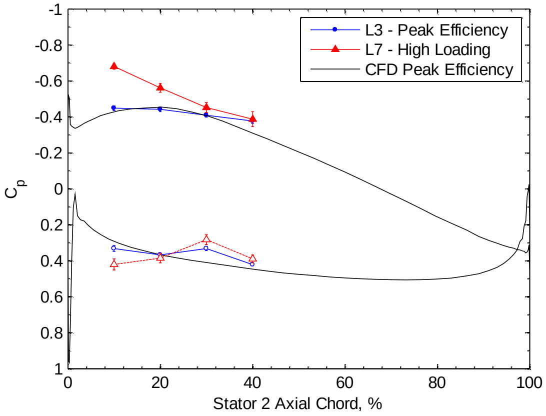

Figure 7.2 Stator 2 static pressure distribution at 80%span with bars showing scale of (a) RMS and (b) vane clocking effects scaled

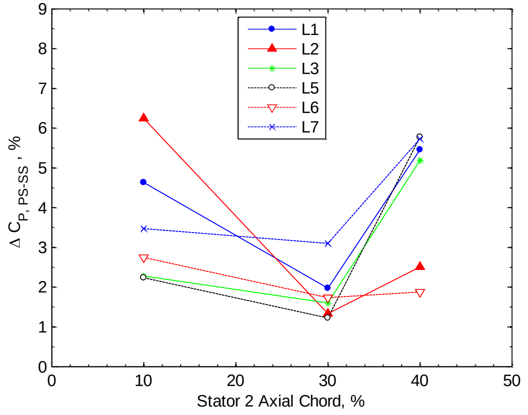
(a) 50%span

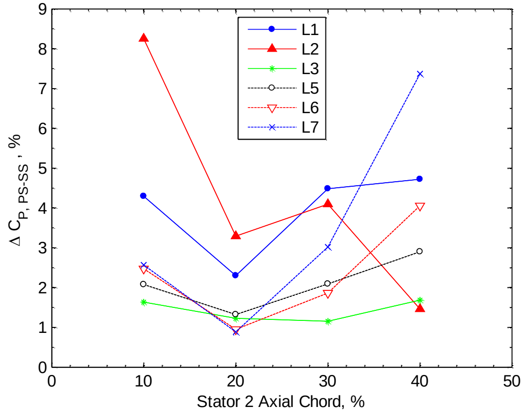
(b) 80%span

Figure 7.3 Change in Stator 2 static pressure differential between vane clocking configurations for (a) 50%span and (b) 80%span at six loading conditions

### 7.1.2 Surface Pressure Unsteadiness

To better understand the differences in average surface pressures between vane clocking configurations shown in the previous section, the changes in surface pressure response and unsteadiness to the Rotor 2 blade passing are presented.

Figure 7.4 shows contours of pressure coefficient along the Stator 2 suction surface for four Rotor 2 blade passings of the full ensemble averaged revolution at

50%span and 80%span at the high loading condition in the nominal clocking configuration, CL1. The Rotor 2 blade passing is characterized by an increase in pressure coefficient along the suction surface. These data agree with the observation from the one-dimensional results, where the 80%span operates at slightly higher pressures than 50%span. The Rotor 2 blade passings in Figure 7.4 are less distinct than data presented by some previous authors in low speed facilities. This can be attributed to the stronger multistage effects in this facility compared to data acquired in an 1.5-stage facility or in the first stage. The data shown here contain interactions from four upstream rows and two downstream rows. Furthermore, the blade counts of the two upstream rotors differ by three, which results in a three-beat modulation of signals. This has been shown to have a marked effect on the Stator 2 boundary layer transition, as shown by Smith and Key (2014) and will be discussed later in this chapter.

To more clearly define the how these fluctuations differ between clocking configurations, an average blade pass is calculated. The ensemble-averaged revolution of data is broken into 33 segments for the 33 Rotor 2 blade passings and averaged. The average pressure coefficient and RMS of the pressure coefficient for a Rotor 2 blade pass are shown in Figure 7.5 for the high loading condition. Data from the sensor at 10%$c_x$ on the suction side are shown at 50%span and 80%span. The other sensor locations exhibit effects from vane clocking, but the sensors nearest the leading edge provide a stronger definition of the surface flow response to the rotor exit flow. The center of the rotor wake is at approximately 50%bp in each plot. The rotor wake effect is seen as local pressure increase and a high RMS; this is present for all six clocking configurations. At 50%span, there are small fluctuations in the pressure signals between rotor wakes which are alter by clocking position, but the RMS values between rotor wakes are generally similar, expect of clocking configurations CL5 and CL6 which have a slightly higher mean unsteadiness. The RMS strength within the rotor wake varies with clocking configuration at 50%span. The effects of vane clocking of the Stator 2 surface pressures more significant at 80%span. In the pressure coefficient traces, the mid-rotor passage fluctuations are stronger and clearly walk through the passage with each sequential clocking configuration. The change in RMS with vane clocking configuration is more pronounced and features a secondary disturbance for some clocking configurations at 80%span. Similar to the response at 50%span, the RMS intensity in the rotor wake changes with clocking configuration. The disturbance to the left of the rotor wake influence corresponds to the effects from rotor tip leakage flows that were presented in the previous chapter. The surface unsteadiness from the Rotor 2 tip leakage flow change with each clocking configuration because as the position of Stator 1 changes, the interactions between the Stator 1 wake and Rotor 2 tip leakage flow for the same Stator 2 position. Figure 7.6 shows that the CL5 clocking configuration has the largest Rotor 2 tip leakage flow, while CL2 does not experience an increase in RMS from the Rotor 2 tip leakage flow at 80%span. These two clocking configurations correspond to the minimum and maximum Stator 2 loss configurations, respectively. Furthermore, this shows that clocking configurations from the Rotor 2 exit / Stator 2 inlet flow does lineup with the same clocking configurations at the Stator 2 leading edge for the L7 loading condition. The convection of the upstream flow filed, including wakes and secondary flow unsteadiness, changes with loading due to differences in flow angles and velocities.

The low loading condition had some of the largest differences in average pressure loading condition between vane clocking. These changes were especially strong at the 10%$c_x$ measurement location. When examining the unsteady pressure responses, both the pressure side and suction side exhibit clear changes with vane clocking. The pressure side response at the 10% axial chord is shown in Figure 7.6 for both 50% and 80%span. Similar to the surface pressure trends with clocking for the L7 loading, the fluctuations between the rotor wake passing change with each clocking configuration. The RMS at 80%span is much larger than 50%span; the two plots are shown on the same scale. Though difficult to see, the RMS in the Rotor 2 wake disturbance varies with clocking configuration at 50%span. At 80%span, the peak RMS changes by nearly 20% between clocking configurations CL3 and CL6.

(a) Suction Side 50%span

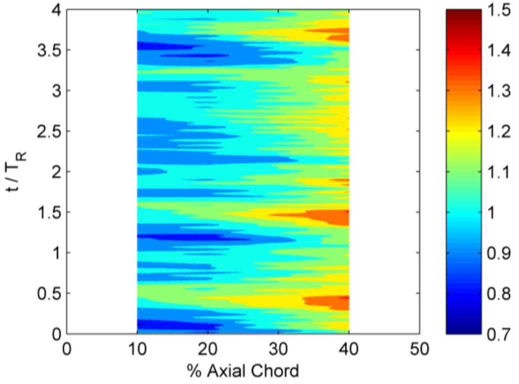

(b) Suction Side 80%span

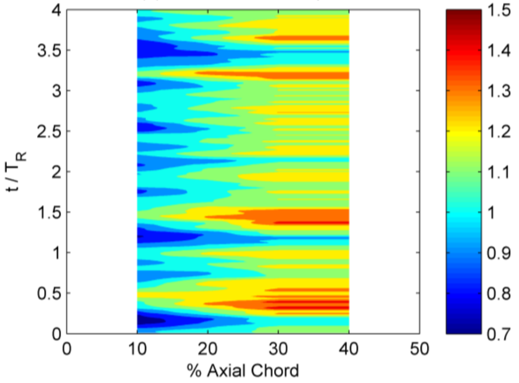

Figure 7.4 Suction surface pressure coefficient with Rotor 2 blade passing at high loading (L7) for (a) 50%span and (b) 80%span

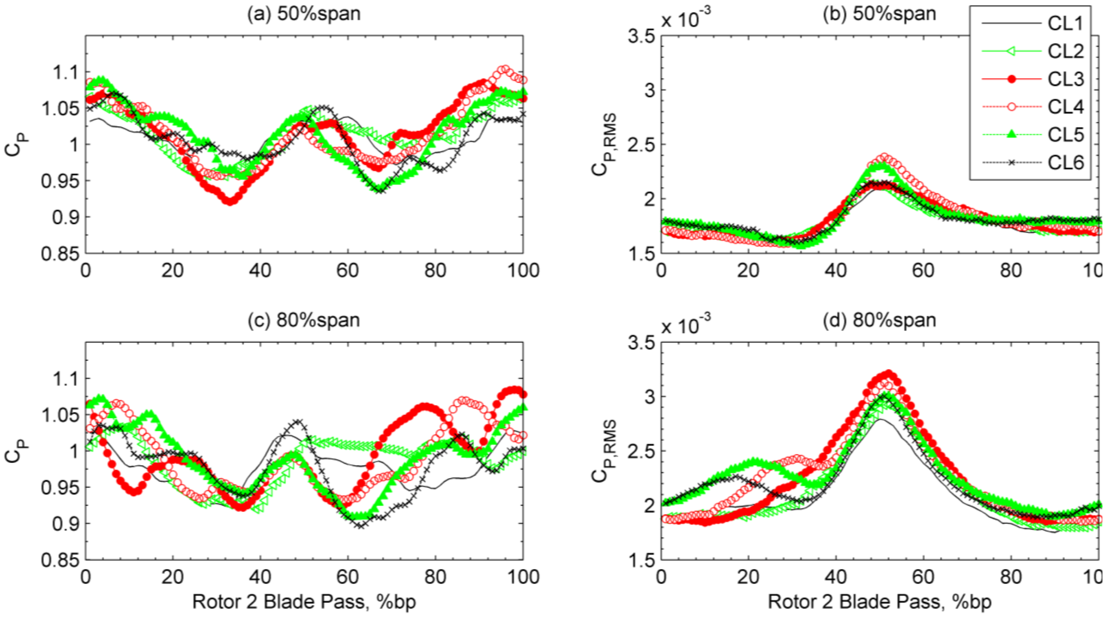

Figure 7.5 Cp and RMS for an average Rotor 2 blade pass on the suction surface at 10% axial chord for the L7 loading condition at (a,b) 50%span and (c,d) 80%span

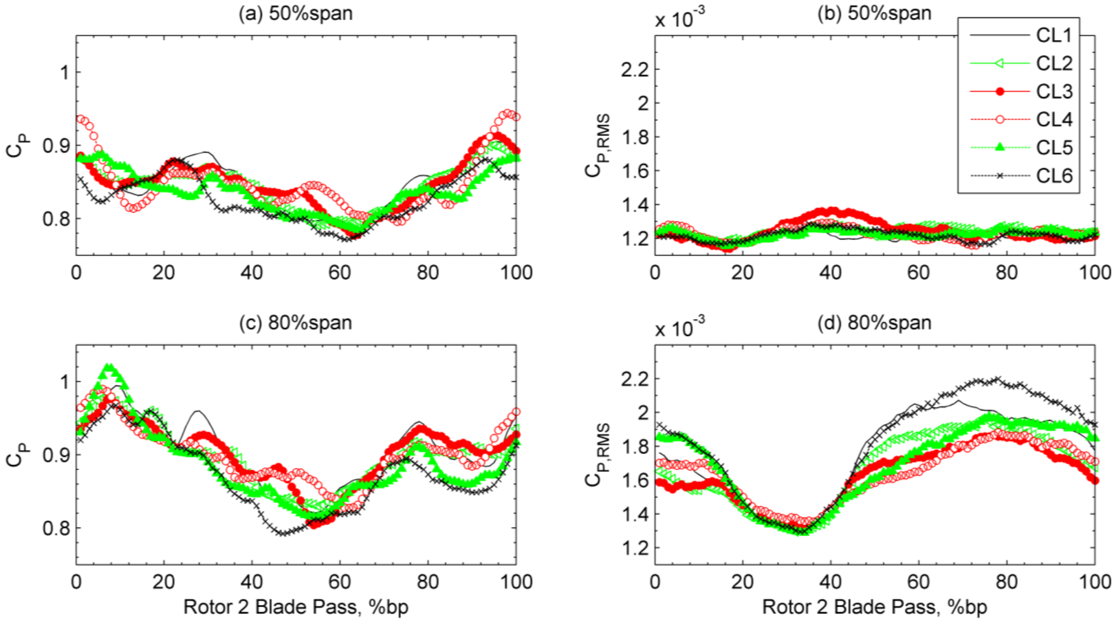

Figure 7.6 Cp and RMS for an average Rotor 2 blade pass on the pressure surface at 10% axial chord for the L1 loading condition at (a,b) 50%span and (c,d) 80%span

### 7.1.3 Frequency Domain Analysis

Fourier analysis allows for an alternative interpretation of the unsteadiness and shows the distribution of the frequency content. The average blade pass at 80%span for the high loading condition is shown for two clocking configurations (CL2 and CL5) which are markedly different are shown in Figure 7.7. The RMS signature of CL2 consists of one large peak while CL5 has a less strong peak at the same location with an additional peak. The Fourier transform of pressure coefficient for these two configurations are shown to highlight the differences in frequency content. The major frequencies are associated with the Rotor 1, Rotor 2, and Rotor 3 blade pass frequencies and harmonics. The rotor blade count decreases by three with each row, where Rotor 1 has 36 blades and Rotor 3 has 30 blades. Both signals have large 30/rev and 60/rev components. This is likely an effect from both the Rotor 3 potential field, and a modulation of -3/rev from 33/rev due to rotor-rotor interactions. The Fourier transform magnitudes vary between clocking configurations at the Rotor 1 and Rotor 2 blade pass frequencies and their harmonics. The trends observed at the L7 loading condition, shown in Figure 7.7, are also seen that the L6 loading condition with slightly less strength due to the lower pressure rise operating condition.

To highlight the differences in Fourier transforms with clocking, the magnitudes at the blade pass frequencies are shown in Figure 7.8 for the 10%$c_x$ suction side sensor at the L7 loading condition. The magnitudes for Rotor 1 and Rotor 2 blade pass frequencies, their second harmonics, and 3/rev are shown. At both 50% and 80%span, the magnitude at the Rotor 2 blade pass frequency (33/rev) changes by over five times. At clocking configurations with a lower 33/rev response, the magnitudes of the Rotor 1 blade pass frequency and its second harmonic are larger. At 80%span, the Rotor 2 blade pass frequency (66/rev) also increases when the 33/rev decreases, but at 50%span, the magnitudes at 66/rev remains relatively constant between clocking configurations. This is likely due to the presence of the Rotor 2 tip leakage flow at 80%span, which adds a second disturbance for every blade pass. Therefore, under some clocking configurations the Stator 1 wake – Rotor 2 tip leakage flow interaction which causes increased blockage, strengthens the 66/rev response at 80%span. And since the rotor tip leakage flow changes do not reach 50%span, the 66/rev response is relatively constant between clocking configurations.

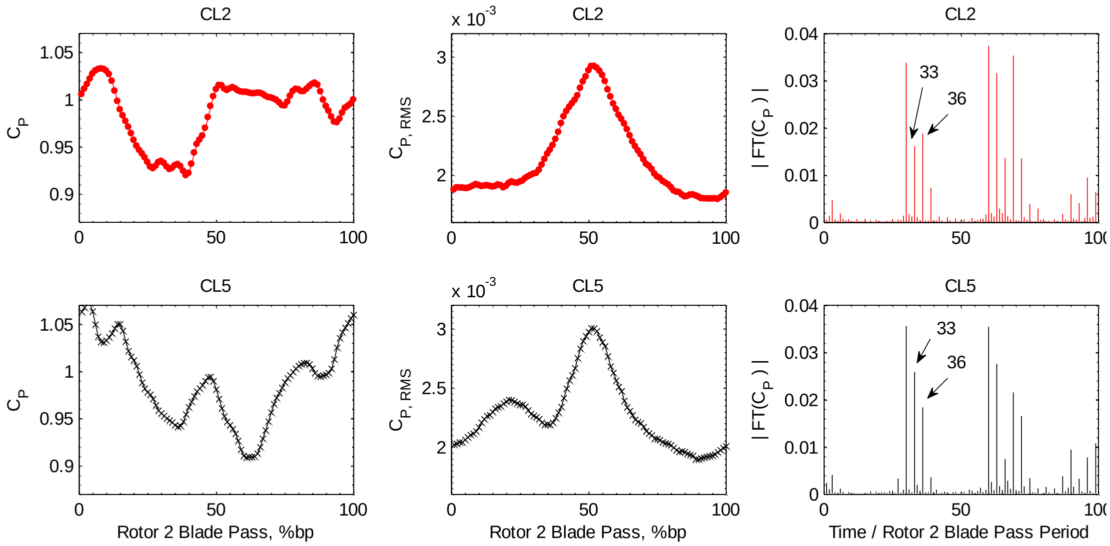

Figure 7.7 Cp and RMS for an average Rotor 2 blade pass and the Fourier transform of Cp at 10% axial chord for the L7 high loading condition at 80%span for CL2 and CL5

(a) 50%span

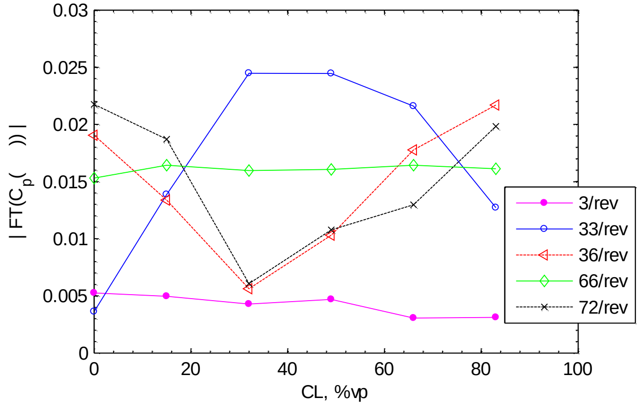

(b) 80%span

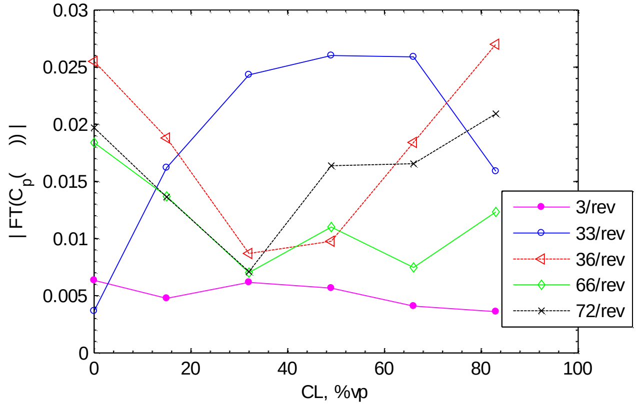

Figure 7.8 Changes in FT magnitude at blade pass frequencies with clocking configuration for L7, at 10%$c_x$ suction side

## 7.2 Stator 2 Wall Shear Stress

The wall shear stress along the Stator 2 suction side was measured using an 18-sensor surface-mounted hot-film array at 75%span. A few sensors were not operational for testing. Six vane clocking configurations were acquired at two loading conditions: peak efficiency (L3) and a low high loading point (L5). Wall shear stress data were acquired and analyzed using surface-mounted hot-film arrays in the uncalibrated method discussed in Chapter 2. This section will present the changes in Stator 2 boundary layer response with clocking configuration including the effect of rotor-rotor interactions and the mean Rotor 2 blade pass effect.

### 7.2.1 Rotor-Rotor Interaction Effects

The difference in blade counts between Rotor 1 and Rotor 2 is three, and the interaction between the rotor wakes results in 3/rev modulation of the unsteady flow field. Therefore not only are the Rotor 2 wakes inducing changes in the Stator 2 wall shear response, but the Rotor 1 wake are as well. These rotor-rotor interactions have been shown to alter the Stator 2 suction side transition in preliminary studies; these results are discusses in Smith and Key (2014).

Figure 7.9 shows space-time (st) diagrams of normalized QWSS for six clocking configurations at the peak efficiency loading condition. The data are normalized by the time-mean QWSS for each streamwise location to allow for identification of rotor wake influence. The abscissa is time normalized by Rotor 2 blade pass period. Near 8% of the Stator 2 suction side surface (ss), there are 33 peaks in QWSS that are directly related to the 33 Rotor 2 wakes. These disturbances propagate downstream along the Stator 2 surface highlighting the Rotor 2 wake-induced paths. In addition to the disturbance associated with the Rotor 2 wakes, the data have an additional unsteady characteristic featuring a 3/rev pattern associated with the Rotor 1 wakes.

A three-lobed beating pattern is apparent in all six clocking configurations in Figure 7.9. The color scales are the same for each st-diagram. The location of strongest definition of the wake paths shifts to different regions of the rotor revolution with each clocking configuration. And in the cases of clocking configurations CL2 and CL3 the range of QWSS is less than the other configurations. To understand the effect of the upstream Rotor 2 wakes and influence from blade row interactions between the Stator 1 wake and Rotor 2 tip leakage flow, the details of the measurements acquired near the leading edge are explored. The ensemble-averaged revolution of QWSS at 8%ss is shown in Figure 7.10 for six clocking configurations at the peak efficiency loading condition. The beating pattern is visible in each of these signals, but additional disturbances are more prominent for some clocking configurations. The Rotor 1 – Rotor 2 wake interaction can be mostly easily identified by locating the positions where the Rotor 1 and Rotor 2 wakes are aligned, for example and Rotor 2 blade passing 10. For configurations CL4, CL5, and CL6, the Rotor 2 wake effect at $t/T_R$ is a clear peak, but it is less defined for the other vane clocking configurations. In particular, CL2 and CL3 have significantly more disturbances within the three-beat pattern. These additional disturbances are likely connected to increased inlet unsteadiness and blockage from Rotor 2 tip leakage flows at the Stator 2 inlet.

### 7.2.2 Mean Rotor 2 Blade Pass

To isolate the effects of the Rotor 2 leakage flow changes with vane clocking from the rotor-rotor interactions, the averaging method used to calculate a mean rotor passage as presented with the high-frequency response pressure data was used. Figure 7.11 shows the surface shear stress at 8%ss response for the average Rotor 2 blade pass for six clocking configurations at peak efficiency. The effect from the Rotor 2 wake is located near 95% of the Rotor 2 blade pass. The peak change in QWSS from the Rotor 2 wake differs between the clocking configurations by approximately 7%. The level of QWSS between the Rotor 2 wake effects is also altered between vane clocking configurations. Clocking configuration CL3 has higher mean shear stress between the Rotor 2 wakes, while CL2 has a well-defined small secondary peak of increased QWSS. The other configurations exhibit evidence of a mid-Rotor passage disturbance shifting. This is similar to the gradual movement of the Rotor 2 tip leakage flows observes in the Stator 2 inlet flow traverse in Chapter 6.2.

In all data presented thus far in this research, vane clocking effects have increased when moving from a peak efficiency operation condition to a high loading condition. This was shown in the Stator 2 steady performance, Stator 2 inlet flow unsteadiness, and the Stator 2 surface pressure unsteadiness. Figure 7.12 shows the surface shear stress at 8%ss response for the average Rotor 2 blade pass for six clocking configurations at a higher loading condition (L5). Similar to the peak efficiency condition, the effect from Rotor 2 is located near 95% of the Rotor 2 blade pass. The change in peak QWSS in the Rotor 2 wake effect between clocking configurations is about 7%, similar to the peak efficiency condition. But at this higher loading condition, the QWSS disturbances between Rotor 2 wakes are as high the QWSS levels within the Rotor 2 wake disturbances. Furthermore, the QWSS response between the Rotor 2 wakes is markedly different between clocking configurations. The CL3 configuration has elevated shear stress for the majority of the Rotor 2 blade pass, but the CL6 experiences only small QWSS disturbances in the Rotor 2 mid-passage. Although this loading condition did not have significant vane clocking effects on steady total pressure loss, the surface shear stress does exhibit larger changes between clocking configurations than at the peak efficiency configuration.

By analyzing the mean Rotor 2 blade pass effects, the Rotor 1 –Rotor 2 interactions have been averaged. This allows the effects of the Stator 1 wake-Rotor 2 tip leakage flow interaction to be highlighted in the Stator 2 surface shear stress response between vane clocking. These changes in Stator 2 QWSS for a mean blade pass between clocking configurations indicate that the altered Stator 2 inlet flow due to changes Rotor 2 tip leakage is having a strong effect on the Stator 2 boundary layer response.

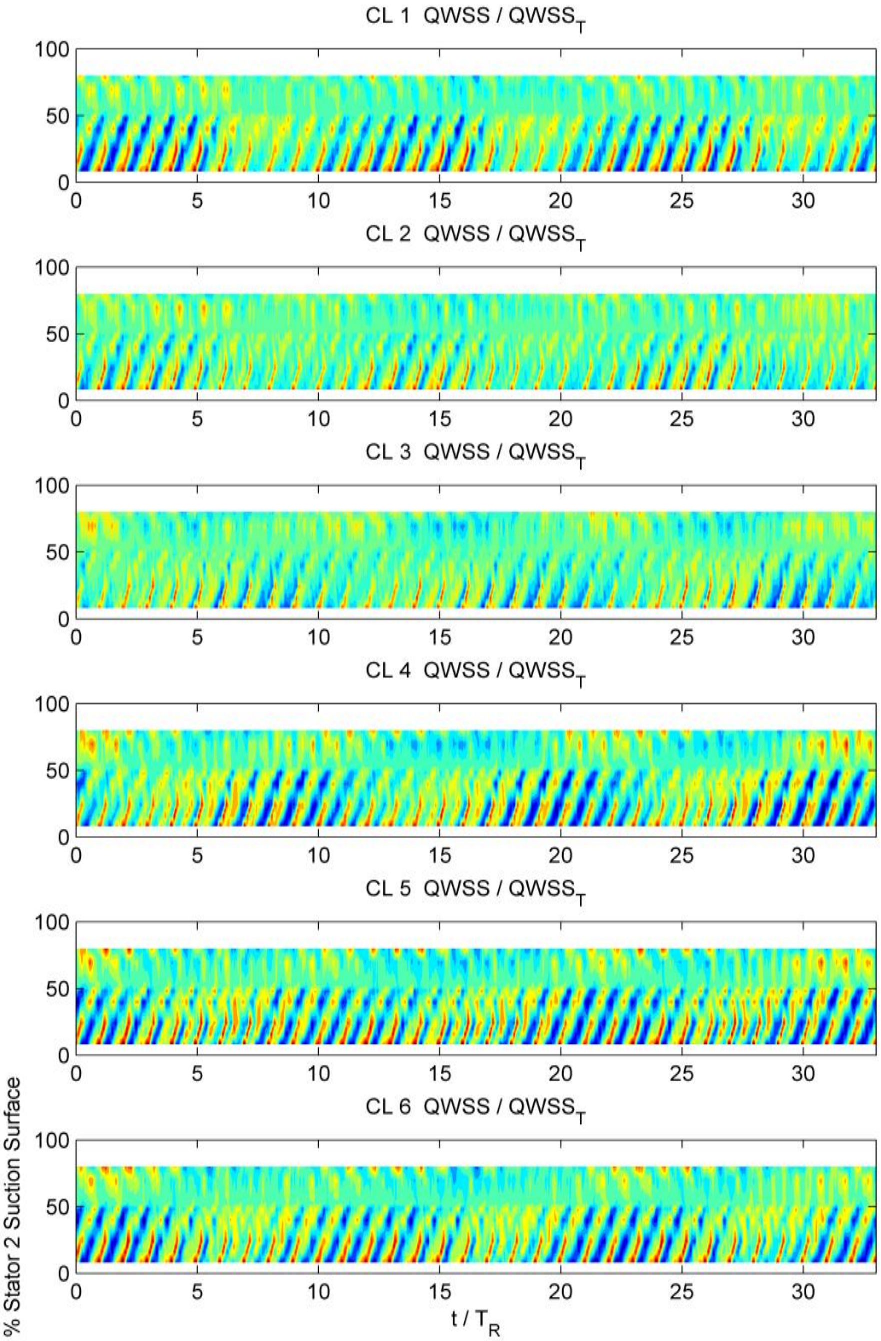

Figure 7.9 st-diamagrams of normalized QWSS for six clocking configurations at peak efficiency (L3)

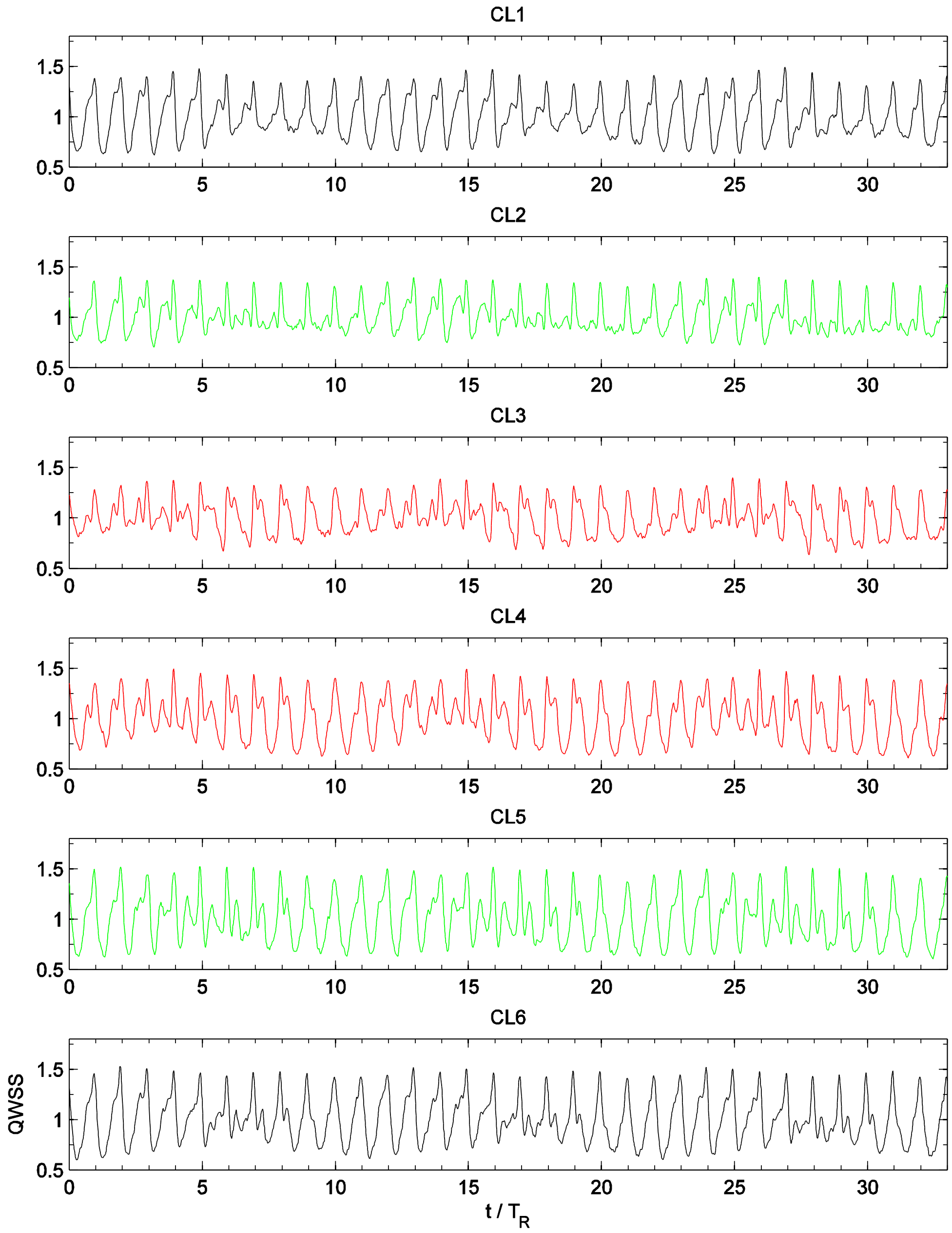

Figure 7.10 QWSS response at 8%ss for six clocking configurations at peak efficiency (L3)

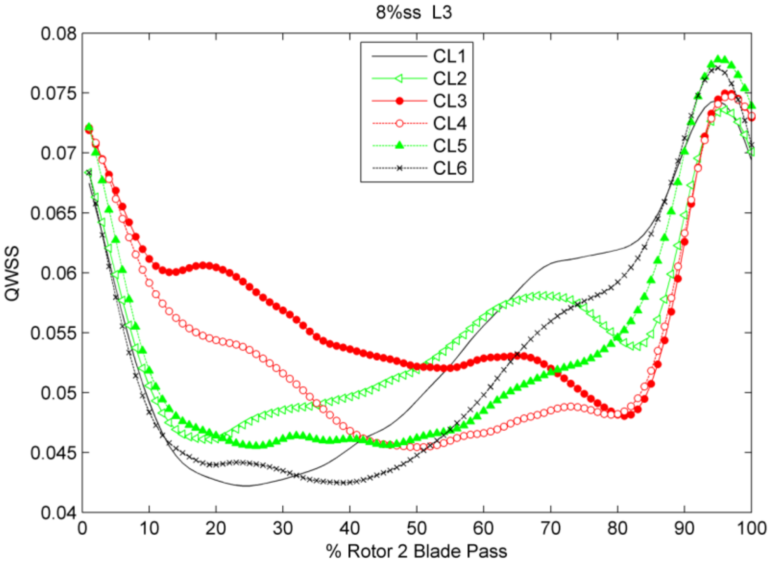

Figure 7.11 Mean Rotor 2 blade pass of QWSS response at 8%ss for six clocking configurations at peak efficiency (L3)

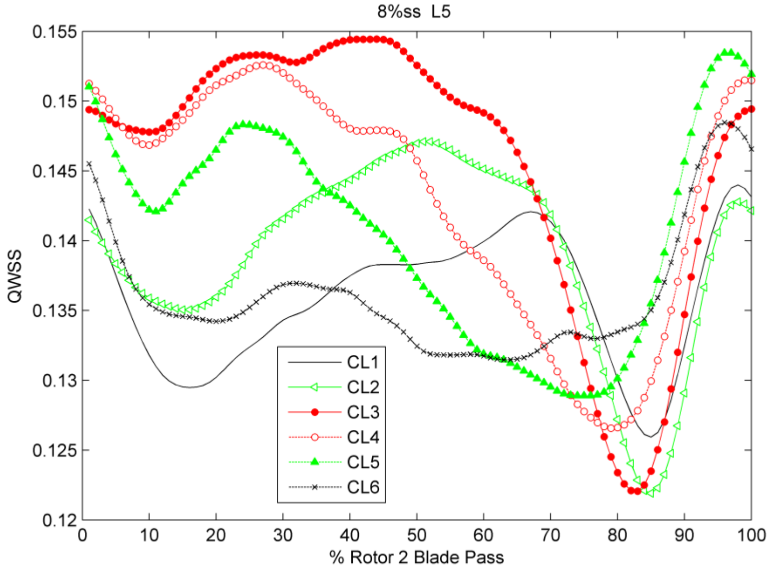

Figure 7.12 Mean Rotor 2 blade pass of QWSS response at 8%ss for six clocking configurations at higher loading (L5)

# CHAPTER 8. SUMMARY AND CONCLUSIONS

The objective of this research was to investigate the effects of blade row interactions on stator loss and boundary layer transition in a multistage compressor. The wakes and potential fields of each blade and vane are the periodic forcing functions which cause these interactions and their influence can have significant effects on compressor performance. Vane clocking, the relative circumferential indexing of adjacent vane rows with the same vane counts, has been used to alter the blade row interactions in the Purdue three-stage axial compressor. The opportunity for performance benefits with vane clocking has been well documented in the open literature, but the driving flow physics have yet to be identified. Furthermore, standard compressor design codes cannot capture these effects, and thus, they are not considered in the design process, despite their impact on both aerodynamic performance and aeromechanical response.

The Purdue three-stage axial compressor models the rear stages of a high pressure compressor and operates at engine-representative Reynolds numbers and Mach numbers. The inlet guide vane, Stator 1, and Stator 2 all have 44 vanes which enable vane clocking of the embedded stage, while the rotors have different blade counts producing amplitude modulation of the unsteady interactions. These blade row interactions are investigated using several steady and time-resolved measurement techniques.

A detailed investigation of corrected conditions has been presented to establish repeatable, compressor performance year-round in this facility which utilizes ambient inlet conditions. A method of including humidity in the correction of rotational speed and mass flow rate is presented as well as the effects of correction for density and work coefficient, Reynolds number considerations, and the effects of large changes in inlet temperature. The omission of relative humidity in compressor corrected conditions has the potential to misrepresent corrected rotational speed by up to 0.6% and corrected mass flow rate by up to 0.8%. Additionally, a correction procedure for density and work coefficient was imposed for data collected from the Purdue three-stage axial compressor facility with two different tip clearance configurations under different ambient conditions. Applying this correction procedure for data collected with cold and hot ambient inlet conditions reduced measured differences by only 0.05%, which is less than half of the measurement uncertainty.

Reynolds number trends with respect to the machine and blade rows were also assessed. These assessments showed ambient conditions representing typical seasonal variations in the Midwest United States can cause large changes (10% different) in Reynolds numbers. However, for this range of Reynolds numbers, the airfoils in the Purdue three-stage compressor operate in a regime which is independent of Reynolds number, far above the transitional Reynolds number. As a result, the changes in overall total pressure ratio with ambient conditions were, therefore, attributed to the small changes measured in rotor tip clearance.

The tip clearance changes due to ambient temperature changes can exceed 0.1% span. On hot days, the tip clearance runs larger, and this is because the aluminum casing grows more compared to the thermal and centrifugal growth of the blade (even for the larger mechanical speeds that are run on hot days to match corrected conditions). A comparison of data collected on hot and cold days verified this trend. As a result, this tip clearance change due to day-to-day variations in thermal growth, which is typically considered in literature to be a negligible effect, is not only measurable, but it is significant.

Quantifying these second-order effects on compressor performance required significant testing of the same compressor with different rotor tip clearances throughout the year to provide quality datasets on both hot and cold days. This type of dataset is rarely available or presented in the literature. Without proper humidity accounting and an understanding of the potential for inlet temperature changes to affect clearances due to thermal growth, measuring small performance changes in detailed research studies could be indiscernible.

The methodology and implementation of powder paint based flow visualization techniques along with the illuminated flow physics are presented in detail. This method assists in understanding the loss development in the compressor by highlighting stator corner separations and endwall flow patterns. Effects of loading condition, rotor tip clearance height, and stator wake and rotor tip leakage interactions are shown with this technique. In a multistage compressor, losses build differently from stage to stage and as loading conditions change. These flow visualization images can be used for comparison with CFD to allow for model validation of stage matching, especially in flow separation regions, which can be difficult to calculate well using common RANS design tools.

These visualizations also provided valuable comparisons between experimental configurations, such as the vane clocking and tip clearance data presented in this study. Specifically, the effects of increased rotor tip clearance on stator loss were made clear with surface streaklines at two loading conditions. For the 3% and 4%TC at the high loading condition, the vane streaklines contained increased radial flow at the tip and reduced hub corner separations due to increased blockage at the tip from larger tip leakage vortices. Furthermore, stator total pressure loss changes due to vane clocking were explained by demonstrating the modulation of the Stator 2 hub corner separation between two clocking configurations. Surface flow visualizations in this study have provided valuable information to reinforce the explanation of flow physics associated with stator losses.

Vane clocking effects on steady compressor performance were quantified for nine loading conditions for six clocking configurations – the largest vane clocking dataset in the open literature. The Stator 2 wake shapes were affected by the amount of interaction between Stator 2 and the Stator 1 wake. While the differences in Stator 2 wake width and depth with clocking were measureable at lower loadings, these changes were small when placed on the same scale as the changes measured in the high loading cases.

For high loading conditions, vane clocking effects were three times as strong at the hub compared to the tip. At high loading condition with the strongest vane clocking effects, the difference in wake width between the maximum and minimum configurations (CL2 and CL5) was 10%vp. This resulted in significantly different radial total pressure profile shapes, which can have important implications to a design engineer. Furthermore, the local vane clocking effects at the hub region resulted in a change in Stator 2 loss coefficient of 48%, which is over twice as large as the changes at the tip for the high loading case. These local changes resulted in a 21.7% difference in 1-D loss coefficient between the minimum and maximum clocking cases. As loading was increased further toward stall, the effects of vane clocking decreased.

To further address these clocking trends, high-frequency response data were acquired at the Stator 2 inlet and along the Stator 2 surface. The unsteadiness at the Stator 2 inlet was quantified with detailed radial traverses of an unsteady total pressure probe for the different clocking configurations. These data illuminate the effects of interactions between the Stator 1 wake and Rotor 2 tip leakage flow, which result in significantly different inlet flow conditions for Stator 2. When the rotor chops the stator wake, its tip clearance flow develops differently than if the rotor were between stator wakes. The leakage flow trajectory is also altered based on the position of the stator wake within the rotor passage as shown by these data. These rotor tip leakage flow differences exist in a circumferentially periodic pattern corresponding to the upstream vane pitch in the downstream flow. And thus, the high unsteadiness and blockage region formed by the rotor tip leakage flow changes in size and shape between vane clocking configurations. At the high loading condition, the radial depth of this blockage region was more than 10%span further into the flow between clocking configurations. Furthermore, the time-averaged total pressure radial profiles exhibited significant changes in shape between clocking configurations. The stator wake-rotor tip leakage interaction had larger differences in the Stator 2 inlet flow field between clocking configurations at high loading compared to low loading. These results compared well with the vane clocking effects on Stator 2 total pressure loss for different loadings, where the high loading conditions resulted in larger differences in total pressure loss.

Finally, measurements of the Stator 2 surface flows were acquired to investigate the vane clocking effects on unsteady surface pressures and boundary layer transition. Flush mounted high-frequency response pressure transduces on the pressure and suction surfaces were used to measure surface pressure unsteadiness. These data revealed that the Stator 2 performance is influenced by blade row interactions including rotor-rotor interactions, stator wake-rotor tip leakage flow interactions, and vane clocking.

This investigation of blade row interactions is a significant contribution to the understanding of the underlying vane clocking flow physics. The characterization of steady stator losses with vane clocking is the most extensive in the open literature. Moreover, the results demonstrating the differences in the rotor exit flow field due to stator wake-rotor tip leakage flow interactions are the first of their kind and are directly linked to vane clocking. By changing the level of unsteadiness at the downstream stator inlet, vane clocking alters the downstream stator’s unsteady performance and steady total pressure loss.

# REFERENCES

# REFERENCES

Adamczyk, J.J., 1996, “Wake Mixing in Axial Flow Compressors,” ASME Paper 96-GT-29.

Arndt, N., 1993, “Blade Row Interaction in a Multistage Low-Pressure Turbine,” *ASME Journal of Turbomachinery,* Vol. 115, No. 1, pp. 137-146.

Arnone, A., Marconcini, M., Pacciani, R., Schipani, C., and Spano, E., 2002, “Numerical Investigation of Airfoil Clocking in a Three-Stage Low-Pressure Turbine,” *Journal of Turbomachinery,* Vol. 124, pp. 61-68.

Balje, O.E, 1981, *Turbomachines: A Guide to Design, Selection, and Theory,* John Wiley & Sons, New York, pp. 34-46.

Ball, PR, 2013, An Experimental and Computational Investigation on the Effects of Stator Leakage Flow on Compressor Performance. MS Thesis, Aeronautics and Astronautics, Purdue University, West Lafayette.

Barankiewicz, W. S. and Hathaway, M. D., 1997, “Effects of Stator Indexing on Performance in a Low Speed Multistage Axial Compressor,” *ASME Paper* No. 97-GT-496.

Bellhouse, B.J., and Schultz, D.L., 1966, “Determination of Mean and Dynamic Skin Friction, Separation and Transition in Low-Speed Flow With a Thin- Film Heated Element,” *Journal of Fluid Mechanics,* Vol. 24, No. 2, pp. 379-400.

Berdanier RA, Smith NR, Fabian JC, Key NL, 2015, “Humidity Effects on Experimental Compressor Performance—Corrected Conditions for Real Gases,” *Journal of Turbomachinery*. 137: 031011 (10 pages).

Berdanier RA, Key NL, 2015a, “Tip Leakage Flow Effects on Multi-Stage Compressor Performance for Small Core Engine Applications,” Submitted to *Journal of Turbomachinery*.

Berdanier, R.A. and Key, N.L., 2015b, “Experimental Investigation of Factors Influencing Operating Rotor Tip Clearance in Multistage Compressors,” *International Journal of Rotating Machinery,* Article ID 146272, 14 pages.

Berdanier, R.A., 2015, “An Experimental Characterization of Tip Leakage Flows and Corresponding Effects on Multistage Compressor Performance” Ph.D., Mechanical Engineering, Purdue University, West Lafayette.

Binder, A., Schroeder, Th., and Hourmouziadis, J., 1989, “Turbulence Measurements in a Multistage Low-Pressure Turbine,” *Journal of Turbomachinery,* Vol. 111, No. 2, pp. 153-161.

Bons, J.P., 2010, “A Review of Surface Roughness Effects in Gas Turbines,” *Journal of Turbomachinery,* Vol. 132, No. 2, pp. 021004-1-021004-16.

Boyd, D.M. and Fleeter, S. 2003, “Axial Compressor Blade-to-Blade Unsteady Aerodynamic Variability,” Journal of Propulsion and Power, Vol. 19, No. 2.

Brossman, J. R., Smith, N. R., Talalayev, A., and Key, N. L., 2011, “Tailoring Inlet Flow to Enable High Accuracy Compressor Performance Measurements,” *Int. J. Turbo Jet-Engines*, Vol. 28, pp. 309–320.

Brossman, J.R., Ball, P.R., Smith, N.R., Methel, J., and Key, N.L., 2014 “Sensitivity of Multistage Compressor Performance to Inlet Boundary Conditions,” *Journal of Propulsion and Power*, Vol. 3, No. 2, pp.407-415.

Buckingham, E., 1914, “On Physically Similar Systems; Illustrations of the Use of Dimensional Equations,” *Physical Review Bureau of Standards*, Vol. 4 No. 4, pp. 345-376

Capece, S. R., Manwaring, S. R., Fleeter, S., 1986, “Unsteady Blade Row Interactions in a Multistage Compressor,” *AIAA Journal of Propulsion*, Vol. 2, No. 2, pp. 168-174.

Cargill, P., 2014, private communications.

Chang, P.K., 1970, Separation of Flow. Pergamon Press, New York, Interdisciplinary and Advanced Topics in Science and Engineering, Vol. 3.

Cherrett, M.A. and Bryce, J.D., 1992, “Unsteady Viscous Flow in a High-Speed Core Compressor,” *ASME Journal of Turbomachinery*, Vol. 114, No. 2, pp. 287-294.

Cumpsty NA, 2004, *Compressor Aerodynamics*. Krieger Publishing Company, Malabar, FL, pp 310-346.

Cyrus V, Pelnar J, 1989, “Flow Visualization in the Stator Blade Row of an Axial Compressor Stage,” In: Reznicek (ed) *Flow Visualization V*, Proceedings of the Fifth International Symposium of Flow Visualization, Hemisphere Publishing Corporation, New York, pp 654-659.

Day, I., 1993, “Stall Inspection in Axial Flow Compressors,” *Journal of Turbomachinery,* Vol. 115, pp. 1-9.

Délery, J.M., 2001, “Robert Legendre and Henry Werle: Toward the Elucidation of Three-Dimensional Separation,” *Annu. Rev. Fluid Mech.* Vol. 33, pp. 129–154.

Denton, JD, 2010, “Some Limitations of Turbomachinery CFD,” *ASME Paper No. GT2010-22540*.

Deregel, P. and Tan, C.S., 1996, “Impact of Rotor Wakes on Steady-State Axial Compressor Performance,” ASME Paper 96-GT-253.

Dixon, S.L., 2005, *Fluid Mechanics and Thermodynamics of Turbomachinery*, Elsevier, Burlington, MA, pp. 16-20.

Dong, Y., Gallimore, S. J., and Hodson, H. P., 1987, “Three-Dimensional Flows and Loss Reduction in Axial Compressors,” *Journal of Turbomachinery*, Vol. 109, pp. 354–361.

Dong, Y. and Cumpsty, N.A., 1990, “Compressor Blade Boundary Layers: Part 1 – Test Facility and Measurements with No Incident Wakes,” *Journal of Turbomachinery*, Vol. 112, pp. 222-230.

Dong, Y. and Cumpsty, N.A., 1990, “Compressor Blade Boundary Layers: Part 2 – Measurements with Incident Wakes,” *Journal of Turbomachinery*, Vol. 112, pp. 231-240.

Dorney, D. J. and Sharma, O. P., 1996, “A Study of Turbine Performance Increases through Airfoil Clocking,” *AIAA Paper No.* 96-2816.

Dorney, D.J., Sharma, O.P., and Gundy-Burlet, K. L., 1998, “Physics of Airfoil Clocking in a High-Speed Axial Compressor,” *ASME Paper No. 98- GT-82*.

Dring, R. P., Joslyn, H. D., and Hardin, L. W., 1982, “An Investigation of Compressor Rotor Aerodynamics,” *Journal of Turbomachinery*, Vol. 104, pp. 84–96.

Flegg, H. G., 1974, *From Geometry to Topology*, English Universities Press, London.

Fulayter, R.D., 2004, “An Experimental Investigation of Resonant Response of Mistuned Fan and Compressor Rotors Utilizing NSMS,” Ph.D. Dissertation, Purdue University, West Lafayette.

Garzon, V.E. and Darmofal, D.L., 2003, “Impact of Geometric Variability on Axial Compressor Performance,” *Journal of Turbomachinery*, Vol. 125, pp. 692-703.

Gbadebo, S.A.., Cumpsty, N.A., and Hynes, T.P., 2005, “Three Dimensional Separations in Axial Compressors,” *Journal of Turbomachinery*, Vol. 127, pp. 331-339.

Gbadebo, S.A., Cumpsty, N.A., and Hynes, T.P., 2007, “Interaction of Tip Clearance Flow and Three Dimensional Separations in Axial Compressors,” *Journal of Turbomachinery*, Vol. 129, pp. 679-685.

Graf, M.B., Wong, T.S., Greitzer, E.M., Marble, F.E., Tan, C.S., Shin, H.W., and Wisler, D.C., 1998, “Effects of Nonaxisymmetric Tip Clearance on Axial Compressor Performance and Stability,” *Journal of Turbomachinery*, Vol. 120, No. 4, pp. 648-661.

Griffin, L.W., Huber, F.W., and Sharma, O.P., 1996, “Performance Improvement Through Indexing of Turbine Airfoils: Part 2 – Numerical Simulation,” *Journal of Turbomachinery*, Vol. 118, pp. 636-642.

Gostelow, J.P., and Walker, G.J., 1991, “Similarity Behavior in Transitional Boundary Layers Over a Range of Adverse Pressure Gradients and Turbulence Levels,” *Journal of Turbomachinery*, Vol. 113, pp. 617-624.

Gostelow, J.P., Thomas, R.L. and Adebayo, D.S., 2009, “On the Response of a Strongly Diffusing Flow to Propagating Wakes,” *Journal of Turbomachinery*, Vol. 131, pp. 021006-1 – 021006-8.

Gundy-Burlet, K.L., and Dorney, D.J., 1997, “Physics of Airfoil Clocking in Axial Compressors,” *ASME Paper No. 97-GT-444*.

Gupta A, Khalid SA, McNulty GS, Dailey L, 2003, “Prediction of Low Speed Compressor Rotor Flowfields with Large Tip Clearances,” *ASME Paper No. GT2003-38637*.

Hall, E.J., 1998, “Aerodynamic Modeling of Multistage Compressor Flow Fields Part 1: Analysis of Rotor-Stator-Rotor Aerodynamic Interaction,” *Proceedings of the Institution of Mechanical Engineers*, Vol. 212, Part G, pp. 77-89.

Halstead, D.E., Wisler, D.C., Okiishi, T.H., Walker, G.J., and Hodson, H.P., 1997, “Boundary Layer Development in Axial Compressors and Turbines: Parts 1-4,” *Journal of Turbomachinery*, Vol. 119, No. 1, pp114-139, No. 2 , pp. 225-237, No. 3, pp. 426-444.

Hansen, J.L. and Okiishi, T.H., 1989, “Rotor-Wake Influence on Axial-Compressor-Stator Boundary Layers,” *Journal of Propulsion and Power*, Vol. 5, No. 1, pp. 89-94.

Hodson, H.P. and Howell, R.J., 2005, “Bladerow Interactions, Transition, and High-Lift Aerofoils in Low-Pressure Turbines,” *Annual Review of Fluid Mechanics*, Vol. 37, pp. 71-98.

Hodson, H.P., Huntsman, I., and Steele, A.B., 1994, “An Investigation of Boundary Layer Development in a Multistage LP Turbine,” *Journal of Turbomachinery*, Vol. 116, pp. 375-383.

Horlock, J.H., Louis, J.F., Percival, P.M.E., Lakshminarayana, B., 1966, “Wall Stall in Compressor Cascades,” *J. Basic Engineering*, Vol. 88, pp.637-648.

Howell, R.J., Hodson, H.P., Schulte, Stieger, R.D., Schilffer, H., Haselbach, F., Harvey, N.W., 2002, “Boundary Layer Development in the BR710 and BR715 LP Turbines – The

Implantation of High-Lift and Ultra-High-Lift Concepts," *Journal of Turbomachinery*, Vol. 124, No. 3, pp. 385-392.

Hsu, S. T., and Wo, M. A., 1998, "Reduction of Unsteady Blade Loading by Beneficial of Vortical and Potential Disturbances in an Axial Compressor with Rotor Clocking," *Journal of Turbomachinery*, Vol. 120(4), pp. 705-713.

Huber, F. W., Johnson, P. D., Sharma, O. P., Staubach, J. B., and Gaddis, S. W., 1996, "Performance Improvement Through Indexing of Turbine Airfoils: Part 1 – Experimental Investigation," *Journal of Turbomachinery*, Vol. 118(4), pp. 630-635.

Hughes, J.D. and Walker, G.J., 2001, "Natural Transition Phenomena on an Axial Compressor Blade," *Journal of Turbomachinery*, Vol. 123, pp. 392-401.

Hunt, J. C. R., Abell, C. J., Peterka, J. A., and Woo, H., 1978, ''Kinematical Studies of Flow Around Free or Surface-Mounted Obstacles; Applying Topology to Flow Visualization,'' *Journal of Fluid Mechanics*, Vol. 86, Part 1, pp. 179–200.

Hynes, T.P, and Greitzer, E.M, 1987, "A Method for Assessing Effects of Circumferential Flow Distortion on Compressor Stability," *Journal of Turbomachinery*, Vol. 109, No. 3, pp. 371-379.

Kamiyoshi, S. and Kaji, S., 1992, "Tone Noise Reduction of Multi-stage Fan by Airfoil Clocking," *AIAA Paper No.* 2000-1992, pp. 1-10.

Kerrebrock, J.L. and Mikolajczak, A.A., 1970, "Intra-Stator Transport of Rotor Wakes and Its Effect on Compressor Performance," Journal of Engineering for Power, Vol. 92, pp. 359-368.

Key, N.L., Lawless, P.B., and Fleeter, S., 2004, "Rotor Wake Variability in a Transonic Compressor Stage," Proceedings of ASME Turbo Expo, Vienna, Austria, June 14-17, *ASME Paper GT-2004-53486*.

Key, N.L., Lawless, P.B., and Fleeter, S., 2008, "An Investigation of the Flow Physics of Vane Clocking using Unsteady Flow Measurements," *Proceedings of ASME Turbo Expo*, Berlin, Germany, *GT2008-51091*.

Key, N. L., Lawless, P.B., and Fleeter, S., 2010a, "An Experimental Study of Vane Clocking Effects on Embedded Compressor Stage Performance," *Journal of Turbomachinery*, Vol. 132, No. 1, pp. 1-10.

Key, N.L., Lawless, P.B., and Fleeter, S., 2010b, "Rotor Wake Variability in a Multistage Compressor," *Journal of Propulsion and Power*, Vol. 26, No. 2, pp. 344-352.

Key, N. L., 2013, "Compressor Vane Clocking Effects on Embedded Rotor Performance," *Journal of Propulsion and Power*, Vol. 30, No. 1, pp246-248.

King, A., 2014, private communications.

Konig, S., Stoffel, B., and Schobeiri, M.T., 2009, “Experimental Investigation of the Clocking Effect in a 1.5-Stage Axial Turbine—Part II: Unsteady Results and Boundary Layer Behavior,” *Journal of Turbomachinery*, Vol. 131, pp. 1-12.

Krug, A., Busse, P., Vogeler, K., 2014, “Experimental Investigation of the Steady Wake-Tip Clearance Vortex Interaction in a Compressor Cascade,” *Journal of Turbomachinery*, Accepted Manuscript, TURBO-14-1244.

Johnston, R.T., Freiereisen, J.M., and Fleeter, S., 1998, “Measured Rotor Wake and Potential Forcing Functions Including Blade Row Interactions,” *Journal of Propulsion and Power*, Vol. 14, No. 2, pp. 191-198.

Joslyn, D. H., and Dring, R. P., 1985, “Axial Compressor Stator Aerodynamics,” *ASME J. Heat Transfer*, Vol. 107, pp. 485–493.

Jouini, D. B. M., Little, D., Bancalari, E., Dunn, M., Haldeman, C., and Johnson, P. D., 2003, “Experimental Investigation of Airfoil Wake Clocking Impacts on Aerodynamic Performance in a Two Stage Turbine Test Rig,” *ASME Paper No.* GT2003–38872.

Lakshminarayana, B, 1996, *Fluid Dynamics and Heat Transfer of Turbomachinery*, John Wiley & Sons, New York, pp. 59-70.

Walsh, P.P. and Fletcher, P., 2004 Gas Turbine Performance, Blackwell Science, Oxford, pp. 143-158.

Lighthill, M. J., 1963, “Attachment and Separation in Three-Dimensional Flows,” *Laminar Boundary Layers*, L. Rosenhead, ed., Oxford Univ. Press, Oxford, UK, pp. 72–82.

Mailach, R. and Vogeler, K., 2004, “Rotor-Stator Interactions in a Four-Stage Low-Speed Axial Compressor – Part 1: Unsteady Profile Pressures and the Effect of Clocking,” *Journal of Turbomachinery*, Vol. 126, No. 4, pp. 507-518.

Mailach, R., Lehmann, I., Vogeler, K., 2008, “Periodic Unsteady Flow Within a Rotor Blade Row of an Axial Compressor – Part II: Wake-Tip Clearance Vortex Interaction,” *Journal of Turbomachinery*, Vol. 130, pp. 041005-1 – 041005-10.

Mayle, R.E., 1991, “The Role of Laminar-Turbulent Transition in Gas Turbine Engines,” *Journal of Turbomachinery*, Vol. 113, pp. 509-536.

Mertz, C., 1954, “A Study of the Effect of Boundary Layer Control on an Axial Flow Compressor Stage,” Aeronautical Engineer Thesis, California Institute of Technology.

Methel, J.C., Smith, N.R., Key, N.L., 2015, “Vane Wake Characterization Including Variability in a Multistage Compressor,” Presented at the AIAA Science and Technology Forum, Kissimmee, FL, January 5-9.

Miller, K.L., Key, N.L., and Fulayter, R.D., 2012, “Lessons Learned from an Aggressive Outlet Guide Vane Design for Axial Compressors,” *J. Propuls. Power*, Vol. 28, pp.918-926.

Monk, D.J.W., 2014, “A Computational Analysis of the Aerodynamic and Aeromechanical Behavior of the Purdue Multistage Compressor,” MS Thesis, School of Mechanical Engineering, Purdue University, West Lafayette.

Murray III, W.L. 2014, “Experimental Investigation of a Forced Response Condition in a Multistage Compressor,” MS Thesis, Aeronautics and Astronautics, Purdue University, West Lafayette.

NASA, 1965, “Aerodynamic Design of Axial-Flow Compressors,” ed. Johnsen, I.A. and Bullock, R.O., Washington, D.C., NASA SP-36, pp. 206.

Perry, A. E., and Chong, M. S., 1987, “A Description of Eddying Motions and Flow Patterns Using Critical Point Concepts,” *Annu. Rev. Fluid Mech.*, Vol. 19, pp. 125–155.

Poincaré, H., 1928, *Oeuvres de Henri Poincaré, Tome I*, Gauthier-Villars, Paris.

Prato, J., Lakshminarayana, B., and Suryavamshi, N., 1998, “Steady and Unsteady Three-Dimensional Flow Field Downstream of an Embedded Stator in a Multistage Axial Flow Compressor Part 1: Unsteady Velocity Field,” *Presented at the International Gas Turbine & Aeroengine Congress & Exhibition*, Stockholm, Sweden.

Raj, R., Lakshminarayana, B., 1973, “Characteristics of the Wake Behind a Cascade of Airfoils,” Journal of Fluid Mechanics, Vol. 61, No. 4, pp. 707-730.

Reinmöller, U.S.B., Schmidt, S., and Niehuis, R., 2002, “Clocking Effects in a 1.5 Stage Axial Turbine – Steady and Unsteady Experimental Investigations Supported by Numerical Simulations,” *Journal of Turbomachinery*, Vol. 124, No.1, pp. 52-60.

Reynolds, B., Lakshminarayana, B., Ravindranath, A., 1978, “Characteristics of the Near Wake of a Compressor Airfoil,” Presented at the AIAA 11th Fluid and Plasma Dynamics Conference, Seattle, WA, July 10-12, 1978.

Richter, J.-P. 1883 (reprinted 1970). *The Notebooks of Leonardo da Vinci: Compiled and Edited from the Original Manuscripts.* Dover Publications, New York.

Sanders, A.J. and Fleeter, S., 2002, “Rotor Blade-to-Blade Wake Variability and Its Effect on Downstream Vane Response,” *Journal of Propulsion and Power*, Vol. 18, pp. 456-464.

Saravunamuttoo, H.I.H., Rogers, G.F.C., Cohen, H., and Straznicky, P.V., 2009, *Gas Turbine Theory,* Pearson, Essex, pp. 178-181.

Saren, V. E., Savin, N. M., Dorney, D. J., and Zacharias, R. M., 1997, “Experimental and Numerical Investigation of Unsteady Rotor-Stator Interaction on Axial Compressor Stage (With IGV) Performance,” *Unsteady Aerodynamics and Aeroelasticity of Turbomachines, Proceedings of the Eighth International Symposium*, Stockholm, Sweden, pp. 407-424.

Schmidt, D. P. and Okiishi, T. H., 1977, “Multistage Axial-Flow Turbomachine Wake Production, Transport, and Interaction,” *AIAA Journal*, Vol. 15, No. 8, pp. 1138-1145.

Schubauer, G.B. and Klebanoff, P.S., 1956, “Contributions on the Mechanics of Boundary-Layer Transition,” NACA Report No. 1289.

Sherman, P.J., Dudley, R., and Suarez, M., 1996, “The Stochastic Structure of Downstream Pressure from an Axial Compressor – II. An Investigation of Blade-to-Blade Variability,” *Mechanical Systems and Signal Processing*, Vol. 10, No. 4, pp. 423-437.

Smith, L.H., 1964, “Some Comments on Reynolds Number,” *Journal of Engineering for Power,* Vol. 86, No. 3, pp. 225–226.

Smith, L.H., 1966, “Wake Dispersion in Turbomachines,” *Journal of Basic Engineering*, Vol. 88, pp. 688-690.

Smith, N.R., 2011, “Experimental Investigation of Vane Clocking Effects on Stall Performance and Unsteady Vane Boundary Layer Development in a Multistage Compressor,” MS Thesis, Purdue University, West Lafayette.

Smith, N.R., and Key, N. L., 2013, “Vane Clocking Effects on Stall Margin in a Multistage Compressor,” *Journal of Propulsion*, Vol. 29, No.4, pp. 891-898.

Smith, N.R. and Key, N.L., 2014, "Unsteady Vane Boundary Layer Response to Rotor-Rotor Interactions in a Multistage Compressor," *Journal of Propulsion and Power*, Vol. 30, No. 2, pp.416-425.

Solomon, W.J. and Walker, G.J., 1995, “Observations of Wake-Induced Transition on an Axial Compressor Blade,” *Proceedings of the International Gas Turbine and Aeroengine Congress and Exposition,* Houston, TX, ASME Paper 95-GT-381.

Städing, J., Wulff, D., Kosyna, G., Becker, B., and Gümmer, V., 2011, “An Experimental Investigation of Stator Clocking Effects in a Two-Stage Low-Speed Axial Compressor,” *ASME Paper No*. GT2011-45680.

Tobak, M., and Peake, D. J., 1982 “Topology of Three-Dimensional Separated Flows,” *Annu. Rev. Fluid Mech.*, Vol. 14, pp. 61–85.

Van Zante DE, Strazisar AJ, Wood JR, Hathaway MD, Okiishi TH, 2000, “Recommendations for Achieving Accurate Numerical Simulation of Tip Clearance Flows in Transonic Compressor Rotors,” *Journal of Turbomachinery,* Vol. 122, pp.733-742.

Walker, G. J. and Oliver, A. R., 1972, “The Effect of Interaction between Wakes from Blade Rows in an Axial Flow Compressor on the Noise Generated by Blade Interaction,” *Journal of Engineering for Power*, Vol. 94, No. 4, pp. 241-248.

Walker, G. J., Hughes, J. D., Köhler, I., and Solomon, W. J., 1997, “The Influence of Wake-Wake Interactions on Loss Fluctuations of a Downstream Axial Compressor Blade Row,” *ASME Paper No.* 97-GT-469.

Walker, G.J., Hughes, J.D., and Solomon, W.J., 1999, “Periodic Transition on an Axial Compressor Stator: Incidence and Clocking Effects: Part I Experimental Data,” *Journal of Turbomachinery*, Vol. 121, pp. 398-407.

Wellborn, S.R., 1996, “Effects of shrouded stator cavity flows on multistage axial compressor aerodynamic performance,” Ph.D., Iowa State University.

Wellborn, S.R., and Okiishi, T.H., 1999 “The Influence of Shrouded Stator Cavity Flows on Multistage Compressor Performance,” *Journal of Turbomachinery,* Vol. 121, No. 3, pp. 486-497.

Williams, M.C., 1988, “Inter and Intrablade Row Laser Velocimetry Studies of Gas Turbine Compressor Flows,” *ASME Journal of Turbomachinery,* Vol. 110, No. 3, pp. 369-376.

Wisler, D.C., 1985, “Loss Reduction in Axial-Flow Compressors Through Low-Speed Model Testing,” *J. Engineering for Gas Turbines and Power*, Vol. 107, No. 2, pp. 354-363.

Wisler, D.C., 1998, “The Technical and Economic Relevance of Understanding Boundary Layer Transition in Gas Turbine Engines,” *Minnowbrook II, 1998 Workshop on Boundary Layer Transition in Turbomachines*, NASA/CP- 1998-206958.

Wright, T., 1999, *Fluid Machinery: Performance, Analysis, and Design*, CRC Press, Boca Raton, FL, pp. 52-56.

Zierke, W. C., and Straka, W. A., 1996, ‘‘Flow Visualization and the Three-Dimensional Flow in an Axial Flow Pump,” *Journal of Propulsion Power,* Vol. 12, pp. 250–259.

# APPENDICES

# Appendix A. Flow Visualization of Vanes with Downstream Instrumentation

Chapter 4 discussed the stator suction side separation line variability as observed from flow visualization images. The following figures show the Stator 1, Stator 2, and Stator 3 vanes which have downstream instrumentation ports. Due to limited paint coverage, there are only images available of the circumferential position D.

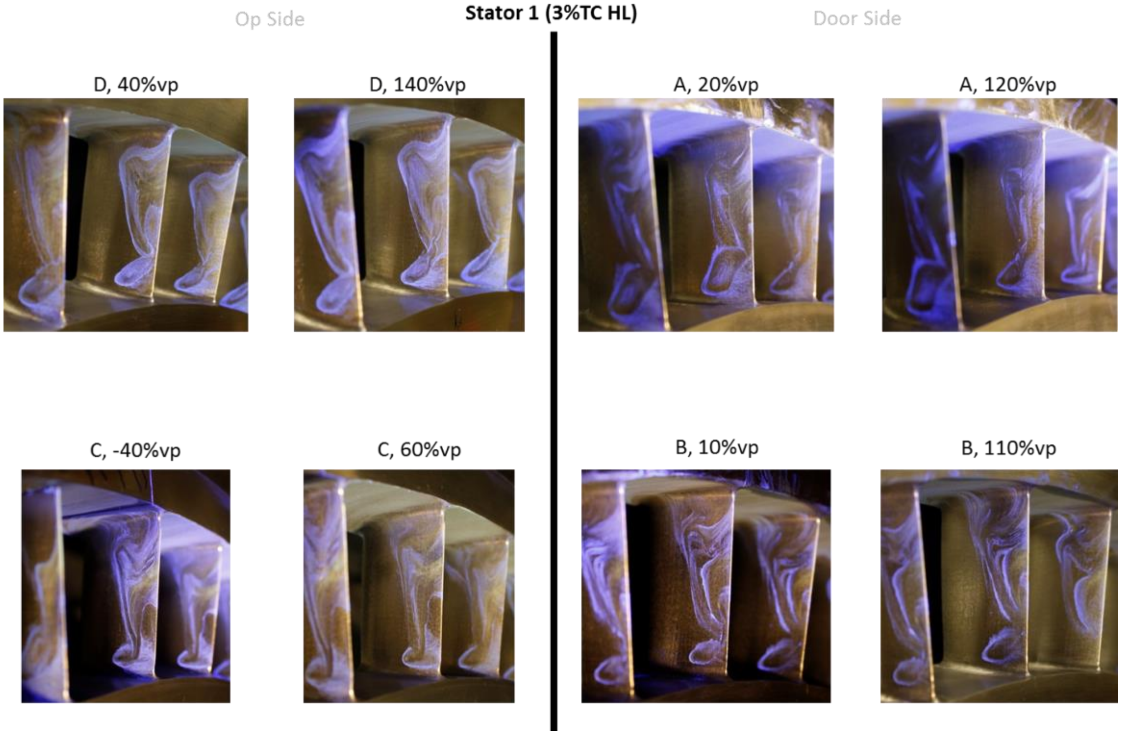

Figure A.1 Stator 1 Vanes with Downstream Instrumentation

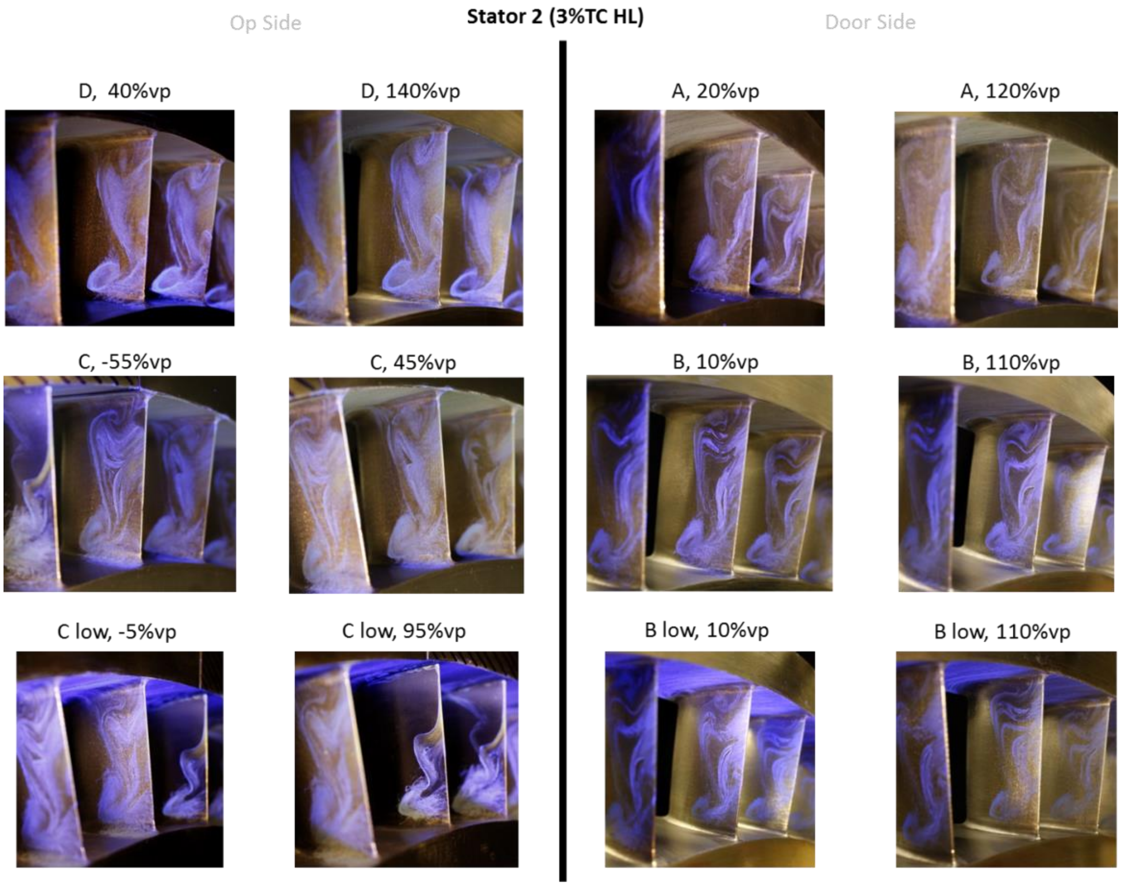

Figure A.2 Stator 2 Vanes with Downstream Instrumentation

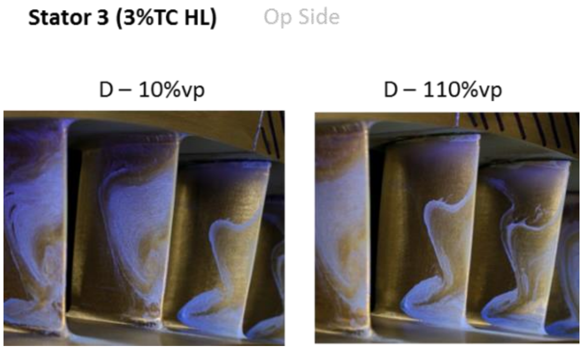

Figure A.3 Stator 3 Vanes with Downstream Instrumentation

# Appendix B. Gallery of Fluid Motion

A portion of the flow visualization study presented in Chapter 4 with different rotor tip clearances was submitted to the Gallery of Fluid Motion. This submittal is shown in Figure B.1.

Natalie R. Smith | Ph.D. Candidate | Purdue University, West Lafayette, IN
Nicole L. Key | Associate Professor | Purdue University, West Lafayette, IN

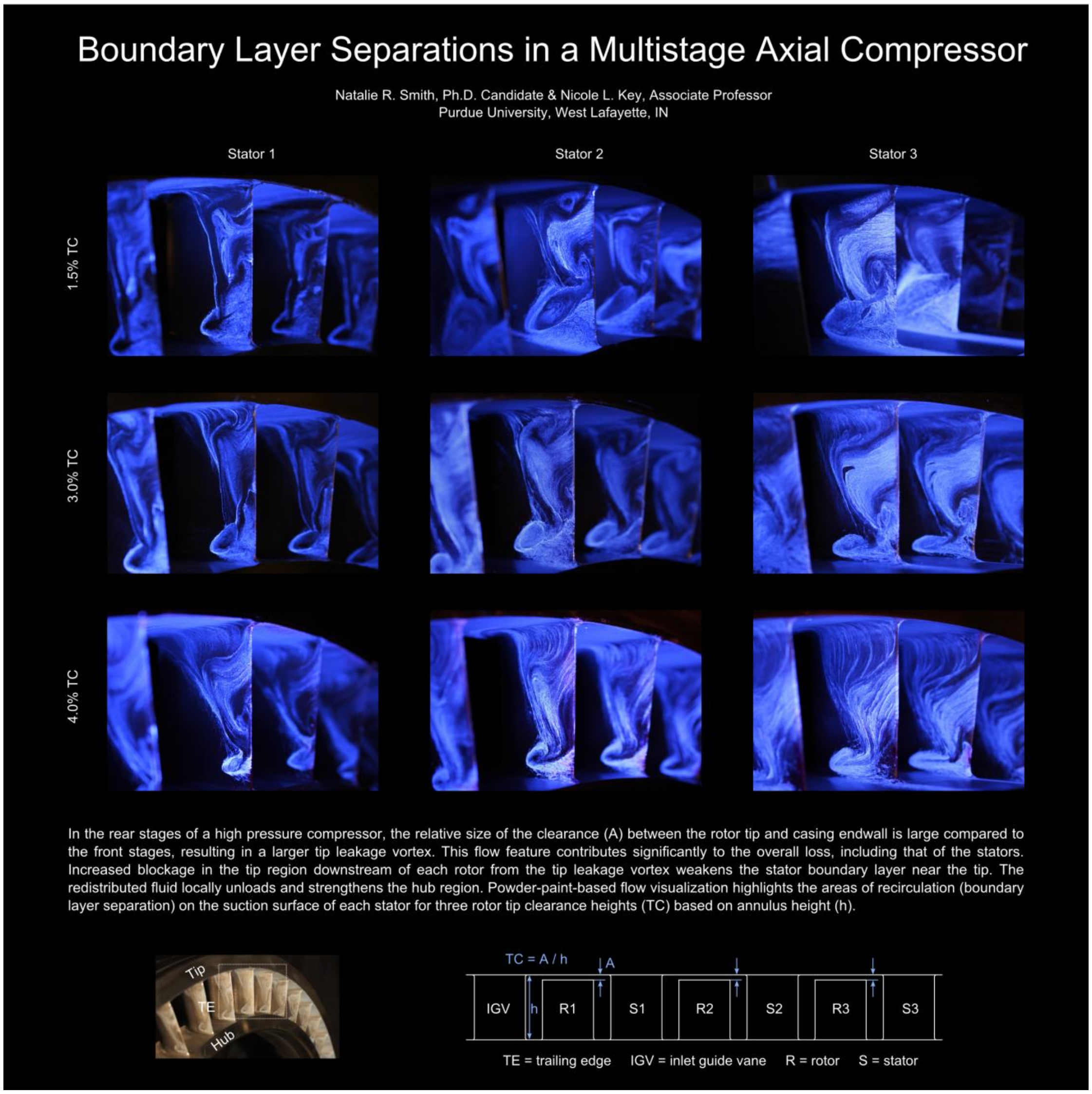

Boundary Layer Separations in a Multistage Axial Compressor

Natalie R. Smith, Ph.D. Candidate & Nicole L. Key, Associate Professor
Purdue University, West Lafayette, IN

In the rear stages of a high pressure compressor, the relative size of the clearance (A) between the rotor tip and casing endwall is large compared to the front stages, resulting in a larger tip leakage vortex. This flow feature contributes significantly to the overall loss, including that of the stators. Increased blockage in the tip region downstream of each rotor from the tip leakage vortex weakens the stator boundary layer near the tip. The redistributed fluid locally unloads and strengthens the hub region. Powder-paint-based flow visualization highlights the areas of recirculation (boundary layer separation) on the suction surface of each stator for three rotor tip clearance heights (TC) based on annulus height (h).

TE = trailing edge IGV = inlet guide vane R = rotor S = stator

Figure B.1 Gallery of Fluid Motion 2015 Submission

# Appendix C. Stator 2 Insert Design with Leading Edge and Knife Seal Pressures

To investigate the total pressure field at the Stator 2 leading edge, a special two-vane passage section was designed with instrumentation. This stator insert features a vane with leading edge Kiel-heads incorporated directly into the vane for total pressure measurements. Pressure tubulations are routed through the vane and out of the casing.

The two-vane passage stator insert presents manufacturing challenges for a couple reasons. The vane geometry, particularly at this scale (vane span of 2in) and the desired tolerances of 0.005in on the contours, is difficult to machine. Furthermore, stainless steel (17-4) is not the easiest material to machine. These factors caused excessive delays with the first stator 2 insert. In the previous case, instrumentation was added by milling out the opposing sides of the vane, installing the sensors and filling the holes to reform the vane surface contour. In this case with leading edge instrumentation, using this technique would alter much larger portions of the vane surface and be much closer the measurements themselves at the leading edge, and thus is less ideal. Following design discussions with a couple companies, quotes and lead times were returned as summarized in Table C.1. Although not surprising for the technical challenges associated with manufacturing this part, these numbers were above the allowable budget for this project.

An alternate manufacturing technique was then pursued: direct metal laser sintering (DMLS) or direct metal laser melting (DMLM), commonly referred to as 3D printing. This would allow for more flexibility in the routing of holes and more measurements could be added without additional costs. The overall size of the part drives the cost of 3D printing not the complexities of the small features.

Table C.1 Costs and lead times of different vendors and manufacturing methods

| | Company | Approx. Cost | Lead Time |
|---|---|---|---|
| Traditional Machining | A | $20,000 | 8 weeks |
| | B | $27,000 | 8-10 weeks |
| 3D Printing (DMLS) | C | $5,000 | 3 weeks |
| | GPI Prototype | $6,200 | 2 weeks |

Although it has benefits to cost, lead time, and design freedom, the 3D printing technique has different design considerations. The scale and detail desired in the stator insert is close to the limits of current DMLS. The laser beam is 0.004inches in diameter and tolerance capabilities are dependent on the build direction. The stator insert was printed with the trailing edge plane down and each layer added moving toward the leading edge. Small holes with axes parallel to the build direction are easier to main tolerance and roundness. Whereas small holes with axes perpendicular to the build direction are more difficult to print accurately. The engineers who work with these machines suggestion oversizing the holes by 0.025inches to guarantee a minimum hole diameter. Furthermore, one must consider the ease of cleaning out support material posting-printing. This was a particular challenge when design the measurement hole/connector termination in the outer shroud of the stator insert.

Several geometry designs for the leading edge Kiel-heads were considered, shown in Figure C.1. The initial design resembled the Kiels on the total pressure rakes, as shown in Figure C.1a. The small details of this design, such as the vent holes in the Kiel perpendicular to the hole axis and the gaps between the pressure port and the Kiel, were too small and complicated to incorporate into the 3D printing limitations. These features were deemed unnecessary, and simpler designs were considered, Figure C.1b and Figure C.1c. These designs feature the chamfer of the Kiel-head immediately at the leading edge with the pressure port. Ultimately, the design in Figure C.1b was chosen because of the end of the Kiel aligns with the stator leading edge.

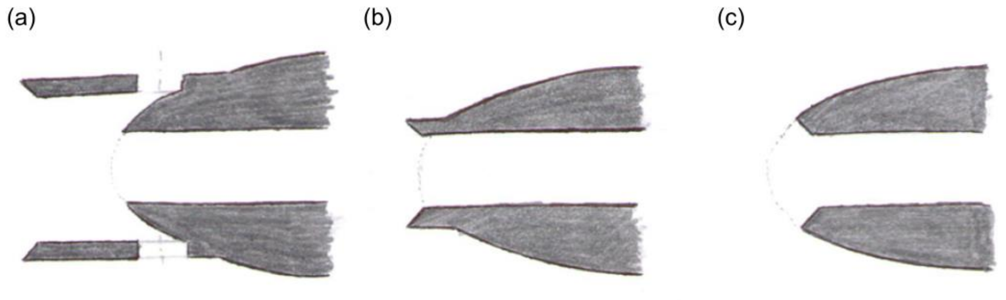

Figure C.1 Kiel-head geometry considerations

The literature is scarce when it comes to experimental data acquisition in the knife seal and stator hub cavity region. (Wellborn, 1996) Advice was sought from several colleagues in the turbomachinery industry on where compressor designers and modelers would prefer these measurements (King, 2014; Cargill, 2014). Based on these conversations and some previous modelling, static pressure taps were placed 0.2in upstream and downstream of the two knife seals. This distance is approximately the distance between the two knife seals. This position should have nearly parallel streamlines while still allowing flexibility with manufacturing and assembly tolerances. The upstream and downstream locations each have four circumferential measurement positions at 0%, 25%, 50%, and 75% of the vane passage, where 0% is aligned with the Stator 2 leading edge. This will provide insight to any pitchwise variations in the knife seal leakage flow.

Despite the freedom 3D printing allows with hole routing, the overall part size is small and space is particularly limited at the casing shroud due to bolt holes for mounting. An overview of the measurement positions, routing, and connector layout is shown in Figure C.2. Based on the position of the mounting bolt holes and through holes in the casing through which pressure tubes can be routed out of the compressor, connector slots were place in the Stator 2 section tip shroud. These slots were sized to accommodate fifteen pressure connections. Several connector designs were considered. Typical laboratory practice installs small metal pressure tubulations into an appropriately sized counter bore in the hardware using JB Weld. A similar installation was deemed unusable due to radial limitations to accommodate plastic tubing, metal connector, and internal routing. The option to have these connectors printed integral with the insert was also explored, but not feasible due to support issues. The final design features counter-bores where plastic tubes were installed after receiving the part.

The Kiel-heads are located on “vane 1” at the same seven radial positions as the interstage rakes. The pressure port holes are routed along the camber line at each radial height downstream to the mid-chord region with large vane thickness where each is then routed up through the center of the vane toward the tip shroud.

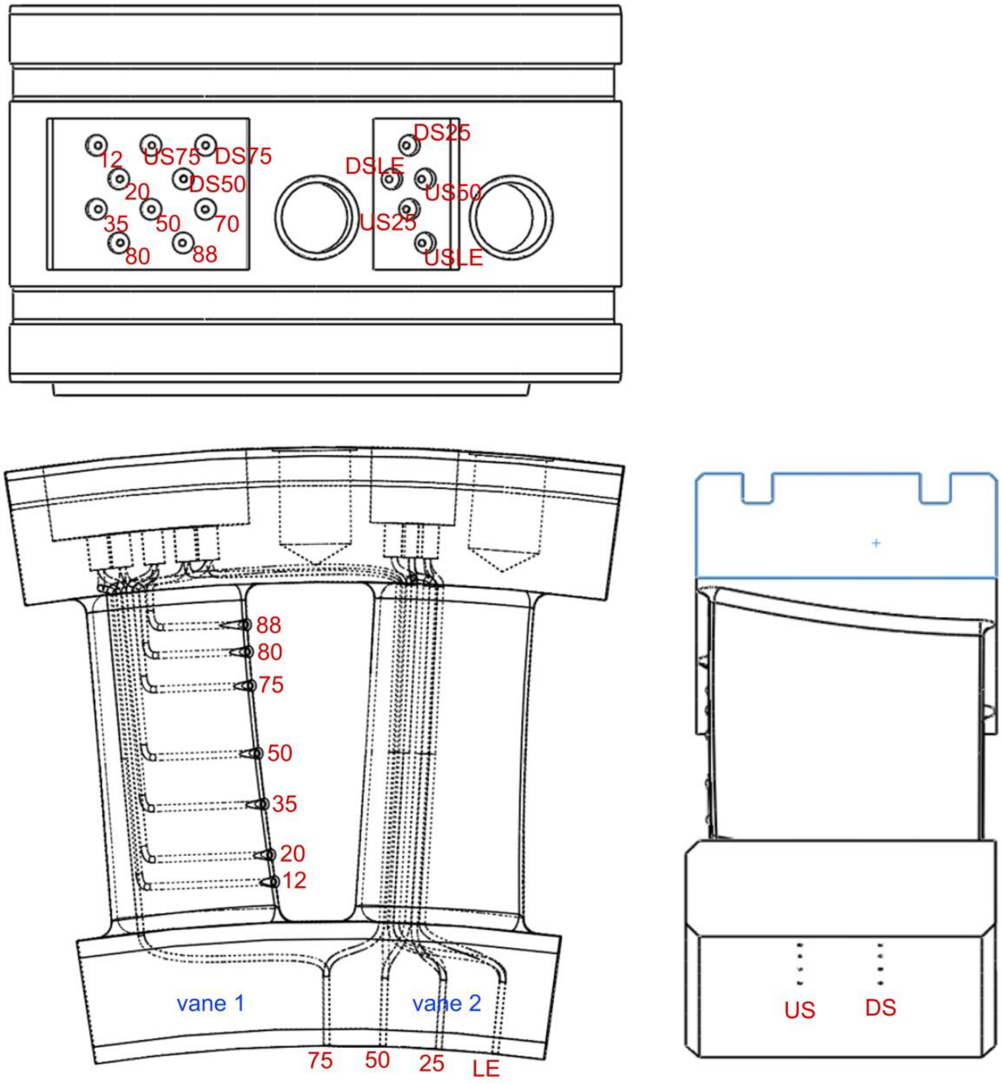

Figure C.2 Stator 2 insert model with routing holes and connector configuration

# VITA

# VITA

Natalie Rochelle Smith was born to parents Brian and Elizabeth Smith on April 7, 1987 in Hollister, California. She has one brother, Aaron Smith. She grew up in Hollister, California and graduated from San Benito High School in 2005. In August of 2005, she began pursuing her Bachelor's degree in aerospace engineering at California Polytechnic State University, San Luis Obispo. During her undergraduate, she had internships with Pacific Scientific Energetic Materials Company and Pratt and Whitney Rocketdyne with the Space Shuttle Main Engine Main Combustion Chamber and Nozzle development group. She graduated from Cal Poly with a Bachelor's of Science in 2009. In August, 2009, she began her graduate studies at Purdue University in the School of Aeronautics and Astronautics with advisor Nicole Key where she studied the effects of vane clocking on stall margin and boundary layer response in the Purdue 3-stage research compressor. She graduated from Purdue with her Masters of Science in Aeronautics and Astronautics in December 2011. She continued her graduate studies at Purdue where she received a NASA Graduate Student Research Program fellowship. She will receive her Ph.D. from the School of Aeronautics and Astronautics in May 2015.

# PUBLICATIONS

# PUBLICATIONS

Brossman, J.R., **Smith, N.R.**, Talalayev, A, Key, N.L., 2011, “Tailoring Inlet Flow to Enable High Accuracy Compressor Performance Measurements,” *Int. J. Turbo Jet-Engines*, Vol. 28, pp. 309–320.

**Smith, N.R**., Key, N.L., 2013 “Vane Clocking Effects on Stall Margin in a Multistage Compressor,” *Journal of Propulsion and Power*, Vol. 29, pp. 891-898.

Brossman, J.R., Ball, P.R., **Smith, N.R.**, Methel, J.C., Key N.L., 2014 “The Sensitivity of Multistage Compressor Performance to Inlet Boundary Conditions,” *Journal of Propulsion and Power*, Vol. 30, pp. 407-415.

**Smith, N.R.**, Key, N.L., 2014 “Unsteady Vane Boundary Layer Response to Rotor-Rotor Interactions in a Multistage Compressor,” *Journal of Propulsion and Power*, Vol. 30, pp. 416-425.

**Smith, N.R.**, Key, N.L., 2014, “Unsteady Vane Boundary Layer Response to Rotor-Rotor Interactions in a Multistage Compressor,” *Journal of Propulsion and Power*, Vol. 30, pp. 416-425.

**Smith, N.R**., Key, N.L., 2015, “Vane Clocking Effects on Stator Loss for Different Compressor Loading Conditions,” *Journal of Propulsion and Power*, Vol. 31, pp.519-526.

Berdanier R.A., **Smith N.R.**, Fabian J.C., Key N.L., 2015, “Humidity Effects on Experimental Compressor Performance—Corrected Conditions for Real Gases,” *Journal of Turbomachinery*, Vol. 137, 031011 (10 pages).

**Smith, N.R.**, Key, N.L., 2015, “Flow Visualization for Investigating Stator Losses in a Multistage Axial Compressor,” Accepted to *Experiments in Fluids*.

**Smith, N.R**., Berdanier, R.A., Fabian, J.C., Key, N.L., 2015, “Reconciling Compressor Performance Differences with Varying Ambient Inlet Conditions,” Accepted to *Journal of Engineering for Gas Turbines and Power*.

**Smith, N.R.**, Murray III, W.L., Key, N.L., 2015, “Considerations for Measuring Compressor Aerodynamics Excitations Including Rotor Wakes and Tip Leakage Flows,” ASME Paper GT2015-43508, To be presented at the ASME Turbo Expo Montréal, Canada, June 15-19, 2015 and submitted to *Journal of Turbomachinery*.